12-2015

Effective field theory approach to collective motion in atomic nuclei

Eduardo Antonio Coello Perez
University of Tennessee - Knoxville, ecoello@vols.utk.edu

To the Graduate Council:

I am submitting herewith a thesis written by Eduardo Antonio Coello Perez entitled "Effective field theory approach to collective motion in atomic nuclei." I have examined the final electronic copy of this thesis for form and content and recommend that it be accepted in partial fulfillment of the requirements for the degree of Doctor of Philosophy, with a major in Physics.

Thomas Papenbrock, Major Professor

We have read this thesis and recommend its acceptance:

Lucas Plater, Kate Jones, Robert Hinde

Accepted for the Council:

Carolyn R. Hodges

Vice Provost and Dean of the Graduate School

(Original signatures are on file with official student records.)

Effective field theory approach to collective motion in atomic nuclei

A Dissertation Presented for the
Doctor of Philosophy
Degree
The University of Tennessee, Knoxville

Eduardo Antonio Coello Pérez
December 2015

ACKNOWLEDGMENTS

I would like to express my sincere gratitude to my adviser, Professor Thomas Papenbrock. His course on Advanced Quantum Mechanics motivated me to start a career on theoretical nuclear physics. His guidance and persistent help made this dissertation possible.

I would like to thank my committee members, Professor Robert Hinde, Professor Kate Jones and Professor Lucas Platter, for asking questions whose attempts to respond significantly improve my understanding of the subject. Especial thanks to Professor Lucas Platter, for his useful advice on applications for postdoctoral positions.

In addition, I would like to thank Doctor Efraín Rafael Chávez Lomeli, Doctor Dan Shapira and Professor Kate Jones. Their support encourage me to start the graduate program in physics at The University of Tennessee.

For their infinite support, I would like to sincerely thank my whole family. Especial thanks to my parents, Marco Antonio Coello Coutiño and Maite Pérez Pérez, and brothers, Alejandro Coello Pérez, Daniel Coello Pérez and Raúl Coello Pérez. Without your love and patience I would not have come so far.

At last but not least, I would like to thank my friends Aislin, Alexandra, Alvaro, Ana, Andrés, Andrea, Avelina, Beakman, Ben, Callie, Camilo, Carolina, Caroline, Celia, Cholo, Chris, Chrisanne, Citlali, Corina, Cory, Daniel, Desireé, Diana, Don, Dookie, Ehira, Elena, Elisa, Ellen, Emi, Erika, Fátima, Fabo, Felipe, Frank, Gary, Georgina, Grant, Horus, Ingrid, Jenny, Jim, Jonas, Jozra, Julián, Justin, Kat, Lefty, Lety, Linda, Luciana, Mafe, Malcond, Manuel, Marcel, María, Marisol, Marta, Mary, Mauricio, Mauro, Max, Melqui, Miguel, Mike, Moustapha, Nacho, Nelly, Noemi, Olga, Pamela, Paty, Paul, Penny, Poncho, Quiela, Ryan, Rulo, Sabrina, Sam, Sandra, Santiago, Sofia, Spencer, Stuart, Tonatiuh, Trey, Virginia, Waldo, Xóchitl, Yannick and Zaira. Without you, graduate school would not have been as amazing as it was.

ABSTRACT

Collective motion in heavy nuclei has been studied within collective and algebraic models, and within density functional theory. While they reproduce the energy spectra of these systems, their predictions for some electromagnetic transitions and moments do not lie within experimental uncertainty; in other words, these predictions are inconsistent with experimental data. An effective field theory approach to collective motion in heavy nuclei solves this long standing problem. Based on symmetry arguments only, the effective field theories, constructed as expansions in powers of a small parameter, consistently describe the energy spectra of nuclei exhibiting collective motion at low order in the expansion parameter, reproducing results from models at this order. The systematic construction of operators associated with observables, allows for the estimation of theoretical uncertainties order by order. This is a highlight of effective field theories. Bayesian methods can be employed to quantify these uncertainties, providing them with a clear statistical interpretation. Within the effective field theories, the description of experimental data on electric quadrupole transitions and moments is consistent within theoretical uncertainties. In nuclei near shell closures, the systematic construction of the electric quadrupole operator allows for the description of sizeable static quadrupole moments and transitions between states with the same phonon number. In rotational nuclei faint transitions between states in different rotational bands are correctly described and are of natural size.

TABLE OF CONTENTS

LIST OF TABLES

LIST OF FIGURES

1
INTRODUCTION

In many physical systems, different phenomena take place at different energy scales E_{low} and E_{high}, fulfilling the condition $E_{\text{low}} \ll E_{\text{high}}$. An effective field theory (EFT) is an extremely powerful tool if one is interested in the description of the low-energy physics of systems with a large separation of energy scales. In the past, EFTs have been employed to successfully describe the low-energy physics in diverse systems. In nuclear physics, EFT approaches based on the spontaneous breaking of the chiral symmetry have been used to describe the interaction between nucleons systematically [1, 2, 3, 4, 5], allowing for the model-independent description of nucleon-nucleon scattering, few-nucleon systems [6, 7, 8, 9], neutron matter [10, 11], light halo nuclei [12, 13, 14] and nuclear reactions [15, 16]. In combination with many-body methods, EFT potentials can be employed to describe heavier systems [17, 18, 19, 20, 21].

In certain atomic nuclei, collective excitations in which the motion of a large number of nucleons is coherent, are the least energetic modes. This collectivity has been studied within several models, referred to as collective models, among which Bohr collective model is one of the best known [22, 23, 24, 25]. On the other hand, the separation of scales between collective motion and other excitation modes motivates the description of the former within EFT approaches. These EFTs have been developed in Refs. [26, 27, 28]. Refs. [29, 30] are reported in this thesis. In this Chapter, the basis for the construction of such EFTs for collective motion are established. The Bohr collective model is briefly reviewed too.

1.1 Effective field theories

In this Section, the procedure to construct EFTs is described. As described in Ref. [5], this procedure can be summarized as follows.

(i) First, the separation of scales between low- and high-energy physics must be established. This allows for the identification of the degrees of freedom (DOF) of the EFT.

(ii) Second, the symmetries of the system must be identified. Whether these symmetries are broken or not is relevant for the construction of the EFT. Broken symmetries must be realized nonlinearly [31, 32, 33].

(iii) Finally, the most general Lagrangian or Hamiltonian consistent with the symmetries of the system must be constructed. A power counting must be established for this construction to be systematic.

A direct consequence of the systematic construction of an EFT is the possibility to estimate the theoretical uncertainty in calculations at each order of the power counting. This estimate, which is a highlight of EFT approaches (not offered by models), allows for a meaningful comparison against experimental data.

1.1.1 Separation of scales and effective degrees of freedom

Assume that the system is completely described by a "fundamental" theory in terms of the degrees of freedom (DOF) x and X that represent excitation modes below and above certain energy scale Λ, respectively. The description of the system below Λ can be achieved by integrating out the high-energy DOF. The resulting theory, referred to as EFT, is written in terms of the x DOF, and depends on the energy scale Λ, referred to as breakdown scale. If the energy scale where low-energy physics takes place is denoted by E, the EFT can be written as an expansion in powers of $Q \equiv E/\Lambda$, where the expansion coefficients depend on Λ and enclose all the information about the "fundamental" theory.

If one does not start from the "fundamental" theory, it is possible to write the EFT as follows. From the energy spectrum of the system, the DOF relevant to describe the physics of the system up the energy scale Λ must be inferred. Then, the most general Lagrangian consistent with the symmetries of the system is constructed. Without an underlying theory to calculate the values of the low-energy constants (LECs) of the EFT, they must be fit to experimental data. If data on some low-energy observables is employed to fit the LECs, predictions can be made for other observables below the breakdown scale Λ.

The separation of scales can also be understood in terms of resolution. Assume a projectile in a scattering experiment has a momentum p. This particle can only "see" structures with a linear dimension $R \geq p^{-1}$. Thus, if the components of the target are characterized by $R < p^{-1}$, they cannot be resolved by the projectile, and the experiment can be described within an EFT that employs the projectile and the target, not its constituents, as effective DOF.

Let us briefly mention examples of EFTs for the description of nuclear interactions. At low energies, nucleon processes with a momentum p below the mass of

the rho meson m_ρ can be described within the chiral EFT. This theory employs nucleon and pion fields as DOF, and is written as an expansion in powers of p/m_ρ and m_π/m_ρ, where m_π is the mass of the pion. Processes with momentum below m_π do not involve pions. At this scale, nucleon-nucleon scattering is characterized by the effective range of the nuclear interaction and the long scattering lengths, denoted by r_0 and a, respectively. These processes can be described within the pionless EFT. This theory is written in terms of nucleon fields only, as an expansion in powers of r_0/a, with $r_0 \ll a$.

The energy scale of collective motion in heavy nuclei ranges from around 50 keV to 1 MeV. Single particle motion becomes relevant at 2 or 3 MeV. Thus, the small parameter Q and the convergence rate of the EFTs describing collective motion vary from nucleus to nucleus.

1.1.2 Symmetries and symmetry breaking

A physical system possesses a symmetry if its Lagrangian or Hamiltonian remains invariant after its DOF transform under the transformation in certain group $\mathcal{G}$, referred to as symmetry group. This symmetry is spontaneously broken if the ground state of the system is only invariant under a subgroup $\mathcal{H}$ of the symmetry group $\mathcal{G}$. The low-energy spectrum of an infinite system with a broken symmetry is described in terms of low-energy Nambu-Goldstone modes [34].

In order to exemplify these concepts, let us briefly discuss the EFT approach to ferromagnets [35]. The Hamiltonian of a ferromagnet is invariant under the spin-rotational symmetry group O(3), which contains all transformations that rotate the orientation of all the spins. On the other hand, all spins in the ground state of these systems are aligned, breaking the O(3) symmetry of the Hamiltonian to the spin-rotational symmetry group O(2), which contains all transformations that rotate all the spins around the direction of alignment. The Nambu-Goldstone modes in these systems are long-wavelength (or low-energy) spin waves that give rise to small oscillations of the orientation of the spins around the direction of alignment. This oscillation depends on position and time.

As mentioned before the Nambu-Goldstone modes describe the low-energy spectrum of an infinite ferromagnet. For a finite one, the ground states corresponding to different alignment directions overlap. Thus, a finite ferromagnet can undergo rotations that change the alignment direction. These rotations are represented by time-dependent modes [36].

Many nuclei exhibit spectra with rotational bands, implying an intrinsic deformation of their ground states. Thus, the SO(3) symmetry of the Hamiltonian describing these systems is spontaneously broken. The construction of the EFT for the description of these system employs DOF that realize the SU(3) symmetry nonlinearly [26, 27, 28].

1.1.3 Power counting and the systematic construction of EFTs

The Lagrangian or Hamiltonian of an EFT employed to describe a system, must contain every single term consistent with the symmetries of the system. There is an infinite number of such terms. As mentioned before, the EFT can be written as a power in the small expansion parameter $Q \equiv E/\Lambda$, where E is a "small" scale (where the processes of interest take place) compared to Λ, the breakdown scale for the EFT.

Thus, an EFT can be systematically constructed order by order. For this purpose, it is necessary to establish a power counting that allows one to infer at which order in Q a contribution to the Lagrangian or Hamiltonian becomes relevant. Higher-order calculations within the EFT require more LECs to be fit to data, reducing the predictive power of the theory. While this reduction of predictive power is not ideal, it comes hand-to-hand with an increase of accuracy in the calculations.

To exemplify the systematic construction of a theory, let us discuss the following system. Assume a particle of mass m and charge q is immerse in a static electric field generated by a localized charge distribution with density $\rho(\mathbf{r})$. Let the center of mass of the distribution coincide with the origin of the reference frame, and the particle be far away from it, that is, if the distribution is contained within a sphere of radius ρ, let the particle be at a distance R from the origin such that $\rho \ll R$. The Hamiltonian of the system is given by

$$H = \frac{p^2}{2m} + q\Phi(\mathbf{R}), \tag{1.1}$$

where p is the momentum of the particle, and $\Phi(\mathbf{R})$ is the electric potential due to the charge distribution at the position of the particle $\mathbf{R}$. This potential can be written as a multipole expansion [37]

$$\Phi(\mathbf{R}) = \frac{1}{R}\sum_{IM}\frac{4\pi}{2I+1}\frac{q_{IM}}{R^I}Y_{IM}(\theta,\phi), \tag{1.2}$$

with $I = 0, 1, ..., \infty$ and $-I \leq M \leq I$. Here $Y_{IM}(\theta, \phi)$ are spherical harmonics, θ and ϕ are the angles determining the orientation of $\mathbf{R}$, and the quadrupole moments q_{IM} are given by

$$q_{IM} \equiv \int dV' \, Y^*_{IM}(\theta', \phi') r'^I \rho(\mathbf{r}'), \tag{1.3}$$

where the integration is over all space. Thus, the multipole expansion is in powers of ρ/R.

An EFT for this system can be systematically constructed. At leading order (LO), the interaction term takes the form

$$\Phi_{\rm LO}(\mathbf{R}) = \frac{1}{R} q_0, \tag{1.4}$$

where q_0 is a LEC and must be fit to data. The next-to-leading order (NLO) correction to this interaction is of order $\mathcal{O}(r/R)$. It can be written as

$$\Delta\Phi_{\rm NLO}(\mathbf{R}) = \frac{1}{R} \sum_M \left(\frac{r}{R}\right) q_{1M} Y_{1M}(\theta, \phi). \tag{1.5}$$

From here, it is clear that the EFT for the particle in the static electric field at NLO requires more experimental data to fit the LECs q_0 and q_{1M}, reducing its predictive power when compared to the EFT at LO. Nevertheless, the NLO expression for the interaction is closer to the real one given by the multipole expansion (1.2). Consequently, the EFT increases its accuracy. In other words, better agreement with experimental data is expected at higher orders in the EFT.

1.1.4 Theoretical uncertainty

A direct consequence of the systematic construction of any operator $\hat{O}$ associated to the observable O within EFT approaches, is the ability to estimate the theoretical uncertainty at any order [38, 39].

Within an EFT, the observable O may be written as an effective expansion in powers of a small parameter $Q \ll 1$

$$O = O_0 \sum_i \mathscr{C}_i Q^i, \tag{1.6}$$

with $i = 0, 1, \ldots, \infty$. Here O_0 is the natural size of the observable (which is factored out of the expansion) and the coefficients $\mathscr{C}_i$ are expected to be of order

one, for each term to scale as the expected power of Q. Large or small values for these expansion coefficients would cast doubts about the power counting. A calculation at order k truncates the expansion (1.6) at the term with $i = k$. The error in this calculation is

$$\Delta O = O_0 \sum_{i=k+1} \mathscr{C}_i Q^i. \tag{1.7}$$

For a small value of Q, this error is dominated by the term of order $\mathcal{O}(Q^{k+1})$, and the theoretical uncertainty can be estimated to be

$$\Delta O = O_0 Q^{k+1}. \tag{1.8}$$

Thus, the theoretical uncertainty decreases with increasing order. In other words, the precision with which an observable is calculated within the EFT increases order by order.

Bayesian analysis methods can be employed to quantify the theoretical uncertainty, giving it a clear statistical interpretation. For this purpose, it is necessary to calculate the probability distribution function (pdf) for the error (1.7). Marginalization and Bayes' theorem are employed for this calculation (see Ref. [40] for details).

The quantification of the theoretical uncertainty via Bayesian statistics relies on assumptions made for the coefficients $\mathscr{C}_i$ in the expansion (1.6), encoded in their pdfs. Consequently, the theoretical uncertainty depends on the functional form of these distributions. Therefore, it is necessary to test these assumptions as follows. If calculations at order k have been carried out, the distributions of the expansion coefficients C_i with $i \leq k$ are known. These distributions can be compared against some pdfs assumed for such coefficients. In Chapter 2 the theoretical uncertainty is quantified from two pdfs for the expansion coefficients. A detailed discussion will be presented there.

1.2 Collective motion in nuclei

Most even-even atomic nuclei possess 0^+ ground states and a 2^+ first excited state. The excitation energy of the later, and the electric quadrupole ($E2$) reduced transition probabilities between these states are crucial to characterize the excitation as either collective or non collective. Experimental evidence of collective motion in atomic nuclei was first found in heavy nuclei with a large number of nucleons outside closed shells. Figure 1.1 shows the full energy spectrum of ^{168}Er

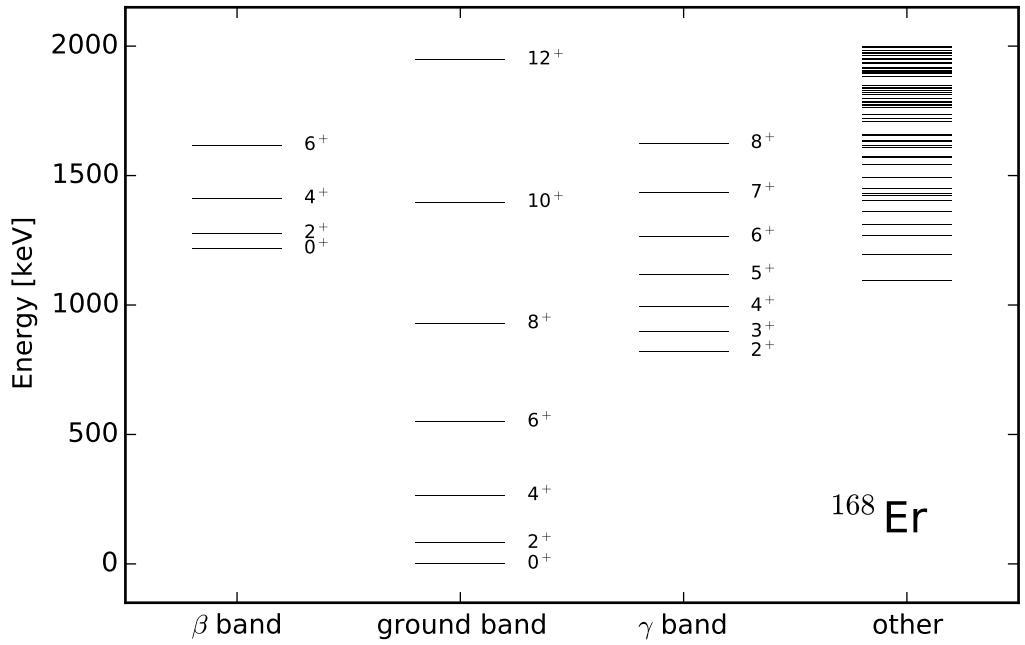

Figure 1.1: Full energy spectrum of ^{168}Er below 2 MeV [41]. Some of the states have been classified as members of the ground, β or γ rotational bands [42]. States under the label "other" do not belong to these rotational bands.

below 2 MeV [41], to illustrate the features of the spectra of midshell nuclei with $A \sim 150$. As shown in the figure, the spectrum in these systems can be arranged into bands [43, 44, 45]. The members of the lowest band have energies that closely follow the relation $E(I) \propto I(I+1)$ where I is the angular momentum of the state. A spectrum proportional to $I(I+1)$ is characteristic of rotational systems, implying midshell nuclei posses a low-energy rotational mode of motion, suggesting an intrinsic deformation of their ground states. At higher energies, other excitation modes become available to the systems, giving rise to spectra consisting of rotational bands on top of high-energy excitations. The details on the nomenclature of the different bands will be given in Section 1.3.4.

Near shell closures, the energy spectra of heavy nuclei are very different from that of midshell nuclei. In Figure 1.2, the full energy spectrum of ^{120}Te below 2.5 MeV [46] is shown to illustrate the features of the spectra of nuclei near shell closures with $A \sim 100$. In these nuclei, the lowest portion of the spectrum exhibits a pattern expected for a harmonic quadrupole vibrator. For the later, the energy spectrum consists of multiplets with energies proportional to the total number of excited quanta of the quadrupole vibrational modes N, that is $E(N) \propto N$. The details for the harmonic vibrator will be given in Section 1.3.2. The identification of states with harmonic quadrupole excitations is clear up to states with $N = 2$. At

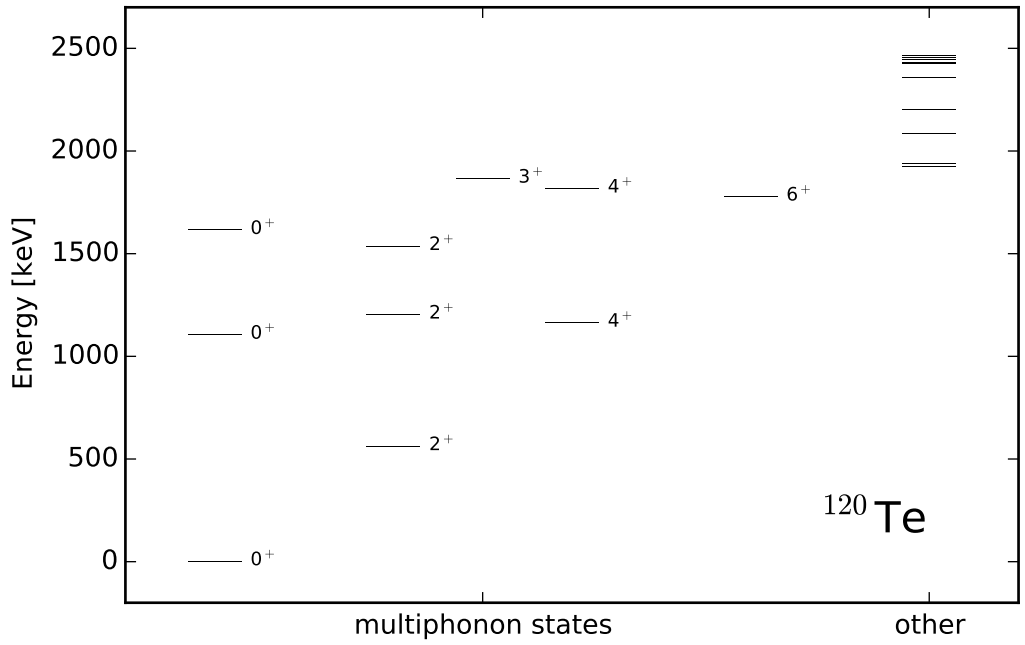

Figure 1.2: Full energy spectrum of ^{120}Te below 2.5 MeV [46]. Some of the states have been classified as one-, two- and three-phonon quadrupole excitations. States under the label "other" are not characterized as multiphonon excitations.

the energy scale where the three-phonon states lie, other modes become available to these systems, making the identification of quadrupole excitations difficult. From now on, the energy scale where the states with N phonons lie will be referred to as the N-phonon level.

Thus, the low-energy behavior of even-even nuclei seems to depend on the number of nucleons outside closed shells. For nuclei near shell closures, the energy ratio between the 4_1^+ state and the 2_1^+ state, $R_{4/2} \equiv E(4_1^+)/E(2_1^+) \approx 2$. For midshell nuclei $R_{4/2} \approx 10/3$. This ratio can be employed to identify nuclei with low-energy vibrational or rotational modes of motion. In Figure 1.3, the $R_{4/2}$ ratio in even-even nuclei is as a function of N and Z. Roughly, yellow and orange squares represent nuclei for which $R_{4/2} \sim 2$ and $R_{4/2} \sim 10/3$, respectively.

1.2.1 Electric quadrupole transitions and quadrupole moments

In even-even heavy nuclei, the excitation mode giving rise to the 2_1^+ state involves a large number of nucleons moving coherently. The experimental evidence supporting this collective motion resides in the $E2$ reduced transition probabilities for the decay from the 2_1^+ state to the 0_1^+ state. These transition rates are very large when compared to the single-particle or Weisskopf unit, denoted by W. U. For a nucleus with A nucleons, a Weisskopf unit is given by the $E2$ reduced transition

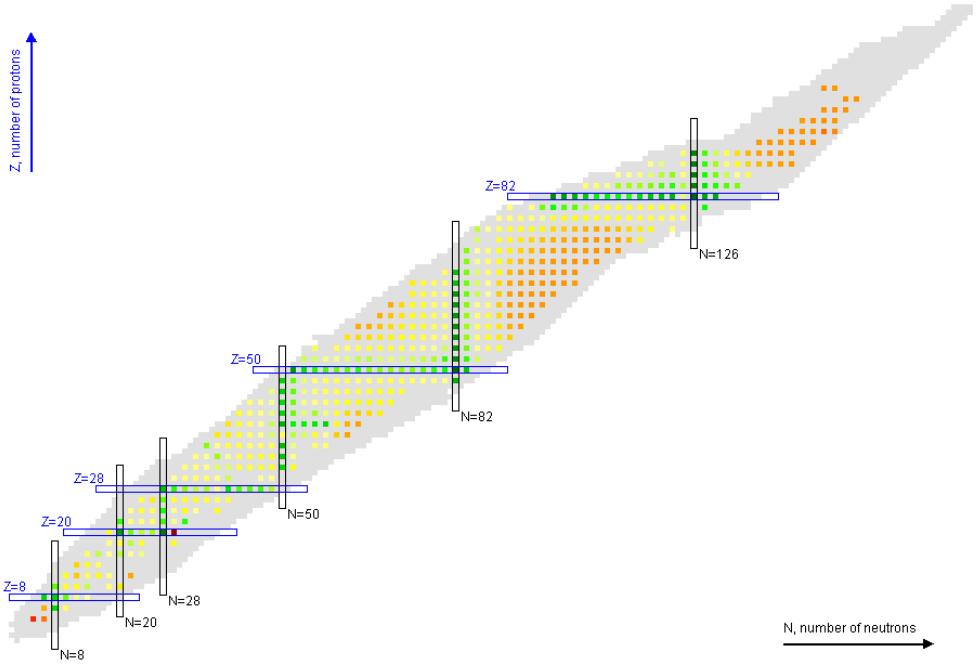

Figure 1.3: Energy ratio $R_{4/2}$ in even-even nuclei. The color code can be roughly read as follows. For yellow nuclei $R_{4/2} \sim 2$, suggesting harmonic vibrational behavior. For orange nuclei $R_{4/2} \sim 10/3$, suggesting rotational behavior. Plot produced using the code ENSDAT, written by R.R. Kinsey, National Nuclear Data Center, Brookhaven National Laboratory, Upton, NY, U.S.A.

probability for a transition involving the motion of only one proton [47]. The reduced transition probability for this transition is given by

$$\begin{aligned} B(E2)_{\mathrm{W}} &\equiv \mathrm{W.\ U.} \\ &= 5.94 \times 10^{-6} A^{4/3} e^2 \mathrm{b}^2, \end{aligned} \tag{1.9}$$

where e is the electron charge. Figure 1.4 shows data taken from [48] on the $E2$ reduced transition probabilities for the mentioned transition. The large values can only be accounted for if many nucleons participate coherently. In the figure, the largest values are observed in heavier midshell nuclei, where the $E2$ reduced transition probabilities lie around $B(E2) \sim A$. In nuclei near shell closures, the effect is not as drastic as in midshell nuclei; nevertheless, the reduced transition rates are still large when compared to the Weisskopf unit. Some of the nuclei shown in this figure will be studied with an EFT approach to collective motion.

The static quadrupole moment of the 2_1^+ state in even-even nuclei also depends on the number of nucleons outside closed shells. This statement can be appreciated in Figure 1.5. It is clear that the magnitude of the quadrupole moments in cadmium and tellurium isotopes, lying near the $Z = 50$ shell closure, are smaller than

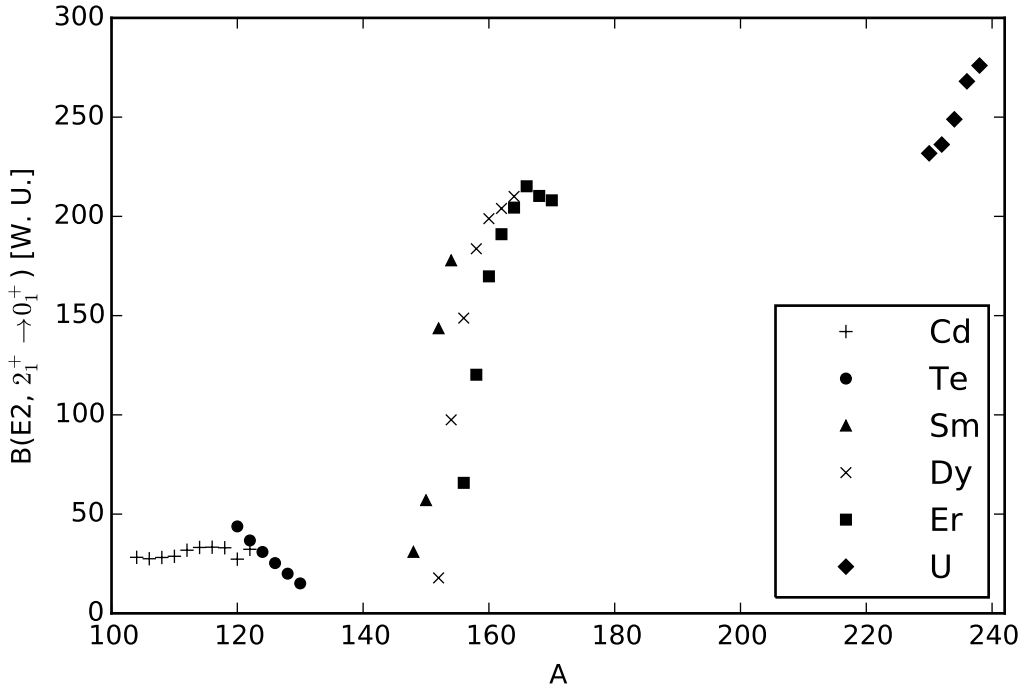

Figure 1.4: $B(E2)$ values for decays from the $2_1^+ \rightarrow 0_1^+$ transition in some even-even nuclei in different isotopic chains. These transition rates are measured in single-particle or Weisskopf units.

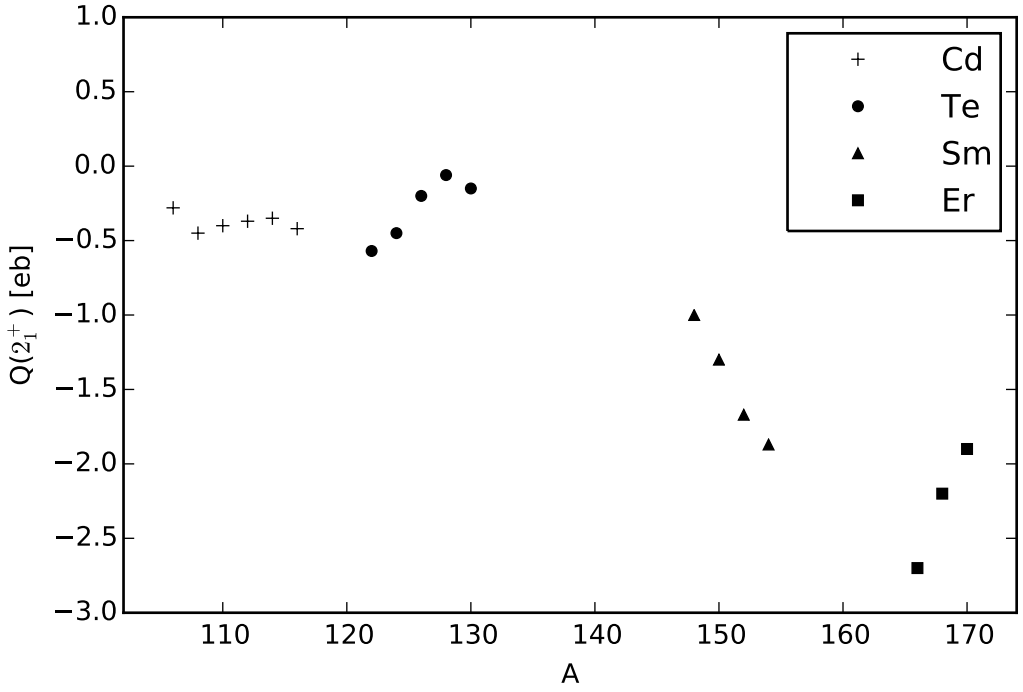

Figure 1.5: Quadrupole moments of the 2_1^+ state in even-even nuclei. The magnitude of this quantity is smaller in nuclei near shell closures than in nuclei far from them. A negative quadrupole moment signals a prolate shape for the 2_1^+ state.

those in samarium or erbium isotopes, lying far from shell closures. Experimental data were taken from Ref. [49]. Notice that all nuclei shown in this figure possess negative quadrupole moments, signaling a prolate shape for the 2_1^+ state. While there exist nuclei with positive quadrupole moments, implying oblate shapes, the vast majority of nuclei possess a negative quadrupole moment.

The difference in the size of the quadrupole moment in nuclei near to and far from shell closures, along with the different patterns of their low-lying spectra, implies different shapes for these systems [24, 25]. Nuclei near shell closures possess spherical symmetry. These systems possess quadrupole vibrational modes of motion (thus explaining the large $E2$ reduced transition probabilities between its low-lying states). The large quadrupole moments in midshell nuclei imply they possess deformed shapes with respect to the sphere. These systems, referred to as deformed nuclei, possess a rotational mode of motion. The energy scale or this mode $E_{\rm rot} \sim \hbar^2 I(I+1)/mR^2$ where m is the mass of the nucleus, R is its linear dimension and I is the angular momentum of the state, is smaller than the energy scale of quadrupole oscillations $E_{\rm vib} \sim \hbar^2/m(\Delta R)^2$ where ΔR is the amplitude of the oscillation. Thus, rotations are the least energetic mode of motion in these nuclei.

1.3 Bohr collective model

In this section some submodels of the Bohr collective model are briefly reviewed [22, 23, 24, 25]. Of particular interest are the harmonic vibrator submodel, the rotor submodel and the adiabatic Bohr model. The first of these submodels is employed to describe the energy spectra and reduced transition probabilities of nuclei near shell closures, assumed to possess spherical symmetry. The others are employed to describe the same properties in heavy midshell nuclei, assumed to posses deformed ground states (particular attention is placed on nuclei that are believed to possess axial symmetry). Predictions from the EFTs for collective motion developed in Chapters 2 and 3 will be compared to the predictions from these submodels of the Bohr collective model.

1.3.1 Oscillations of the nuclear shape and the Bohr collective Hamiltonian

In many-body systems, the energy spectra have frequently been described in terms of different modes associated with oscillations around the equilibrium configuration of the system. In atomic nuclei, these modes may describe the oscillation of, for example, the nuclear surface at low energies and the nuclear matter density at

high energies, among others.

Of particular interest are the low-energy oscillations around the equilibrium nuclear shape, since collective motion in nuclei is explained in terms of them. In his collective model [22], Aage Bohr assumed that the surface of a nucleus can be written as an expansion in terms of spherical harmonics

$$\begin{aligned} R &\equiv R(\theta, \phi) \\ &= R_0 \left[1 + \sum_{\lambda\mu} \alpha_{\lambda\mu} Y_{\lambda\mu}(\theta, \phi) \right], \end{aligned} \tag{1.10}$$

where R_0 is an equilibrium radius, the angles θ and ϕ determine an orientation with respect to the laboratory reference frame, and the expansion coefficients $\alpha_{\lambda\mu}$, referred to as deformation parameters, fulfill the reality condition

$$\alpha_{\lambda\mu} = (-1)^{\mu} \alpha^*_{\lambda-\mu} \tag{1.11}$$

in order for R to be real. The variation with respect to time of the deformation parameters describes the dynamics of the nuclear surface, that is, it describes the oscillations around the equilibrium nuclear shape. These deformation parameters are employed as the DOF in terms of which the Bohr collective model is written [22, 23, 24].

If the equilibrium shape is spherical, and the oscillations around it are small, the kinetic and potential energies of the system are [22, 23]

$$T = \frac{1}{2} \sum_{\lambda\mu} B_{\lambda} \left| \dot{\alpha}_{\lambda\mu} \right|^2, \qquad V = \frac{1}{2} \sum_{\lambda\mu} C_{\lambda} \left| \alpha_{\lambda\mu} \right|^2, \tag{1.12}$$

where the notation $\dot{x}$ is employed to denote the generalized velocity associated to the generalized coordinate x. The momenta canonical to the deformation parameters are

$$\begin{aligned} \pi_{\mu\lambda} &\equiv \partial_{\dot{\alpha}_{\lambda\mu}} L \\ &= \partial_{\dot{\alpha}_{\lambda\mu}} T, \end{aligned} \tag{1.13}$$

where L is the Lagrangian of the surface. The notation $\partial_x \equiv \partial/\partial x$ is employed to denote partial differentiation with respect to the generalized coordinate x. In

terms of them, the Hamiltonian of the nuclear surface can be written as

$$H = \sum_{\lambda\mu} \left(\frac{1}{2B_\lambda} \left|\pi_{\lambda\mu}\right|^2 + \frac{C_\lambda}{2} \left|\alpha_{\lambda\mu}\right|^2 \right), \tag{1.14}$$

with $\lambda \geq 2$. This last condition is explained as follows. Oscillations of order $\lambda = 0$, associated with changes of volume that preserve the shape, are not expected due to the incompressibility of nuclear matter. Also, oscillations of order $\lambda = 1$, associated with translations of the center of mass (for small oscillations), do not describe nuclear excitations.

If only oscillations of order $\lambda = 2$, referred to as quadrupole oscillations, are taken into account, the Hamiltonian takes the form

$$H = \frac{1}{2B} \sum_{\mu} \left(\left|\pi_\mu\right|^2 + B^2\omega^2 \left|\alpha_\mu\right|^2 \right). \tag{1.15}$$

Here, the subindex $\lambda = 2$ was dropped, $\mu = \pm 2, \pm 1, 0$, and $\omega \equiv \sqrt{C/B}$ is the frequency of oscillation.

A more recent approach [25] describes the shape of the nucleus employing the spherical multipole moments of the nuclear charge distribution as DOF. In this case, the DOF of the Bohr collective model can take any real value. They define a point in $\mathbb{R}^5$ that determines the nuclear shape.

The spherical quadrupole moments form a spherical tensor of rank two. Under a SO(3) rotation r defined by the Euler angles θ_i with $i = 1, 2, 3$, they transform as

$$\alpha_\mu \to a_\mu = \sum_\nu \alpha_\nu D^{2*}_{\nu\mu}(\theta_3, \theta_2, \theta_1), \tag{1.16}$$

where $D^2_{\nu\mu}(\theta_3, \theta_2, \theta_1)$ is the matrix representation of the rotation r. The components of this matrix are Wigner D-functions, the properties of which will be discussed in Chapter 3. These DOF transform linearly under SO(3) rotations.

In the body-fixed or intrinsic reference frame, the deformation parameters, denoted by a_μ with $\mu = \pm 2, \pm 1, 0$, take the form a_0, $a_{\pm 1} = 0$ and $a_2 = a_{-2}$ [25]. The dot product of two spherical tensors $\mathcal{M}$ and $\mathcal{N}$ of the same rank, defined by [50]

$$\mathcal{M} \cdot \mathcal{N} = \sum_\mu (-1)^\mu \mathcal{M}_\mu \mathcal{N}_{-\mu}, \tag{1.17}$$

is invariant under rotations. Let us define the rotational invariant β^2 as

$$\begin{aligned}\beta^2 &\equiv \alpha \cdot \alpha \equiv \ a \cdot a \\ &= a_0^2 + 2a_2^2.\end{aligned} \tag{1.18}$$

Thus, β is the SO(5) analogue to the SO(3) radius r, and can take values in the domain $\beta \geq 0$. This coordinate "measures" the deformation of the nucleus ($\beta = 0$ corresponds to spherical shape). The definition of this hyper radius suggests that it is possible to write the spherical quadrupole moments in the intrinsic frame as

$$a_0 = \beta \cos\gamma, \qquad a_2 = \sqrt{\frac{1}{2}}\beta \sin\gamma, \tag{1.19}$$

where γ is a hyperangle. The transformations $\gamma \to -\gamma$ and $\gamma \to \gamma - 2\pi k/3$ with k an integer number, permute the labels of the intrinsic axes without changing the nuclear shape. From here, the domain of γ is restricted to $0 \leq \gamma < \pi/3$ (see Refs. [22, 25] for a more detailed discussion on the domain of γ).

From here, it is possible to write the deformation parameters in the laboratory reference frame in terms of β, γ and the Euler angles θ_1, θ_2 and θ_3. From now on these DOF will be referred to as the β_μ DOF. The nuclear shape is determined by β and γ, while the Euler angles determine its orientation with respect to the laboratory reference frame.

The quantized Hamiltonian of the Bohr collective model is

$$\hat{H} = -\frac{\hbar^2}{2B}\Delta + V, \tag{1.20}$$

where Δ is the Laplacian for $\mathbb{R}^5$, V is a rotationally invariant potential, and B is a mass parameter. In the following sections, let us set $\hbar = 1$ and study some submodels of the Bohr collective model.

With respect to transitions, if a state $|f\rangle$ is a quadrupole excitation of the state $|i\rangle$, the "strength" of an $E2$ transition between them is expected to be large. Such "strength" is measured by the $E2$ reduced transition probability or $B(E2)$ value, given by Fermi's golden rule

$$B(E2, i \to f) = \frac{\left|\langle f||\hat{\mathscr{M}}(E2)||i\rangle\right|^2}{2I_i + 1}. \tag{1.21}$$

Here, the $E2$ operator is defined to be

$$\hat{\mathscr{M}}(E2,\mu) \equiv \frac{Ze}{A}\alpha_\mu, \tag{1.22}$$

where Ze is the nuclear charge and A is the nucleon number.

1.3.2 Harmonic vibrator submodel

For oscillations around a spherical shape, the coordinate β oscillates around the equilibrium value $\beta_0 = 0$. In this case, the potential energy depends only on the rotational invariant β^2, and the Hamiltonian takes the form [25]

$$\begin{aligned}\hat{H} =& -\frac{1}{2B}\Delta + \frac{1}{2}C\beta^2 \\ =& -\frac{1}{2B}\sum_\mu (-1)^\mu \left(\hat{\pi}_\mu\hat{\pi}_{-\mu} + B^2\omega^2\alpha_\mu\alpha_{-\mu}\right),\end{aligned} \tag{1.23}$$

where $\hat{\pi}_\mu \equiv -i\partial_{\alpha^*_\mu}$ and $\omega \equiv \sqrt{C/B}$. This submodel, referred to as the harmonic vibrator submodel, is equivalent to the quantized version of the Hamiltonian in equation (1.15). It is that of a five-dimensional harmonic oscillator.

In order to solve the eigenvalue problem of this Hamiltonian, let us first introduce the quadrupole creation and annihilation operators, denoted by $d^\dagger_\mu$ and d_μ with $\mu = \pm 2, \pm 1, 0$ respectively and defined by

$$d^\dagger_\mu = -\sqrt{\frac{1}{2}}\left[i\ell\hat{\pi}_\mu - \ell^{-1}(-1)^\mu\alpha_{-\mu}\right], \qquad d_\mu = \sqrt{\frac{1}{2}}\left(\ell^{-1}\alpha_\mu + i\ell(-1)^\mu\hat{\pi}_{-\mu}\right), \tag{1.24}$$

where $\ell \equiv (B\omega)^{-1/2}$ is the oscillator length. These operators create and annihilate quanta of the quadrupole vibrational mode, referred to as phonons, and fulfill the commutation relations for bosons

$$[d_\mu, d^\dagger_\nu] = \delta^\nu_\mu. \tag{1.25}$$

In terms of the quadrupole creation and annihilation operators, the Hamiltonian (1.23) takes the form

$$\hat{H} = \omega\left(\sum_\mu d^\dagger_\mu d_\mu + \frac{5}{2}\right). \tag{1.26}$$

Here, the operator

$$\hat{N} = \sum_{\mu} d_{\mu}^{\dagger} d_{\mu} \tag{1.27}$$

counts the total number of phonons N. Thus, the energy spectrum of this submodel is

$$E(N) = N\omega \tag{1.28}$$

after the energy of the ground state is set to zero.

The ground state of the nucleus has zero phonons. This phonon vacuum is denoted by $|0\rangle$. Excited states can be created from it by the successive application of creation operators [25]. More details on how to construct excited states from the phonon vacuum will be given in Chapter 2. For the moment it is only relevant to know that such a construction yields a singlet at the one-phonon level with angular momentum $I = 2$, a triplet at the two-phonon level with angular momenta $I = 0, 2, 4$, and a quintuplet at the three-phonon level with angular momenta $I = 0, 2, 3, 4, 6$. This energy spectrum is shown in Figure 1.6. Here, the energy of the 2_1^+ state was chosen arbitrarily. The energy of any other state is completely determined.

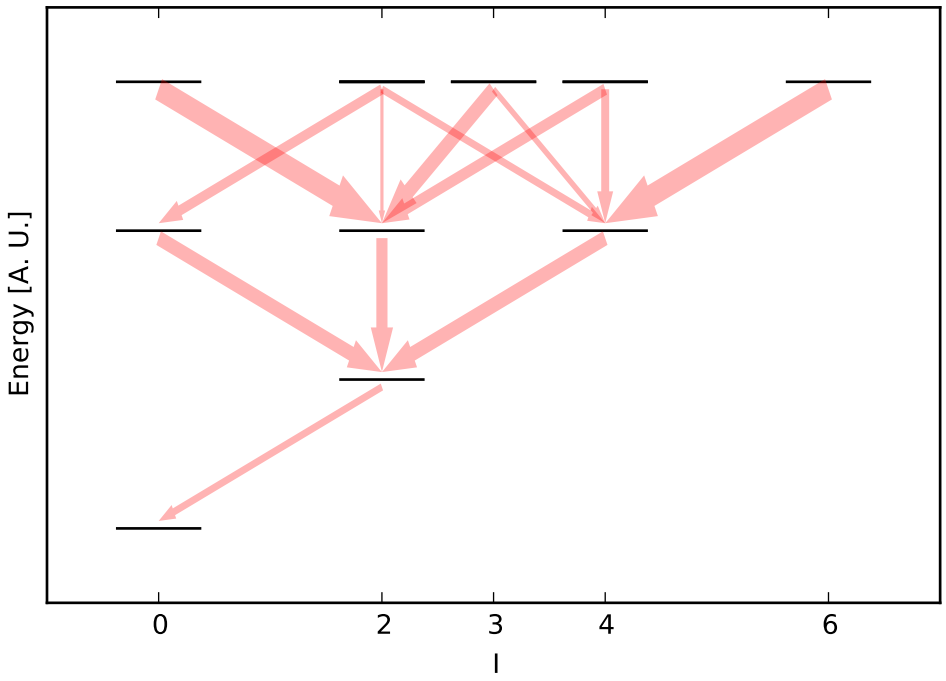

Figure 1.6: Partial energy spectrum and reduced transition probabilities of the harmonic vibrator submodel. The energies are normalized to the energy of the 2_1^+ state. The width of the arrows is proportional to the $B(E2)$ values.

In order to calculate the reduced transition probabilities between the states of the harmonic vibrator submodel, the $E2$ operator (1.22) is written in terms of the quadrupole creation and annihilation operators as

$$\hat{\mathscr{M}}(E2,\mu) = \frac{Ze}{A}\sqrt{\frac{1}{2}}\ell\left[d_\mu + (-1)^\mu d^\dagger_{-\mu}\right]. \tag{1.29}$$

This operator can only couple states for which $\Delta N = \pm 1$ and $\Delta I \leq 2$. The $E2$ reduced transition probabilities for decays from the one- and two-phonon states are

$$\begin{aligned} B(E2, N=1 \to N=0) =& \left(\frac{Ze}{A}\right)^2 \frac{\ell^2}{2}, \\ B(E2, N=2 \to N=1) =& 2B(E2, N=1 \to N=0). \end{aligned} \tag{1.30}$$

The $B(E2)$ values for decays from states up to the three-phonon level are schematically shown in Figure 1.6. The widths of the arrows are proportional to the $B(E2)$ values.

1.3.3 Rotor submodel

In terms of the β_μ DOF, the Laplacian for $\mathbb{R}^5$ takes the form [22, 25]

$$\Delta = \frac{1}{\beta^4}\partial_\beta \beta^4 \partial_\beta + \frac{1}{\beta^2 \sin 3\gamma}\partial_\gamma \sin 3\gamma \partial_\gamma - \sum_i \frac{\hat{I}_i^2}{4\beta^2 \sin^2(\gamma - 2\pi i/3)}, \tag{1.31}$$

where $\hat{I}_i$ with $i = 1, 2, 3$ are the Cartesian components of the angular momentum operator in the intrinsic frame.

If it is assumed that the nucleus possesses a static intrinsic deformation, that is, the values for the coordinates $\beta = \beta_0$ and $\gamma = \gamma_0$ with $\beta_0 \neq 0$ are constants, the Hamiltonian takes the form

$$\begin{aligned} \hat{H} =& -\frac{1}{2B}\Delta \\ =& \frac{1}{2}\sum_i \frac{\hat{I}_i^2}{\mathscr{I}_i}. \end{aligned} \tag{1.32}$$

This Hamiltonian is equivalent to the Hamiltonian of a rigid rotor with moments of inertia given by $\mathscr{I}_i \equiv 4\beta_0^2 \sin^2(\gamma_0 - 2\pi i/3)$.

The value of γ_0 determines the shape of the nucleus. For $\gamma_0 = 0, \pi/6, \pi/3$ two moments of inertia are equal, and the nucleus is a symmetric top. Any other

value of γ_0 yields the Hamiltonian of an asymmetric top. In the former case $\mathscr{I}_1 = \mathscr{I} = \mathscr{I}_2$ and the Hamiltonian is further simplified to

$$\hat{H} = \frac{1}{2\mathscr{I}}\hat{I}^2 + \frac{1}{2}\left(\frac{1}{\mathscr{I}_3} - \frac{1}{\mathscr{I}}\right)\hat{I}_3^2. \tag{1.33}$$

In what follows we restrict the discussion to nuclei with a prolate shape, characterized by $\gamma_0 = 0$. In this case, the moment of inertia $\mathscr{I}_1 = 0$, reflecting the fact that a quantum system cannot rotate around a symmetry axis. Thus, the projection of the angular momentum onto such axis is zero, and the Hamiltonian reduces to

$$\hat{H} = \frac{1}{2\mathscr{I}}\hat{I}^2. \tag{1.34}$$

Consequently, the energy spectrum of a prolate nucleus is

$$E(I) = \frac{1}{2\mathscr{I}}I(I+1), \tag{1.35}$$

and the wave functions of its states are

$$\langle \Omega | IMK = 0 \rangle = \sqrt{\frac{2I+1}{8\pi^2}} D^I_{M0}(\Omega), \tag{1.36}$$

where only states with even angular momentum I are allowed due to the symmetries of the system (more details on this will be given in Chapter 3). The label K is the projection of the angular momentum onto the symmetry axis.

For prolate nuclei, the $E2$ operator (1.22) takes the form [25]

$$\hat{\mathscr{M}}(E2,\mu) = \frac{Ze}{A}\beta_0 D^2_{\mu 0}(\Omega). \tag{1.37}$$

The $B(E2)$ values for decays are [25]

$$B(E2, I_i \to I_f) = \left(\frac{Ze}{A}\right)^2 \beta_0^2 \left(C^{I_f 0}_{I_i 020}\right)^2, \tag{1.38}$$

where the Clebsch-Gordan coefficient $C^{IM}_{I_1 M_1 I_2 M_2}$ represents the probability amplitude that the angular momenta I_1 and I_2 with projections M_1 and M_2 respectively are coupled into an angular momentum I with projection M [50].

1.3.4 Adiabatic Bohr model

If the coordinate β and γ oscillate around their equilibrium values, β_0 and $\gamma_0 = 0$ in prolate nuclei, the Laplacian for $\mathbb{R}^5$ can approximately be written as [25]

$$\Delta \approx \partial_\beta^2 + \frac{1}{\beta_0^2 \gamma} \partial_\gamma \gamma \partial_\gamma - \frac{\hat{I}_3^2}{4\beta_0^2 \gamma^2} - \frac{\hat{I}^2 - \hat{I}_3^2}{3\beta_0^2}. \tag{1.39}$$

This approximation is valid if the potential $V \equiv V(\beta, \gamma)$ has a deep minimum at the equilibrium values β_0 and $\gamma_0 = 0$. In this case, the potential can be expanded in a Taylor series around the minimum, taking the approximate form

$$V(\beta, \gamma) \approx V(\beta_0, 0) + \frac{1}{2} B \omega_\beta^2 (\beta - \beta_0)^2 + \frac{1}{2} B \beta_0^2 \omega_\gamma^2 \gamma^2. \tag{1.40}$$

For these approximations the Hamiltonian takes the form $\hat{H}_\beta + \hat{H}_\gamma + \hat{H}_{\text{rotor}}$. Here, the β-dependent Hamiltonian

$$\hat{H}_\beta = -\frac{1}{2B} \partial_\beta^2 + \frac{1}{2} B \omega_\beta^2 (\beta - \beta_0)^2 \tag{1.41}$$

is the Hamiltonian of a harmonic oscillator with frequency ω_β [51]. Its states are denoted by $|n_\beta\rangle$, where n_β is the number of excited quanta of the harmonic oscillator.

The γ-dependent Hamiltonian

$$\hat{H}_\gamma = -\frac{1}{2B\beta_0^2} \left(\frac{1}{\gamma} \partial_\gamma \gamma \partial_\gamma - \frac{\hat{I}_3^2}{4\gamma^2} \right) + \frac{1}{2} B \beta_0^2 \omega_\gamma^2 \gamma^2 \tag{1.42}$$

is the Hamiltonian of a two-dimensional harmonic oscillator with frequency ω_γ [51]. Its states are denoted by $|n_\gamma K/2\rangle$, where n_γ and $K/2$ are the number of excited radial and angular quanta of the two-dimensional harmonic oscillator, respectively. Notice that the operator $(\hat{I}_3/2\gamma)^2$ appears in the Hamiltonian (1.42), giving rise to the factor $1/2$ in the quantum number $K/2$. The quantum number K, can only take even values, as will be discussed later.

The part of the Hamiltonian depending on the Euler angles θ_1, θ_2 and θ_3

$$\hat{H}_{\text{rotor}} = \frac{1}{6B\beta_0^2} \left(\hat{I}^2 - \hat{I}_3^2 \right) \tag{1.43}$$

is the Hamiltonian of a rigid rotor [51]. Its states are denoted by $|IMK\rangle$, where the labels are the angular momentum of the state, and its projections onto the

laboratory and intrinsic z-axis respectively. The wave functions for states with $K = 0$ are those in Equation (1.36). For other values of K the wave functions are

$$\langle \Omega | IMK \rangle = \sqrt{\frac{2I+1}{16\pi^2}} \left[D^I_{MK}(\Omega) + (-1)^I D^I_{M-K}(\Omega) \right] . \tag{1.44}$$

This functional form is a consequence of the positive $\mathcal{R}$-parity possessed by the ground state, as rotations of π around any axis perpendicular to the symmetry axis do not change the wave function.

Within this submodel, referred to as adiabatic Bohr model, the energy spectrum is

$$E(n_\beta, n_\omega, I, K) = \omega_\beta \left(n_\beta + \frac{1}{2} \right) + \omega_\gamma \left(2n_\gamma + \frac{K}{2} + 1 \right) + \frac{I(I+1) - K^2}{6B\beta_0^2}. \tag{1.45}$$

It consist of rotational bands on top of harmonic excitations, referred to as bandheads. The rotational bands on top of the bandheads with quantum numbers $n_\beta = 1$, $n_\gamma = 0$, $K = 0$ and $n_\beta = 0$, $n_\gamma = 0$, $K = 2$ are referred to as β and γ bands respectively. A partial energy spectrum of the adiabatic Bohr model is shown in Figure 1.7. There, the energy of the 2_1^+ state and the energies of the bandheads of the β and γ bands were arbitrarily chosen. The energy of the rest

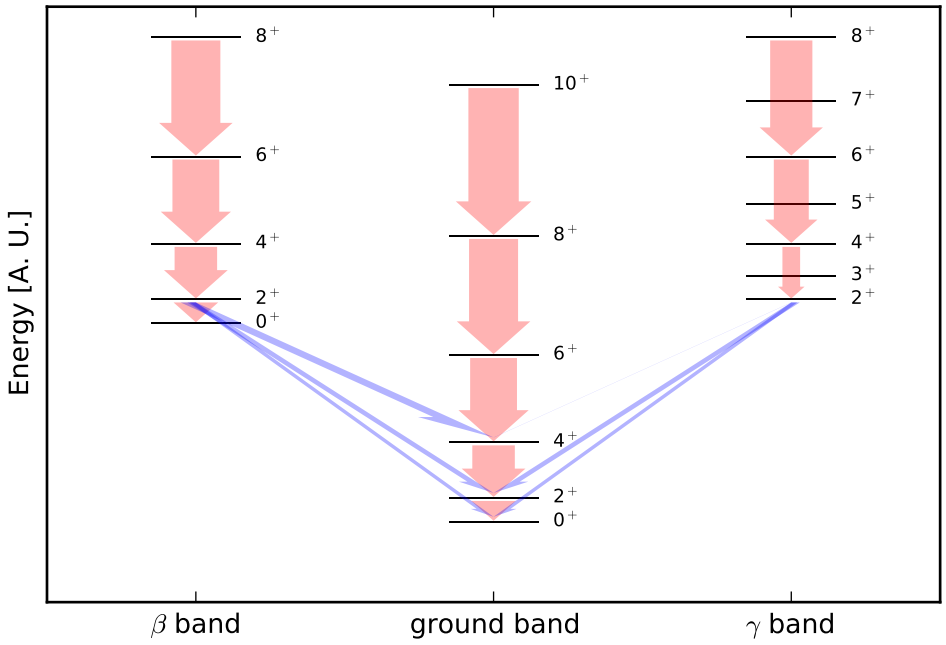

Figure 1.7: Partial energy spectrum and reduced transition probabilities of the adiabatic Bohr model. The energies of the bandheads of the β and γ bands was arbitrarily fixed. The width of the arrows is proportional to the $B(E2)$ values.

of the states is completely determined. Notice that, from the form of the wave functions (1.44), bands with $K = 0$ can only possess states with even values of I, while bands with $K \neq 0$ can possess states with both even and odd values of I.

Within this approximation, and for prolate nuclei, the $E2$ operator (1.22) takes the approximate form [25]

$$\hat{\mathscr{M}}(E2,\mu) = \frac{Ze}{A}\left\{\beta_0 D^2_{\mu 0}(\Omega) + (\beta - \beta_0)\, D^2_{\mu 0}(\Omega) + \sqrt{\frac{1}{2}}\beta_0\gamma\left[D^2_{\mu 2}(\Omega) + D^2_{\mu -2}(\Omega)\right]\right\}. \tag{1.46}$$

The first term induces transitions between states fulfilling the conditions $\Delta n_\beta = \Delta n_\gamma = \Delta K = 0$. In other words, it induces inband transitions. The second and third terms induce interband transitions. The former can couple states for which $\Delta n_\beta = \pm 1$, and the later can couple states for which $\Delta K = \pm 2$. Thus, these terms can be employed to describe decays from the β and γ band to the ground band respectively. The $E2$ reduced transition probabilities for inband decays are [25]

$$B(E2, i \to f) = \left(\frac{Ze}{A}\right)^2 \beta_0^2 \left(C^{I_f K}_{I_i K 20}\right)^2. \tag{1.47}$$

The $E2$ reduced transition probabilities for interband decays from the β and γ bands to the ground band are [25]

$$B(E2, i_\beta \to f_g) = \left(\frac{Ze}{A}\right)^2 \frac{1}{2B\omega_\beta}\left(C^{I_f 0}_{I_i 0 20}\right)^2 \tag{1.48}$$

and

$$B(E2, i_\gamma \to f_g) = \left(\frac{Ze}{A}\right)^2 \frac{1}{B\omega_\gamma}\left(C^{I_f 0}_{I_i 2 2 -2}\right)^2, \tag{1.49}$$

respectively. For $\omega_\beta \sim \omega_\gamma$, decays from the γ band are a factor two stronger than those from the β band.

Some $E2$ reduce transition probabilities between the states of the adiabatic Bohr model are displayed in Figure 1.7. There, the width of the arrows is proportional to the $B(E2)$ values.

1.4 Motivation of this study

The different submodels of the Bohr collective model successfully describe the low-lying spectra of spherical and deformed heavy nuclei in terms of quadrupole DOF. The low-lying spectrum of ^{120}Te, shown in Figure 1.2, and other nuclei near

shell closures exhibit states that can be identified with those predicted by the harmonic vibrator submodel, shown in Figure 1.6, up to the three-phonon level. At that level, states that cannot be identified with quadrupole excitations appear. Similarly, if one compares the spectrum of ^{168}Er, shown in Figure 1.1, and other rotational nuclei with the spectrum predicted by the adiabatic Bohr model, shown in Figure 1.7, the ground, β and γ rotational bands can be easily identified. At high energies, states that can neither be identified as β or γ excitations, or as rotations on top of a bandhead, appear.

Besides predictions for the energy spectra, predictions for electromagnetic reduced transition probabilities with different multipolarities arise from the Bohr collective model. This work focuses on $E2$ transitions. In nuclei near shell closures, experimental data on $E2$ reduced transition probabilities for decays from yrast states up to the two-phonon level are in agreement with those predicted by the harmonic vibrator submodel. However, decays from non yrast two-phonon states have small $E2$ reduced transition probabilities [52]. The decay pattern from the three-phonon candidates in these nuclei is completely inconsistent with that of Figure 1.6.

In rotational nuclei, experimental data on $E2$ reduced transition probabilities for inband decays are in agreement with those predicted by the adiabatic Bohr model. Experimental data on interband decays from the β and γ bands to the ground band are qualitatively in agreement with the model, exhibiting much smaller $E2$ reduced transition probabilities than inband decays. Nevertheless, the Bohr collective model tends to overpredict the reduce transition probabilities for interband transitions by factors two to ten [25].

The EFTs for collective motion described in the following chapters propose a solution to these problems. The ability to estimate and quantify the theoretical uncertainty within an EFT allows us to statistically compare experimental data to calculations. This comparison is used to establish when a data set is consistent with a particular EFT, as will be shown in Chapter 2.

Let us comment about the experimental data that will be compared to the EFT predictions. These data is taken from Nuclear Data Sheets, where the reported values for several observables are obtained after the evaluation of results arising from diverse experiments. In the case of energy spectra and electric quadrupole transitions strengths, these experiments involve the measurement of photons resulting from the de-excitation of atomic nuclei. The population of the excited states of

the nucleus of interest can be achieved via different processes. Some examples of these processes are Coulomb excitation [53, 54, 55, 56, 57, 58, 59, 60, 61, 62, 63] and inelastic neutron scattering [64, 65, 66, 67, 68, 69]. The lifetimes and spins of excited states and the multipolarity of transitions are extracted from the angular distributions of the emitted photons. For more details on the experimental methods from which the spectrum and transition strengths of a particular nucleus are measured, we refer the reader to the references within the Nuclear Data Sheets for such system.

Within EFT approaches transition operators that are consistent with the Hamiltonian. In Chapter 2, the systematic construction of the $E2$ operator via nonminimal coupling terms allows us to describe the large static quadrupole moments, and $E2$ reduced transition probabilities between states with the same phonon number, exhibited by nuclei near shell closures. In Chapter 3, the $E2$ operators within the EFT are shown to be richer in structure that the $E2$ operator defined by Bohr [24, 25], allowing us to precisely describe interband transitions.

2
VIBRATIONAL NUCLEI

Some nuclei near shell closures, that are assumed to be spherical, exhibit energy spectra with a great resemblance to that predicted by the harmonic vibrator submodel of the Bohr collective model up to the two-phonon level, suggesting quadrupole oscillations of the nuclear shape as the least energetic mode in these systems, with an excitation energy ω. Figure 1.2 shows the full spectrum of ^{120}Te below 2.5 MeV. In this nucleus, as well as in other nuclei near shell closures, the appearance of states that cannot be characterized as multiphonon excitations takes place around the three-phonon level. Within the harmonic vibrator submodel of the Bohr collective model, the energies of multiphonon excitations can be described. However, other DOF are required to describe states that are not classified as multiphonon excitations. Also, the data on $E2$ reduced transition probabilities for decays from states characterized as multiphonon excitations are sometimes small when compared with predictions by the Bohr collective model [70, 52] (this is particularly true for non yrast states). In this chapter, the EFT for quadrupole nuclear vibrations developed in Ref. [30] is described in detail. The expansion parameter of the EFT scales as $\omega/\Lambda \sim 1/3$, allowing for the description of the energies, transitions and static quadrupole moments in these systems up to the two-phonon level. In Ref. [30], Bayesian methods were employed to quantify the theoretical uncertainty in calculated energies and electric quadrupole reduced transition probabilities for decays from states up to the two-phonon level. This theoretical uncertainty has a simple statistical interpretation, and allows us to meaningfully compare experimental data and calculations within the EFT. The consistency between experimental data and the EFT allow us to characterize the states up to the two-phonon level as quadrupole excitations.

2.1 Effective field theory for nuclear vibrations

In this Section, the EFT for nuclear vibration is developed up to NLO. The low-energy spectra of some nuclei near shell closures suggest quadrupole vibrations as the least energetic mode of motion. The effective DOF create or annihilate bosons, referred to as phonons, which are the quanta of this mode. At LO, the Hamiltonian is equivalent to the harmonic vibrator submodel of the Bohr collective model [22, 23, 24, 25], and the predicted energy spectrum consist of multiplets with

energies linear in the total number of phonons. The power counting is employed to identify all the relevant correction terms at NLO. These corrections account for deviations from the LO behavior. The systematic construction of the Hamiltonian and Bayesian statistics allow one to estimate the probability distribution function (pdf) for the omitted contribution to the energies at each order. These distributions allow us to define intervals with an specific degree of belief (dob), which are employed to quantify the theoretical uncertainty.

2.1.1 Phonon operators as DOF and the leading order Hamiltonian

The low-lying spectra of even-even nuclei near shell closures, assumed to be spherical, strongly suggest these systems undergo vibrations of different polarities, with those of quadrupole character being the least energetic. The separation of scales between the excitation energy of quadrupole vibrations ω and the excitation energies of other modes $\Lambda \approx 3\omega$, motivates the study of these systems within an EFT for vibrations, which employs quadrupole boson creation and annihilation operators as building blocks. The boson creation and annihilation operators fulfill the boson commutation relations

$$\left[d_\mu, d_\nu^\dagger\right] = \delta_\mu^\nu, \tag{2.1}$$

with μ, $\nu = \pm 2, \pm 1, 0$. The creation and annihilation operators create and annihilate quanta of the quadrupole vibrational mode, respectively.

In order to construct scalars from the creation and annihilation operators, let us study a few spherical tensors. The angular momentum operator $\hat{\mathbf{I}}$ is

$$\hat{\mathbf{I}} = \sqrt{10}\left(d^\dagger \otimes \tilde{d}\right)^{(1)}, \tag{2.2}$$

where

$$\tilde{d}_\mu = (-1)^\mu d_{-\mu}, \tag{2.3}$$

and the tensor product $(\mathcal{M} \otimes \mathcal{N})^{(I)}$ of the tensors $\mathcal{M}$ and $\mathcal{N}$ with ranks I_1 and I_2 respectively, is the tensor $\mathcal{I}$ of rank I defined by

$$\mathcal{I}_M = \sum_{M_1 M_2} C^{IM}_{I_1 M_1 I_2 M_2} \mathcal{M}_{M_1} \mathcal{N}_{M_2}. \tag{2.4}$$

The dot product of two tensors $\mathcal{M}$ and $\mathcal{N}$ of the same rank I is

$$\mathcal{M} \cdot \mathcal{N} = \sqrt{2I+1}(\mathcal{M} \otimes \mathcal{N})^{(0)}. \tag{2.5}$$

The spherical components of the angular momentum operator $\hat{I}_\mu$ with $\mu = \pm 1, 0$ fulfill the commutation relations

$$[I_{\pm 1}, I_0] = \mp I_{\pm 1} = -[I_0, I_{\pm 1}], \qquad [I_{+1}, I_{-1}] = I_0 = -[I_{-1}, I_{+1}]. \tag{2.6}$$

Also, the commutation relations between the components of the angular momentum operator and the components of a spherical tensor $\mathcal{I}$ of rank I are

$$\left[\hat{I}_\mu, \mathcal{I}_\nu\right] = \sqrt{I(I+1)} C^{2\nu+\mu}_{2\nu 1\mu} \mathcal{I}_{\nu+\mu}. \tag{2.7}$$

Because the creation operators fulfill the commutation relations

$$\left[\hat{I}_\mu, d^\dagger_\nu\right] = \sqrt{6} C^{2\nu+\mu}_{2\nu 1\mu} d^\dagger_{\nu+\mu}, \tag{2.8}$$

they are the components of a spherical tensor of rank two. Similar commutation relations are fulfilled by the operators defined in Equation (2.3). From here, rotationally invariant terms can be constructed by coupling any number of these tensors to form a scalar. The simplest Hamiltonian that one can construct from these tensors is

$$\begin{aligned} \hat{H}_{\mathrm{LO}} &= \omega \left(d^\dagger \cdot \tilde{d}\right) \\ &= \omega \sum_\mu d^\dagger_\mu d_\mu \\ &\equiv \omega \hat{N}, \end{aligned} \tag{2.9}$$

where the operator

$$\hat{N} \equiv d^\dagger \cdot \tilde{d} \tag{2.10}$$

counts the total number of phonons N in a given state.

Thus, the LO Hamiltonian of the EFT for nuclear vibrations is equivalent to the harmonic vibrator submodel of the Bohr collective model [22, 23, 24, 25]. The eigenvalue problem becomes

$$\hat{H}_{\mathrm{LO}} |\psi\rangle = E_{\mathrm{LO}} |\psi\rangle, \tag{2.11}$$

with

$$\begin{aligned} E_{\mathrm{LO}} &\equiv E_{\mathrm{LO}}(N) \\ &= \omega N. \end{aligned} \tag{2.12}$$

Here, ω is a LEC and must be fit to data. It represents the energy scale of the quadrupole vibrational mode. This spectrum, consisting of multiplets with energies linear in the number of phonons, is expected below the breakdown energy scale Λ, where different excitation modes are available to the system.

The states of the LO Hamiltonian are labeled by the quantum numbers of the symmetry subgroups in the chain

$$\begin{array}{ccccccccc} \mathrm{U}(5) & \supset & \mathrm{SO}(5) & \supset & \mathrm{U}(3) & \supset & \mathrm{SO}(3) & \supset & \mathrm{SO}(2) \\ N & & v & & \nu & & I & & M \end{array} .$$

Here ν is a radial quantum number, I and M are the angular momentum and its projection onto the z-axis, respectively, and the seniority v is the SO(5) analog of the angular momentum. From now on, we refer to the SO(3) angular momentum as spin.

The ground state of the system is the phonon vacuum, denoted by $|0\rangle$. A state with N excited quanta is created from the ground state by the successive application of N creation operators. Given the quantum numbers v and ν, the highest-weight state is defined by

$$\begin{aligned} |\psi_{\mathrm{hw}}\rangle &= |N = v + 2\nu, v, \nu, I = 2v, M = 2v\rangle \\ &\propto \left(d^\dagger \cdot d^\dagger\right)^\nu \left(d_2^\dagger\right)^v |0\rangle. \end{aligned} \tag{2.13}$$

The rest of the states with $N = v + 2\nu$ phonons can be reached from the highest-weight states by the application of lowering operators defined by $\hat{C}_{mn} \equiv d_m^\dagger \tilde{d}_n$ with $m < n$. This construction yields a singlet with spin $I = 2$ at the one-phonon level, a triplet with spins $I = 0, 2, 4$ at the two-phonon level, and a quintuplet with spins $I = 0, 2, 3, 4, 6$ at the three-phonon level. For more details on this construction see Ref. [25].

2.1.2 Power counting and the next-to-leading order Hamiltonian

Besides quadrupole vibrations, nuclear systems near shell closures posses high-energy excitation modes. The effects of the omitted DOF describing them, can be systematically included in the EFT as corrections to the Hamiltonian that account for deviations from the behavior expected for quadrupole vibrators.

There is an infinite number of terms consistent with the symmetries of these systems that correct the LO Hamiltonian. For the correction to be systematic, the

power counting is employed to estimate the size of each term as follows. First, the quadrupole DOF $\tilde{\alpha}$ and their canonical momenta π are introduced. These DOF are defined by

$$\tilde{\alpha}_\mu = \sqrt{\frac{1}{2}}\ell\left(d^\dagger_\mu + \tilde{d}_\mu\right), \qquad \pi_\mu = i\sqrt{\frac{1}{2}}\ell^{-1}\left(d^\dagger_\mu - \tilde{d}_\mu\right), \tag{2.14}$$

where $\ell \equiv (B\omega)^{-1/2}$ is the oscillator length and B is a mass parameter. Notice that, unlike the creation and annihilation operators, these are dimensionful DOF. They fulfill the commutation relations

$$[\pi_\mu, \alpha_\nu] = -i\delta^\nu_\mu, \qquad \tilde{\alpha}_\mu = (-1)^\mu \alpha_{-\mu}. \tag{2.15}$$

Both $\tilde{\alpha}$ and π are spherical tensors of rank two. In terms of them, the LO Hamiltonian can be written as

$$\hat{H}_{\rm LO} = \frac{1}{2B}\left(\pi\cdot\pi + B^2\omega^2\tilde{\alpha}\cdot\tilde{\alpha}\right) - \frac{5}{2}\omega. \tag{2.16}$$

From this expression, it is evident that the scale of the quadrupole DOF and their conjugate momenta at the N-phonon level is

$$\tilde{\alpha} \sim \sqrt{N}\ell, \qquad \pi \sim \sqrt{N}\ell^{-1}. \tag{2.17}$$

At the energy scale Λ where the EFT breaks, the scale of the quadrupole DOF is such that

$$\begin{aligned} B\omega^2\tilde{\alpha}^2 \sim \Lambda \implies \tilde{\alpha} \sim \sqrt{\frac{\Lambda}{\omega}}\ell, \\ \frac{\pi^2}{B} \sim \Lambda \implies \pi \sim \sqrt{\frac{\Lambda}{\omega}}\ell^{-1}. \end{aligned} \tag{2.18}$$

Next, the corrections to the Hamiltonian are written as rotationally invariant terms of the form $C_{mn}\pi^m\tilde{\alpha}^n$, with $m+n>2$. At the breakdown scale Λ, the energy shift due to these corrections is such that N-phonon states cannot be distinguished from states with $N\pm 1$ phonons, that is,

$$C_{mn}\pi^m\tilde{\alpha}^n \sim \omega \Rightarrow C_{mn} \sim \ell^{m-n}\left(\frac{\omega}{\Lambda}\right)^{\frac{m+n}{2}}\omega. \tag{2.19}$$

From here, the energy correction below the breakdown scales as

$$C_{mn}\pi^m\tilde{\alpha}^n \sim Q^{\frac{m+n}{2}}\omega. \tag{2.20}$$

Here $Q \equiv (N\omega/\Lambda)$ is a small parameter. It is important to note that terms with even or odd values of $m+n$ correct the energies at first or second order in perturbation theory respectively, which implies the energy shift due to terms with even and odd values of $m+n$ scales as $Q^{(m+n)/2}\omega$ and $Q^{m+n}\omega$, respectively.

According to this naive analysis, the NLO correction to the energies have $m+n=4$ and scale as $Q^2\omega$. The corresponding terms are quartic in the quadrupole DOF. Within the collective model, terms cubic in the quadrupole DOF had been used as NLO corrections [71, 72, 73, 74, 75]. Once the size of the NLO correction is known, it can be written as a linear combination of rotationally invariant terms with two creation and two annihilation operators, since only terms that do not change N are diagonal when acting on the states of the LO Hamiltonian.

There are many ways to couple $d^\dagger$ and $\tilde{d}$ to a scalar. Since these are noncommuting tensors, the relations between the different coupling schemes are [50]

$$\begin{aligned}\left(d^\dagger \otimes \tilde{d}\right)^{(I)} \cdot \left(d^\dagger \otimes \tilde{d}\right)^{(I)} &= (-1)^I \sqrt{\frac{2I+1}{5}} \left(\left(d^\dagger \otimes \tilde{d}\right)^{(I)} \otimes d^\dagger\right)^{(2)} \cdot \tilde{d} \\ &= (-1)^I \sqrt{\frac{2I+1}{5}} d^\dagger \cdot \left(\tilde{d} \otimes \left(d^\dagger \otimes \tilde{d}\right)^{(I)}\right)^{(2)},\end{aligned} \tag{2.21}$$

with $I = 0, 1, 2, 3, 4$. These relations imply that it is possible to write all the required terms as tensor products of the form $(d^\dagger \otimes \tilde{d})^{(I)} \cdot (d^\dagger \otimes \tilde{d})^{(I)}$. Terms of this form can be written as the linear combination [50]

$$\begin{aligned}\left(d^\dagger \otimes \tilde{d}\right)^{(I)} \cdot \left(d^\dagger \otimes \tilde{d}\right)^{(I)} = \sum_i (2I+1) \left\{ \begin{array}{ccc} 2 & 2 & I \\ 2 & 2 & i \end{array} \right\} \left(d^\dagger \otimes d^\dagger\right)^{(i)} \cdot \left(\tilde{d} \otimes \tilde{d}\right)^{(i)} \\ - \frac{2I+1}{5} \left(d^\dagger \cdot \tilde{d}\right),\end{aligned} \tag{2.22}$$

where the symbol between braces is a $6j$ symbol [50]. The last equation implies that the NLO correction can be written in terms of $(d^\dagger \otimes d^\dagger)^{(i)} \cdot (\tilde{d} \otimes \tilde{d})^{(i)}$ with $i = 0, 2, 4$, and $\hat{N}$. Thus, there are three different linearly independent terms. We choose

$$\begin{aligned}\hat{N}^2 &= \left(d^\dagger \cdot \tilde{d}\right)^2, \\ \hat{\Lambda}^2 &= -\left(d^\dagger \cdot d^\dagger\right)\left(\tilde{d} \cdot \tilde{d}\right) + \hat{N}^2 - 3\hat{N}, \\ \hat{I}^2 &= 10 \left(d^\dagger \otimes \tilde{d}\right)^{(1)} \cdot \left(d^\dagger \otimes \tilde{d}\right)^{(1)}\end{aligned} \tag{2.23}$$

as the linearly independent terms required to write the NLO correction. Here the

operator $\hat{\Lambda}$ is the SO(5) analog of the angular momentum operator $\hat{I}$ [25]. The action of these operators in the LO states is

$$\begin{aligned}\hat{N}^2|Nv\nu IM\rangle &= N^2|Nv\nu IM\rangle,\\ \hat{\Lambda}^2|Nv\nu IM\rangle &= v(v+3)|Nv\nu IM\rangle,\\ \hat{I}^2|Nv\nu IM\rangle &= I(I+1)|Nv\nu IM\rangle.\end{aligned} \tag{2.24}$$

Thus, at NLO the Hamiltonian takes the form $\hat{H}_{\mathrm{NLO}} = \hat{H}_{\mathrm{LO}} + \Delta\hat{H}_{\mathrm{NLO}}$ where

$$\Delta\hat{H}_{\mathrm{NLO}} = C_N\hat{N}^2 + C_v\hat{\Lambda}^2 + C_I\hat{I}^2. \tag{2.25}$$

Here C_N, C_v and C_I are LECs. The action of the NLO Hamiltonian on the states of the LO Hamiltonian yields

$$\hat{H}_{\mathrm{NLO}}|Nv\nu IM\rangle = E_{\mathrm{NLO}}|Nv\nu IM\rangle, \tag{2.26}$$

with

$$\begin{aligned}E_{\mathrm{NLO}} &\equiv E_{\mathrm{NLO}}(N,v,I)\\ &= \omega N + C_N N^2 + C_v v(v+3) + C_I I(I+1).\end{aligned} \tag{2.27}$$

All the LECs are simultaneously fit to data up to the two-phonon level during NLO fits.

2.1.3 Energy uncertainty quantification

The ability to estimate the theoretical uncertainty is a highlight of EFT approaches. At a given order, this uncertainty arises due to the omission of high-order terms in the Hamiltonian or any other operator. In this section, Bayesian statistics are employed to go beyond and quantify the theoretical uncertainty in the LO and NLO spectra following the method proposed by Furnstahl et al. in Refs. [38, 40].

Within the EFT, the energy of any state below the breakdown scale Λ can be written as an effective expansion in powers of the small parameter Q as

$$E = \omega N + \omega\sum_i \mathscr{C}_i Q^i, \tag{2.28}$$

with $i \geq 2$. The LO coefficient ω sets the energy scale of quadrupole vibrations, while the state-dependent expansion coefficients $\mathscr{C}_i$ are expected to be of order

one. At a given order k, the normalized residual $\Delta_k^{(M)}$, defined by

$$\Delta_k^{(M)} = \sum_{m=k+1}^{k+M} \mathscr{C}_m Q^m, \tag{2.29}$$

is the uncertainty in the calculated energies at such order. Bayesian statistics can be employed to calculate the pdf for $\Delta_k^{(M)}$, from which the uncertainty will be quantified, as follows. Under the assumption that the expansion coefficients $\mathscr{C}_i$ are independent of each other, the application of Bayes' theorem yields the pdf for the normalized residual (2.29) given the coefficients ω and $\mathscr{C}_n$ with $n \leq k$ [40]

$$p_M\left(\Delta|\mathscr{C}_n\right) = \frac{\int_0^\infty dc\, p_M(\Delta|c) \left[\prod_n^k \mathrm{pr}(\mathscr{C}_n|c)\right] \mathrm{pr}(c)}{\int_0^\infty dc \left[\prod_n^k \mathrm{pr}(\mathscr{C}_n|c)\right] \mathrm{pr}(c)}, \tag{2.30}$$

where we have assumed that the LO coefficient ω have a precise value, that is, it does not have a pdf (or it has a delta function pdf), the pdf $p_M(\Delta|c)$ is given by

$$p_M(\Delta|c) = \int_{-\infty}^{\infty} \left[\prod_{m=k+1}^{k+M} d\mathscr{C}_m \,\mathrm{pr}(\mathscr{C}_m|c)\right] \delta\left(\Delta - \Delta_k^{(M)}\right), \tag{2.31}$$

and c is a width parameter. The assumption for the expansion coefficients being of order $\mathcal{O}(1)$ is contained in the functional form of the pdf for the expansion coefficients $\mathscr{C}_i$ given a width parameter c $\mathrm{pr}(\mathscr{C}_i|c)$, and the pdf for such parameter $\mathrm{pr}(c)$. These pdfs are referred to as priors.

Let us discuss the functional form of these priors. Factoring out the scale ω in the effective expansion (2.28) allows us to employ a log-normal pdf for c [40]

$$\mathrm{pr}(c) = \frac{1}{\sqrt{2\pi}Rc} e^{-\frac{\log^2 c}{2R^2}}, \tag{2.32}$$

where R is the width of this distribution. This choice is consistent with the expectation for the coefficients $\mathscr{C}_i$ to be of order one. For example, if $R = \log\alpha$ with $\alpha > 1$, then c has a 68% probability to lie in the interval $[1/\alpha, \alpha]$. Recall that c will be employed as a width in the pdfs for the expansion coefficients $\mathscr{C}_i$. Varying α from 1.5 to 3 does not change the results significantly.

Let us test two different pdfs for the expansion coefficients $\mathscr{C}_i$ given c. The

chosen priors are a hard-wall (hw) pdf

$$\mathrm{pr}(\mathscr{C}_i|c) = \frac{1}{2c}\Theta\left(c - |\mathscr{C}_i|\right), \tag{2.33}$$

where $\Theta(x)$ is the Heaviside function, and a Gaussian (G) pdf

$$\mathrm{pr}(\mathscr{C}_i|c) = \frac{1}{\sqrt{2\pi}sc} e^{-\frac{\mathscr{C}_i^2}{2s^2c^2}}, \tag{2.34}$$

where s is a scale factor. Inserting the priors for the width parameter (2.32) and the expansion coefficients $\mathscr{C}_i$ into the pdf for the normalized residual (2.30) leads to the LO expressions (see Appendix A for details)

$$p_1^{(\mathrm{hw})}(\Delta) = \frac{e^{\frac{R^2}{2}}}{4Q^2}\left[1 - \Phi\left(\frac{R}{\sqrt{2}}\left[1 + \frac{\log(\Delta/Q^2)}{R^2}\right]\right)\right], \tag{2.35}$$

where $\Phi(x)$ is the error function and

$$p_M^{(\mathrm{G})}(\Delta) = \frac{1}{2\pi Rqs}\int_0^\infty dx\, e^{-\frac{\log^2 x}{2R^2}} e^{-\frac{\Delta^2 x^2}{2s^2q^2}}, \tag{2.36}$$

where $q^2 \equiv \sum_{m=k+1}^{k+M} Q^{2m}$. The pdfs (2.35) and (2.36) were obtained employing the hard wall and Gaussian priors for the expansion coefficients, respectively. The superindices (hw) and (G) are employed to distinguish them. For the former, it was assumed that the largest contribution to the residual comes from the term proportional to Q^{k+1}, and the rest of the terms were neglected. This approximation will be referred to as next-term approximation.

Calculations at NLO allow one to test the proposed priors for the state-dependent expansion coefficient $\mathscr{C}_2$. First, a LO χ^2 fit is performed in order to set the energy scale ω. For this fit

$$\chi^2_{\mathrm{LO}} = \sum_d \frac{\left[E_{\mathrm{exp}}(d) - E_{\mathrm{LO}}(d)\right]^2}{\sigma^2_{\mathrm{exp}} + \sigma^2_{\mathrm{LO}}}. \tag{2.37}$$

Here, the data set consist of all the states up to the two-phonon level, E_{exp} and E_{LO} are the experimental and theoretical energies of such states, and σ_{LO} is the theoretical uncertainty at LO, set equal to the naive estimate $Q^2\omega$. The experimental uncertainty σ_{exp}, being much smaller than the theoretical uncertainty, is neglected during these fits. Next, the energies at NLO are written as

$$E_{\mathrm{NLO}} = \omega N + C_\omega N + C_N N^2 + C_v v(v+3) + C_I I(I+1), \tag{2.38}$$

where C_ω is a LEC. During the NLO fit

$$\chi^2_{\rm NLO} = \sum_d \frac{[E_{\rm exp}(d) - E_{\rm NLO}(d)]^2}{\sigma^2_{\rm exp} + \sigma^2_{\rm NLO}}, \tag{2.39}$$

where the LEC ω is fixed while the other LECs are allowed to vary. This is in agreement with the assumption for ω to have a sharp value. The theoretical uncertainty at NLO is set to $\sigma_{\rm NLO} = Q^3\omega$. The experimental uncertainty, are still small when compared to the theoretical uncertainty at this order, therefore it is neglected.

Let us define the expansion coefficient $\mathscr{C}_2$ by

$$\begin{aligned} \mathscr{C}_2 &\equiv \mathscr{C}_2(N, v, I) \\ &= \frac{C_\omega N + C_N N^2 + C_v v(v+3) + C_I I(I+1)}{Q^2\omega}. \end{aligned} \tag{2.40}$$

Its cumulative distribution, constructed from the $\mathscr{C}_2$ coefficient for states up to the two-phonon level within the ensemble of all nuclei near shell closures studied in this work, is shown in Figure 2.1. The small data set from which this cumu-

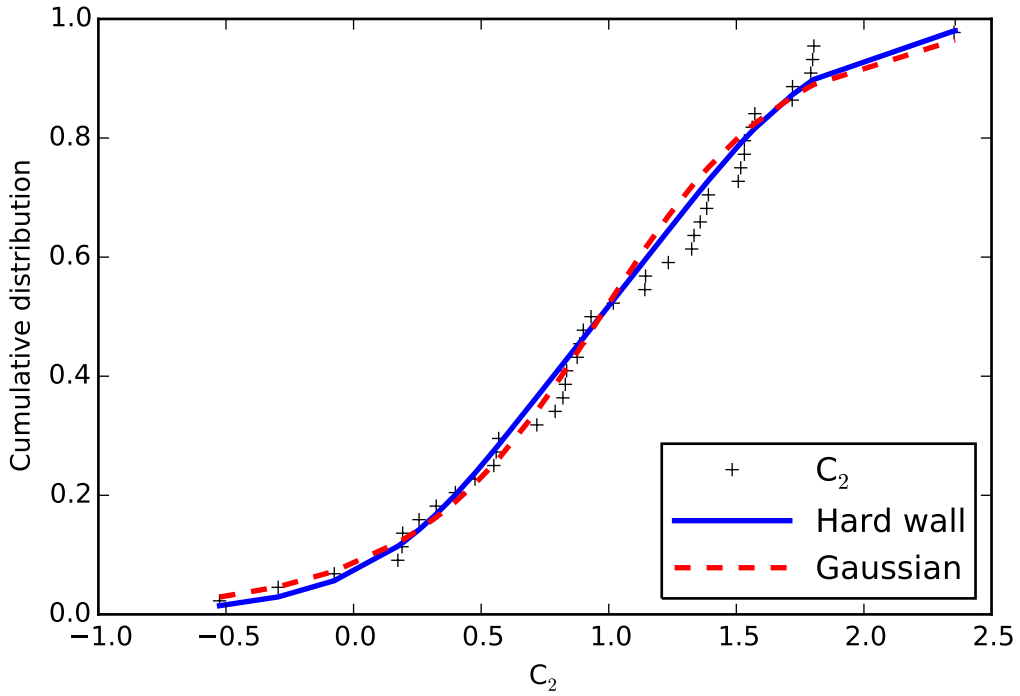

Figure 2.1: Cumulative distribution of the state-dependent C_2 coefficients for states up to the three-phonon level in the ensemble of all nuclei studied in this work. The cumulative distribution of the hard-wall and Gaussian priors is also shown for comparison.

lative distribution is constructed does not allow us to clearly identify which prior describes it better. Both the hard wall (2.33) and Gaussian (2.34) priors describe the cumulative distribution for $\mathscr{C}_2$, the later with a scale factor $s \approx 0.65$, after they are shifted by the mean value $\mu \approx 1$, that is, using $\mathrm{pr}(\mathscr{C}_2 - \mu)$. The cumulative distributions of the shifted priors are also shown in Figure 2.1. These cumulative distributions have a similar behavior close to the mean value μ. The difference between them is only appreciable at the tails of the distributions.

The knowledge acquired at NLO on the distribution of the $\mathscr{C}_2$ coefficient can be included when calculating the pdf for the normalized residual (2.30) at this order. The expressions

$$p_1^{(\mathrm{hw})}\left(\Delta|\mathscr{C}_2\right) = \frac{e^{\frac{3R^2}{2}}}{2Q^3} \frac{1 - \Phi\left(\frac{R}{\sqrt{2}}\left[2 + \frac{\log(\kappa)}{R^2}\right]\right)}{1 - \Phi\left(\frac{R}{\sqrt{2}}\left[1 + \frac{\log(|\mathscr{C}_2'|)}{R^2}\right]\right)}, \tag{2.41}$$

where $\kappa \equiv \max(|\mathscr{C}_2'|, \Delta/Q^3)$ and $\mathscr{C}_2' \equiv \mathscr{C}_2 - \mu$, and

$$p_M^{(\mathrm{G})}\left(\Delta|\mathscr{C}_2\right) = \frac{\int_0^\infty dx\, x e^{-\frac{\log^2 x}{2R^2}} e^{-\frac{\left(\mathscr{C}_2'^2 + \Delta^2/q^2\right)x^2}{2s^2}}}{\sqrt{2\pi} q s \int_0^\infty dx\, e^{-\frac{\log^2 x}{2R^2}} e^{-\frac{\mathscr{C}_2'^2 x^2}{2s^2}}}, \tag{2.42}$$

where $q^2 \equiv \sum_{m=k+1}^{k+M} Q^{2m}$, are obtained when the hard wall (2.33) and Gaussian (2.34) priors for the expansion coefficients $\mathscr{C}_i$ are inserted into Equation (2.30) (see Appendix A for details). Once again, the next-term approximation ($M = 1$) was employed to reach the analytic expression in Equation (2.41).

Let us discuss how to employ the normalized residual pdf to quantify the theoretical uncertainty. Given an interval $[a, b]$ in the domain of a pdf $p(x)$ for the variable x, its degree of belief (DOB) is defined as the integral of such pdf over the given interval

$$\mathrm{DOB}(a, b) = \int_a^b dx\, p(x). \tag{2.43}$$

Notice that due to pdfs being normalized, $\mathrm{DOB}(a, b) \leq 1$. Thus, the DOB of an interval represents the probability for the variable x to take a value within the interval $[a, b]$.

In the present case, it is possible to find a small interval in the domain of the pdf for the normalized residual around its centroid with a large DOB, or in other

words, an interval where such residual has a large probability to lie. Particularly, an interval within the value of the residual has a $X\%$ probability to lie is defined by

$$\mathrm{DOB}(-\delta,\delta) = \int_{-\delta}^{\delta} d\Delta\, p\left(\Delta|C_n\right) = X/100. \tag{2.44}$$

Intervals with different DOB can be employed to quantify the theoretical uncertainty as $\omega\delta$. For systems consistently described by the EFT, it is expected that $X\%$ of the experimental data lies within the theoretical uncertainty defined from the interval with a $X/100$ DOB.

In Section 2.2, experimental data are compared to calculations within the EFT employing a theoretical uncertainty $\omega\delta$, where δ defines an interval $[-\delta,\delta]$ for which the pdf for the normalized residual has $\mathrm{DOB}(-\delta,\delta) = 0.68$. For a Gaussian pdf, this interval is equivalent to a standard deviation σ. At LO, the pdfs in Equations (2.35) and (2.36) both yield values of $\delta = 0.07$ and $\delta = 0.29$ for the one- and two-phonon levels respectively. The values of δ employed to quantify the theoretical uncertainty at NLO for states up to the two-phonon level are listed in Table 2.1. There, columns labeled by hw and G show the values of δ obtained from the pdfs in Equations (2.41) and (2.42), respectively. The values obtained from the different priors are practically the same except for states with values for the expansion coefficient $\mathscr{C}_2$ far from the mean $\mu \approx 1$. These states sample the tails of the priors, where their behaviors differ the most. The values of the $\mathscr{C}_2$ coefficients are listed in Table 2.2 in Section 2.2.

Table 2.1: Values of δ in states up to the two-phonon level, calculated from the NLO pdfs for the normalized energy residual. Columns labeled by hw and G show the values of δ obtained from the pdfs in Equations (2.41) and (2.42) respectively.

	2_1^+		0_2^+		2_2^+		4_1^+	
Nucleus	hw	G	hw	G	hw	G	hw	G
^{62}Ni	0.02	0.02	0.29	0.22	0.21	0.20	0.20	0.20
^{98}Ru	0.02	0.02	0.18	0.19	0.18	0.18	0.18	0.18
^{100}Ru	0.04	0.03	0.18	0.18	0.30	0.22	0.21	0.20
^{106}Pd	0.03	0.02	0.18	0.18	0.18	0.18	0.21	0.20
^{108}Pd	0.02	0.02	0.18	0.19	0.18	0.18	0.18	0.19
^{110}Cd	0.02	0.02	0.18	0.18	0.18	0.18	0.19	0.19
^{112}Cd	0.02	0.02	0.18	0.18	0.18	0.18	0.18	0.19
^{114}Cd	0.02	0.02	0.18	0.18	0.18	0.18	0.18	0.19
^{118}Te	0.02	0.02	0.34	0.23	0.21	0.20	0.19	0.19
^{120}Te	0.02	0.02	0.19	0.19	0.18	0.18	0.18	0.19
^{122}Te	0.03	0.03	0.18	0.18	0.18	0.19	0.21	0.20

2.2 Comparison to spectra

In order to test the EFT, we compare the low-energy spectra of some nuclei near shell closures against LO and NLO calculations. The considered nuclei fulfill the following criteria.

(i) All the states with the spins of the two-phonon triplet lie at energies around two times $E(2_1^+)$. This implies $R_{4/2} \approx 2$.

(ii) The energy spectra exhibit states with some of the spins of the three-phonon quintuplet at energies around three times $E(2_1^+)$.

The LECs required for the description of the energy spectra of the nuclei near shell closures studied in this work at LO and NLO are listed in Table 2.2. They were obtained from χ^2 fits at LO and NLO with a breakdown scale set to $\Lambda = 3\omega$, based on the appearance of states that cannot be identified as quadrupole excitations. The natural size of the state-dependent coefficient $\mathscr{C}_2$ for all states below the breakdown scale justify such choice for Λ. The choice $\Lambda = 4$ leads to coefficients of unnatural size, and theoretical uncertainties for the two-phonon states that increase with order, against the systematic improvement expected below the breakdown scale.

The theoretical uncertainty is quantified from 68% DOB intervals. In order to test the statistical character of the uncertainty, the data set consisting of the energies of the one- and two-phonon states in the ensemble of the nuclei studied in

Table 2.2: Values of the LO and NLO expansion coefficients for energies for the ensemble of nuclei studied in this work. The LECs necessary for their calculation were obtained from χ^2 fits at LO and NLO respectively, with a breakdown scale set to $\Lambda = 3\omega$.

Nucleus	ω [keV]	$\mathscr{C}_2(2_1^+)$	$\mathscr{C}_2(0_2^+)$	$\mathscr{C}_2(2_2^+)$	$\mathscr{C}_2(4_1^+)$
^{62}Ni	1147.9	0.55	-0.29	0.19	0.26
^{98}Ru	668.1	1.02	0.57	0.88	0.83
^{100}Ru	573.9	2.35	1.39	2.36	1.79
^{106}Pd	541.8	1.80	1.38	1.36	1.80
^{108}Pd	464.5	1.14	1.53	0.90	1.51
^{110}Cd	696.7	1.57	1.32	1.33	1.56
^{112}Cd	635.2	1.72	0.82	1.14	1.52
^{114}Cd	578.3	1.72	0.93	1.23	1.53
^{118}Te	582.9	0.83	-0.52	0.19	0.40
^{120}Te	567.8	0.79	0.32	0.71	0.56
^{122}Te	593.5	-0.08	0.88	0.48	0.17

this work was compared against calculations within the EFT. The results are shown in Figure 2.2. There, experimental data, LO and NLO calculations are shown as black lines, red crosses and blue diamonds, respectively. To produce these results, the energies of the states for a given nucleus were normalized to the correspondent ω. Then, χ^2 fits at LO and NLO were performed. The theoretical uncertainties at LO and NLO, displayed as red and blue shaded areas, respectively, were obtained from 68% DOB intervals for the pdfs (2.36) and (2.42). In this case, 81.8% of the experimental data lie within the theoretical uncertainty. This percentage is consistent with 68% within the uncertainty associated with the sample size $\sigma = \sqrt{1/44} = 15.1\%$. The rest of the figures in this Section, where the spectra of nuclei is compared against the EFT, display a theoretical uncertainty obtained from 68% DOB intervals.

The low-lying spectrum of ^{62}Ni, shown in Figure 2.3, exhibits states that can be characterized as multiphonon excitations up to the three-phonon level, making this nucleus a good candidate for low-energy vibrational behavior. States that cannot be identified as quadrupole excitations appear above four of the three-phonon candidates.

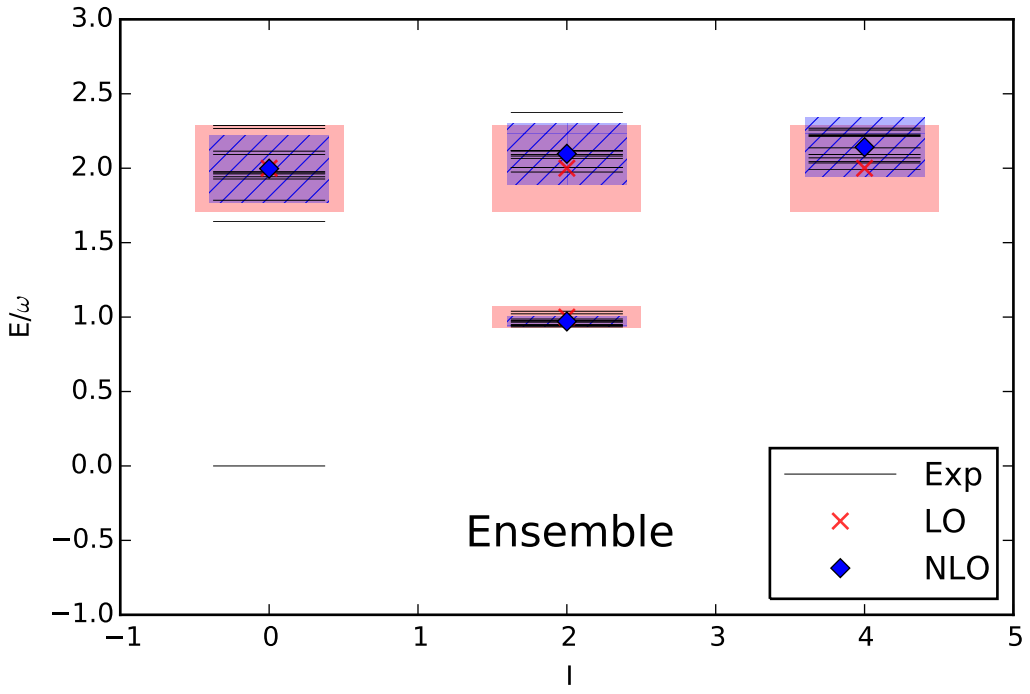

Figure 2.2: Normalized energies of the one- and two-phonon states in the ensemble of the nuclei studied in this work. Experimental energies are shown as thick black lines. Theoretical uncertainty is shown as error bars.

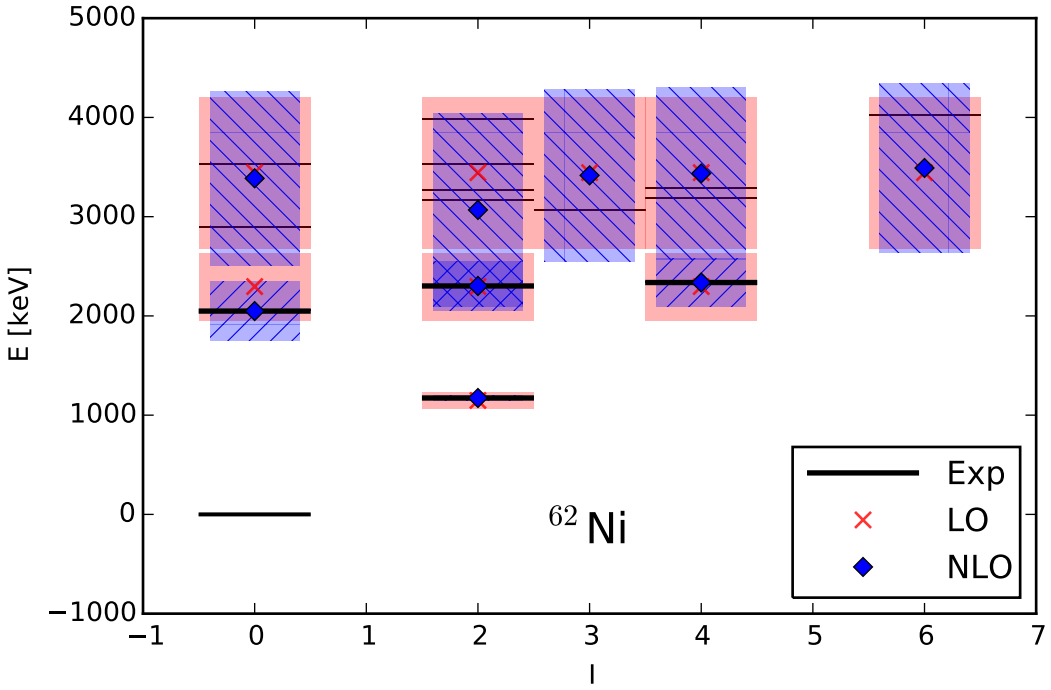

Figure 2.3: Partial energy spectrum of ^{62}Ni up to the three-phonon level. Experimental data are compared against LO and NLO calculations of the EFT. States up to and above the two-phonon level are shown as thick and thin black lines respectively. Theoretical uncertainty is shown as error bars.

The experimental data were taken from Ref. [76]. The NLO theoretical uncertainty in the energy calculated for the 0_2^+ state is slightly smaller that LO one. In Figure 2.3, the states taken into account during the χ^2 fits are displayed as thick black lines, while other states with definite spin assignments are displayed as thin lines. For this nucleus, the density of states above the two-phonon level is larger than shown in Figure 2.3.

The breakdown at the three-phonon level is in agreement with the study on this nucleus presented in Ref. [69], and other nickel isotopes [77, 78]. Shell model calculations with a ^{40}Ca core were required to simultaneously describe the energies and electromagnetic properties of states up to the three-phonon level. These results suggest that intruder configurations due to the promotion of protons or neutrons across the $Z = 28$ or $N = 28$ shell gaps are relevant for the appropriate description of the spectra and $E2$ transitions in these nuclei.

The results for ruthenium isotopes near the $N = 50$ shell closure are shown in Figure 2.4. A comparison between the energy spectra of ^{98}Ru and ^{100}Ru and calculations within the EFT are shown in the top and bottom of the Figure, respectively.

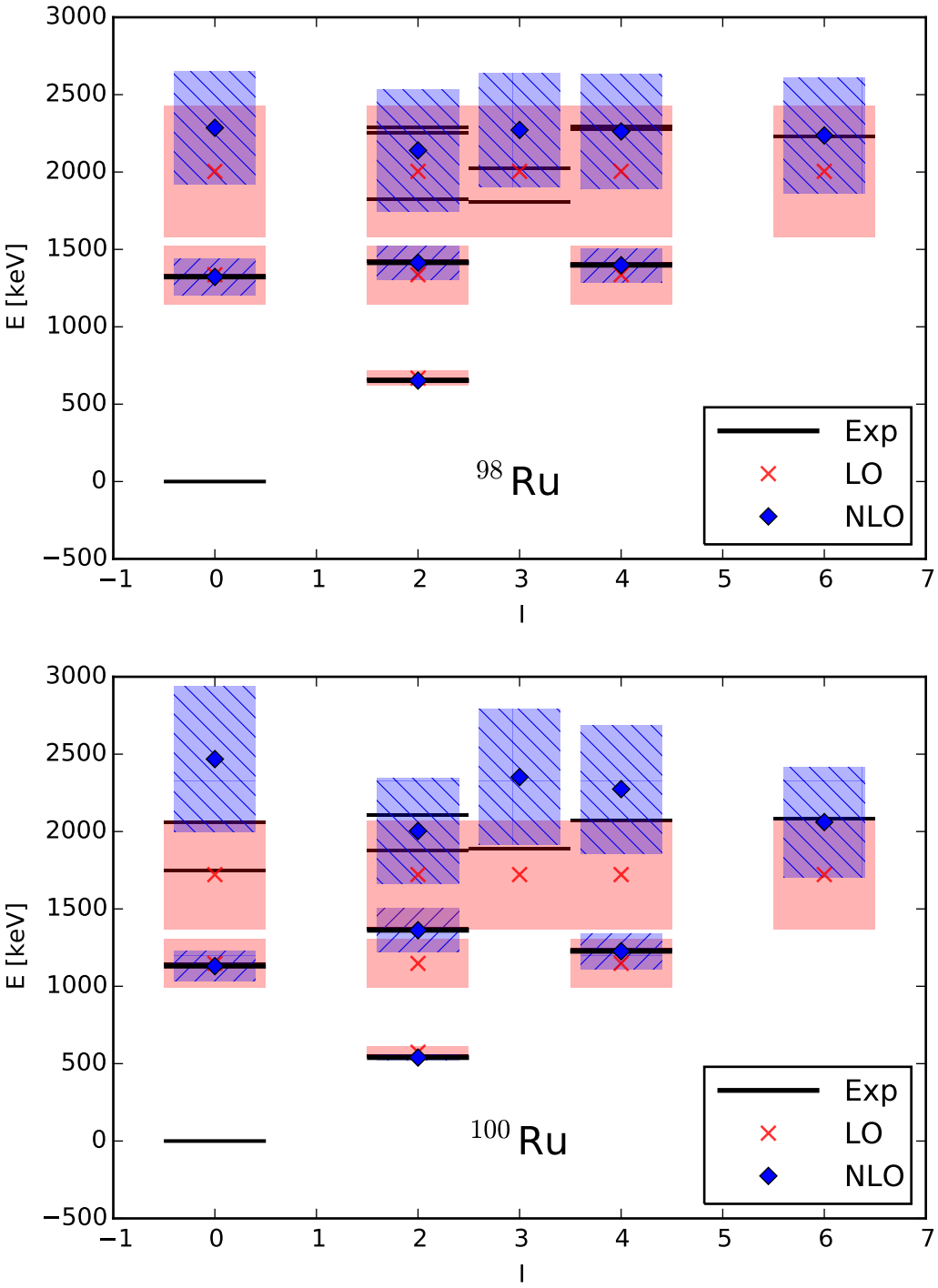

Figure 2.4: Partial energy spectrum of ^{98}Ru (top) and ^{100}Ru (bottom) up to the three-phonon level. Experimental data are compared against LO and NLO calculations of the EFT. States up to and above the two-phonon level are shown as thick and thin black lines respectively. Theoretical uncertainty is shown as error bars.

The low-energy spectra of these isotopes exhibit quadrupole excitations, with several states that cannot be identified as such above the two-phonon level. From this chain, ^{98}Ru is the first isotope expected to exhibit collective behavior based on its ratio of energies $R_{4/2} > 2$. Experimental energies were taken from Ref. [79]. For ^{100}Ru, experimental data was taken from Ref. [80].

The breakdown of vibrational behavior in ruthenium isotopes may be due to collective mixed symmetry modes that distinguish protons and neutrons. Previous work characterized the 2_3^+ and 3_1^+ states in these systems as mixed symmetry states [81, 82, 83]. The mix between multiphonon and mixed symmetry states makes it difficult to characterize the states above the two-phonon level. Shell model calculations with neutrons promoted across the $N = 50$ shell gap reveal the importance of single particle motion in this isotopic chain [84, 85]. It was suggested that nuclei in this isotopic chain undergo a transition from spherical to triaxial shapes, based on the behavior of the ratio $R_{4/2}$ with increasing neutron number [86]. Larger deviations from the harmonic behavior in ^{100}Ru would imply larger deviations from the spherical shape than those assumed for ^{98}Ru.

The energy spectra of ^{106}Pd and ^{108}Pd are compared against LO and NLO calculations in the top and bottom of Figure 2.5, respectively. Experimental data for ^{106}Pd and ^{108}Pd were taken from Refs. [87, 88], respectively. The spectra suggest low-energy vibrational motion in these nuclei.

Mixed symmetry excitations seem to be relevant modes at low-energies in the palladium isotopes too, causing large deviations from the harmonic vibrational behavior at the two-phonon level. Studies similar to those on ruthenium isotopes characterize the 2_3^+ and 3_1^+ states as mixed symmetry states in this isotopic chain [89, 90]. Single particle motion is also relevant in ^{108}Pd [91]. The studied palladium isotopes posses large static quadrupole moments even for states below the three-phonon level [56], suggesting that deviations from the spherical shape in these systems are large.

The comparison between the energy spectra, LO and NLO calculations for ^{110}Cd and ^{112}Cd is shown in the top and bottom of Figure 2.6 respectively, while the same comparison for ^{114}Cd is shown in Figure 2.7. Experimental data for the $A = 110, 112, 114$ isotopes were taken from Refs. [92, 93, 94], respectively. The cadmium isotopes have been considered textbook cases of low-energy vibrational behavior based on their energy spectra [24, 95, 25], despite exhibiting states with spins $I = 0, 2$ around the two-phonon level that cannot be identified as quadrupole

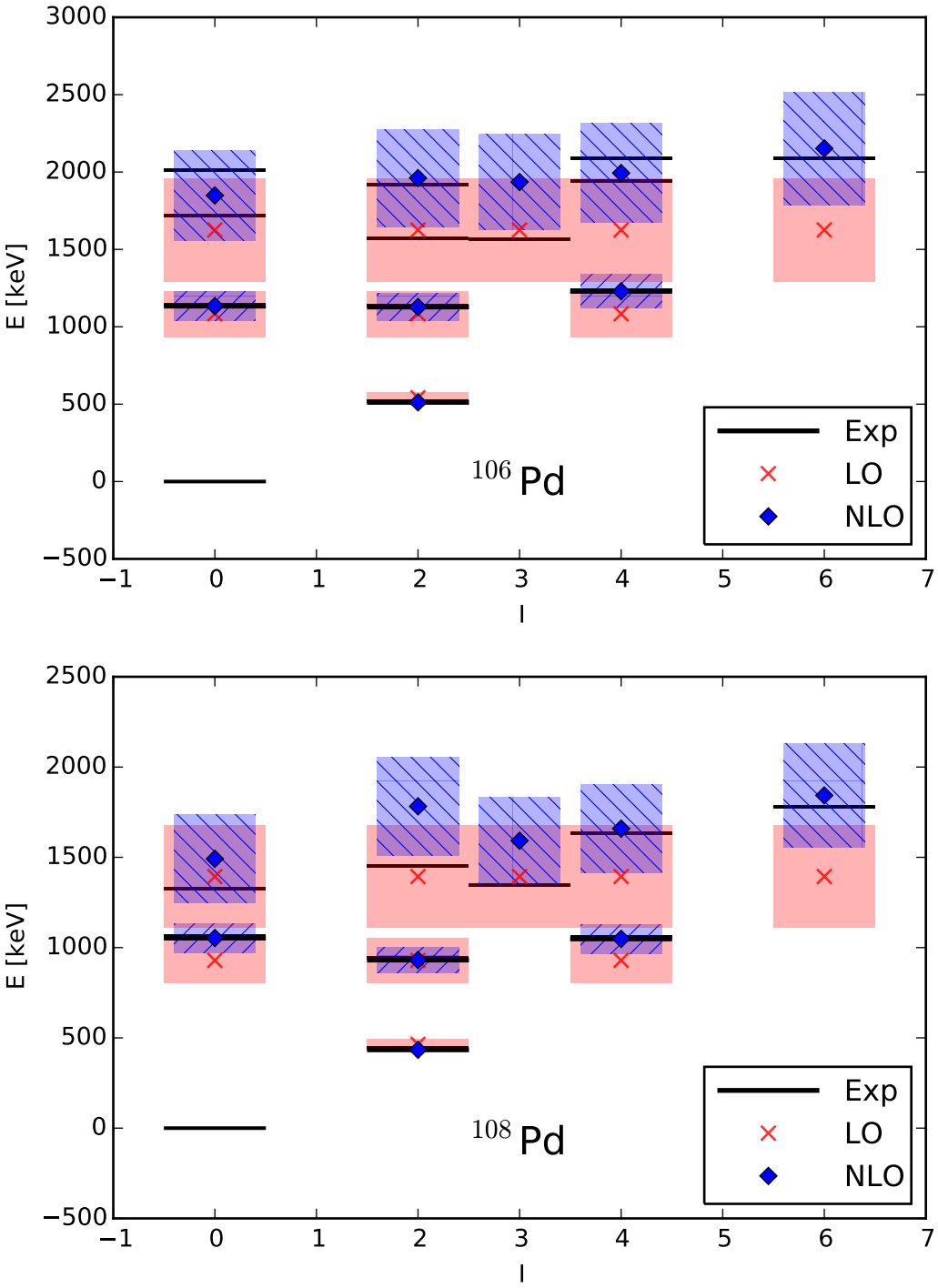

Figure 2.5: Partial energy spectrum of ^{106}Pd (top) and ^{108}Pd (bottom) up to the three-phonon level. Experimental data are compared to LO and NLO calculations of the EFT. States up to and above the two-phonon level are shown as thick and thin black lines respectively. Theoretical uncertainty is shown as error bars.

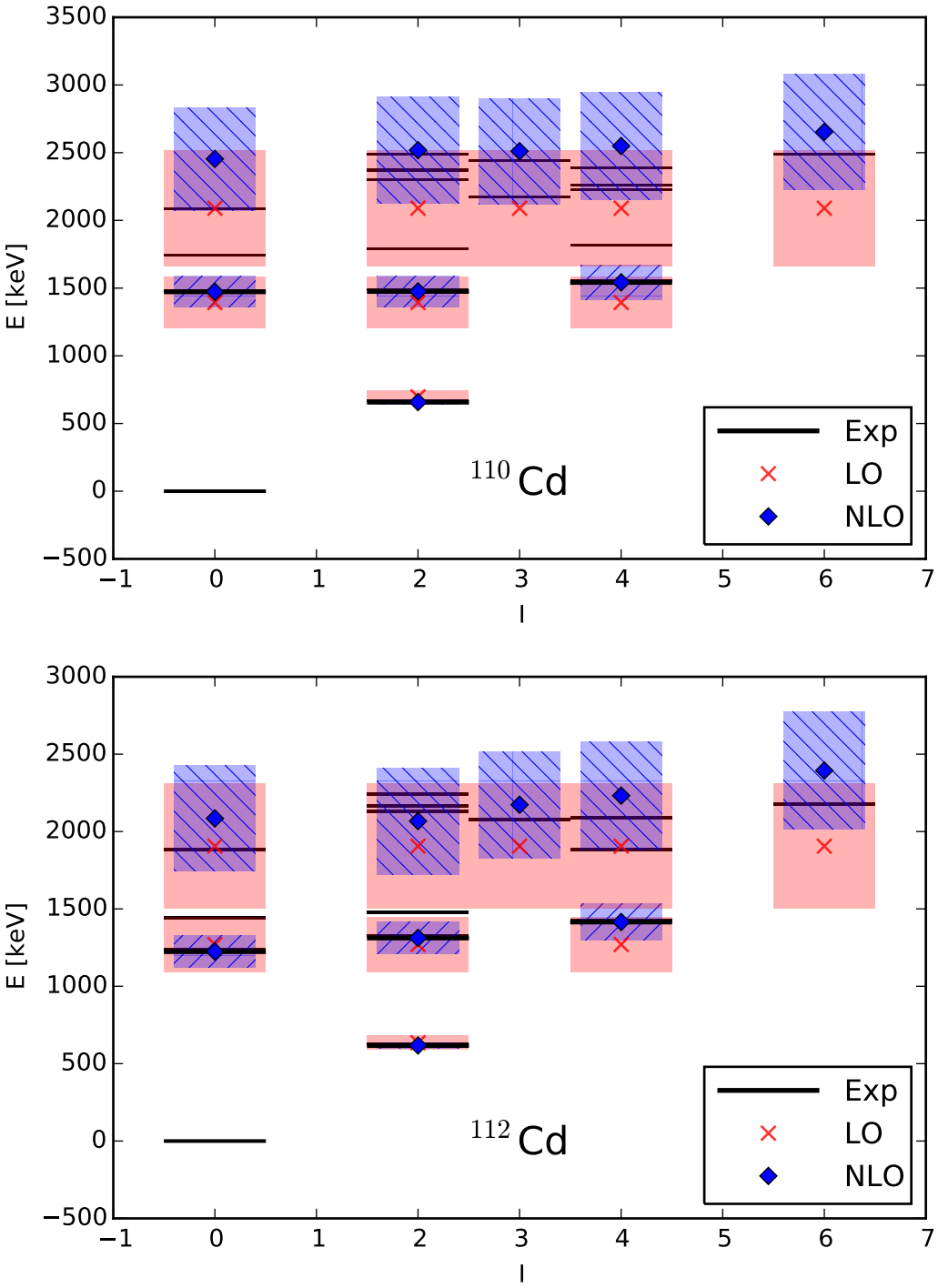

Figure 2.6: Partial energy spectrum of ^{110}Cd (top) and ^{112}Cd (bottom) up to the three-phonon level. Experimental data are compared against LO and NLO calculations of the EFT. States up to and above the two-phonon level are shown as thick and thin black lines respectively. Theoretical uncertainty is shown as error bars.

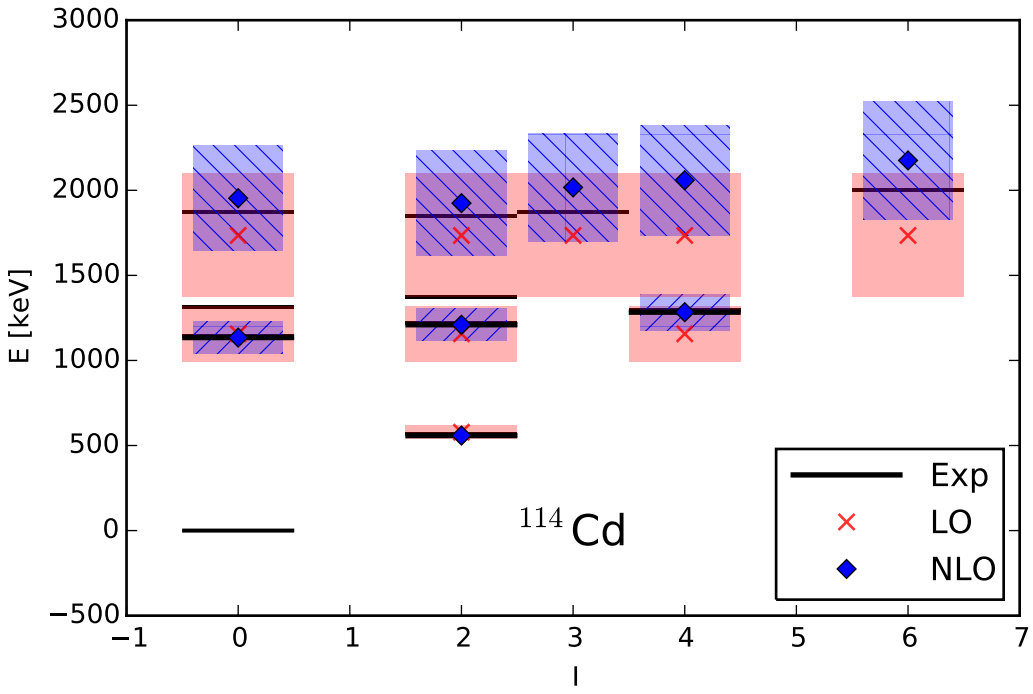

Figure 2.7: Partial energy spectrum of ^{114}Cd up to the three-phonon level. Experimental data are compared against LO and NLO calculations of the EFT. States up to and above the two-phonon level are shown as thick and thin black lines respectively. Theoretical uncertainty is shown as error bars.

excitations. For the isotopes studied in this work, the 0_2^+, 2_2^+ and 4_1^+ were used as two-phonon excitations during the χ^2 fits, in disagreement with previous studies [66, 96, 70, 52, 97], where some of these states are characterized as intruder states. This identification is made based on the assumption that modes besides quadrupole excitations require more energy to be excited. Also, $B(E2)$ values for decays from the chosen states seems to be in better agreement with the EFT expectations than those from other states, as will be discussed later.

The intruder states at the two-phonon level are due to protons promoted across the $Z = 50$ shell gap [98, 99]. The alignment of both valence nucleons and promoted protons breaks the spherical symmetry assumed by the EFT and give rise to noncollective deformed states, that compete energetically with the collective excitations. Studies on cadmium isotopes [64, 66, 100, 101, 96, 70] in which a strong mixing between multiphonon states and other excitations is invoked to explain the electromagnetic properties of multiphonon candidates, is able to describe isotopes near the $Z = 50$ shell closure. These studies set the breakdown of vibrational behavior at the two- or three-phonon level depending on the isotope, and suggest a quasi-rotational character for the low-lying excitations, based on the large

quadrupole moments of some yrast states [49, 52].

The energy spectrum of ^{118}Te is compared against LO and NLO calculations in Figure 2.8, while the same comparison for ^{120}Te and ^{122}Te is shown in the top and bottom of Figure 2.9, respectively. Experimental data for the $A = 118, 120, 122$ isotopes were taken from Refs. [102, 46, 103], respectively. The energy spectra of these isotopes are very similar, with states that can be identified as multiphonon excitations up to the three-phonon level, and states that cannot be identified as quadrupole excitations appearing at the three-phonon level. From these isotopes, the best candidate is ^{120}Te with states that cannot be identified with quadrupole excitations slightly above the states identified as the three-phonon quintuplet. For ^{118}Te and ^{122}Te, the 2_4^+ and 0_4^+ are the first nonvibrational states, respectively. They both lie above four of the states identified as three-phonon excitations. Thus, from energy considerations, these nuclei are the best representatives of quadrupole vibrational excitation.

The breakdown of the harmonic quadrupole vibrator behavior is a consequence of competing single-particle motion, known to exist in tellurium isotopes [104, 105,

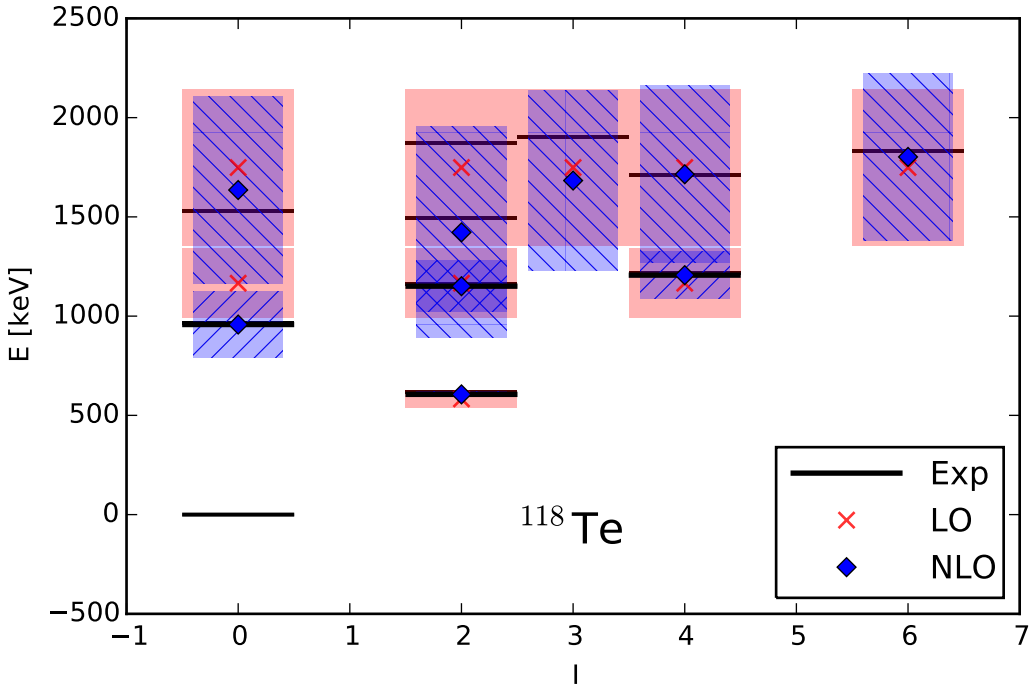

Figure 2.8: Partial energy spectrum of ^{118}Te up to the three-phonon level. Experimental data are compared against LO and NLO calculations of the EFT. States up to and above the two-phonon level are shown as thick and thin black lines respectively. Theoretical uncertainty is shown as error bars.

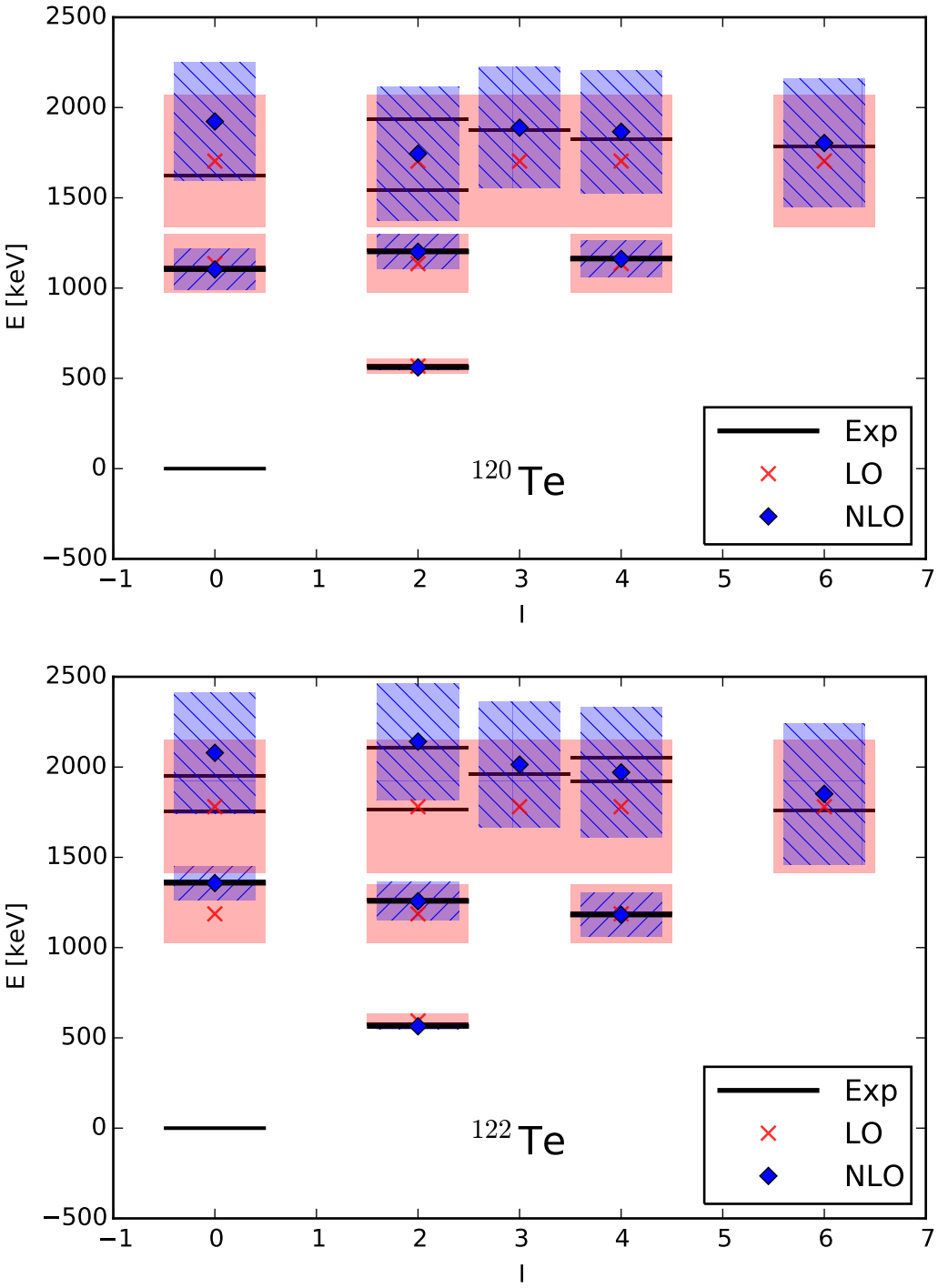

Figure 2.9: Partial energy spectrum of ^{120}Te (top) and ^{122}Te (bottom) up to the three-phonon level. Experimental data are compared against LO and NLO calculations of the EFT. States up to and above the two-phonon level are shown as thick and thin black lines respectively. Theoretical uncertainty is shown as error bars.

106, 107, 108, 109], and signaled in ^{122}Te by the unusual energy ratios $E(4_1^+)/E(2_1^+) < 2$ and $E(6_1^+)/E(4_1^+) < 1.5$ [110]. Intruder configurations due to protons promoted across the $Z = 50$ shell gap breaks the spherical symmetry and give rise to noncollective deformed states that compete energetically with the quadrupole excitations. In particular, the 6_1^+ state has been interpreted both as a multiphonon state and in terms of valence protons configurations coupled to a tin core.

2.3 Electromagnetic coupling

In this section the EFT for electric quadrupole transitions developed in Ref. [30] is described in detail. At LO, the transition operator obtained after gauging the Hamiltonian is equivalent to the electric quadrupole operator proposed by Bohr [23, 24, 25], and the $E2$ reduced transition probabilities for decays from multiphonon states are identical to those predicted by the harmonic vibrator submodel of the Bohr collective model. Higher-order corrections to this operator provide a consistent description of large static quadrupole moments and transitions between states with the same phonon number. The theoretical uncertainty in LO $B(E2)$ values for decays from states below the breakdown scale is quantified employing Bayesian statistics. This uncertainty allows us to meaningfully compare experimental data on $E2$ transitions and calculations within the EFT.

2.3.1 Minimal coupling and the leading order transition operator

In order to couple the effective DOF to an electromagnetic field, the vector potential $\mathbf{A}$ is written as an expansion in terms of spherical harmonics

$$\mathbf{A} = \sum_{IMl} A_{IMl} j_l(kr) \sum_{mn} C^{IM}_{lm1n} Y_{lm}(\theta, \phi) \mathbf{e}_n, \tag{2.45}$$

where $j_l(kr)$ are spherical Bessel functions, $\mathbf{e}_n$ with $n = \pm 1, 0$ are spherical basis vectors, and the expansion coefficients A_{IMl} form a spherical tensor of rank I for a fixed l. Thus, the quadrupole DOF of the EFT couple to the tensors of rank two defined by this expansion. In the long wavelength limit $kr \ll 1$, the spherical Bessel functions are such that $j_l(kr) \propto (kr)^l$. Thus, at LO in kR the coupling of the quadrupole DOF to an electromagnetic field is achieved via the gauging

$$\pi_\mu \to \pi_\mu - q A_{2\mu 1}. \tag{2.46}$$

Let us use a vector potential of the form

$$\begin{aligned}\mathbf{A} =& -iAe^{ikx(\theta,\phi)}\mathbf{e}_z \\ \approx& -iA\left[1+ikx(\theta,\phi)\right]\mathbf{e}_z \\ \approx& -iA\Big\{1+ikR_0\sqrt{\frac{2\pi}{3}}\left[Y_{1-1}(\theta,\phi)-Y_{11}(\theta,\phi)\right]\Big\}.\end{aligned} \tag{2.47}$$

Here the value of $\mathbf{A}$ at R_0 has been employed. If this expression is compared to the expansion (2.45) we find

$$A_{2\pm11} = \mp A\sqrt{\frac{4\pi}{3}}, \qquad A_{2\pm21} = 0 = A_{201}. \tag{2.48}$$

This result is equivalent to that for the toy model presented in Appendix B.

The gauging of the LO Hamiltonian (2.16) minimally couples the quadrupole DOF to the electromagnetic field yielding the LO EFT for nuclear vibrations coupled to an electromagnetic field. The Hamiltonian is of the form $\hat{H}_{\rm LO}+\hat{H}^{(\mathbf{A})}_{\rm LO}$, where

$$\hat{H}^{(\mathbf{A})}_{\rm LO} = -\frac{q}{B}\sum_{\mu}(-1)^{\mu}A_{2-\mu1}\pi_{\mu}, \tag{2.49}$$

and terms of order $\mathcal{O}(q^2A^2)$ have been neglected since they represent suppressed two-photon processes. From here, the transition operator is

$$\hat{\mathscr{M}}_{\rm LO}(E2)_{\mu} = \sqrt{2}Q_0\ell\pi_{\mu}, \tag{2.50}$$

where Q_0 is a LEC with the dimensions of a quadrupole moment [eb] that must be fit to data. At this order the transition operator $\hat{\mathscr{M}}_{\rm LO}(E2)$ is equivalent to the $E2$ operator proposed by Bohr in his collective model [23, 24, 25]. Consequently, transitions between a initial state $|i\rangle$ and a final state $|f\rangle$ are only allowed if $\Delta N=\pm1$ and $|\Delta I|\leq 2$. At this order, the $B(E2)$ values for transitions between multiphonon states calculated within the EFT are equal to those predicted by the harmonic vibrator submodel of the Bohr collective model (see, e.g. Refs. [24, 25])

$$\begin{aligned}B(E2,2^+_1\to0^+_1) =& Q_0^2, \\ B(E2,0^+_2\to2^+_1) =& 2Q_0^2, \\ B(E2,2^+_2\to2^+_1) =& 2Q_0^2, \\ B(E2,4^+_1\to2^+_1) =& 2Q_0^2.\end{aligned} \tag{2.51}$$

2.3.2 Nonminimal couplings and the electric quadrupole operator

Nonminimal coupling arise because the DOF describe composite objects. These terms must be gauge-invariant, and consistent with the symmetries of the system. They account for deviations from the LO electromagnetic behavior.

In the Coulomb gauge $\nabla\cdot\mathbf{A}=0$, the electric field is given by $\mathbf{E}=-\partial_t\mathbf{A}=ik\mathbf{A}$. This field can be coupled to the quadrupole DOF as follows

$$\hat{H}^{(\mathbf{E})}=\sum_{\mu}(-1)^{\mu}E_{2-\mu 1}\left[q_0\tilde{\alpha}_{\mu}+q_1(\tilde{\alpha}\otimes\tilde{\alpha})^{(2)}_{\mu}+\sum_{L}q_{2L}\left(\tilde{\alpha}\otimes(\tilde{\alpha}\otimes\tilde{\alpha})^{(L)}\right)^2_{\mu}+\ldots\right], \tag{2.52}$$

where $E_{2M1}=ikA_{2M1}$ and $L=0,2,4$. The first term in this expansion is equivalent to the minimal coupling term that give raise to the LO transition operator. Subsequent terms correct the LO interaction between the system and the electric field. From the coupling (2.52) the most general $E2$ operator is defined as

$$\begin{aligned}\hat{\mathscr{M}}(E2)_{\mu}\equiv&\frac{\sqrt{2}}{\ell}Q_0\tilde{\alpha}_{\mu}+\frac{2}{\ell^2}Q_1(\tilde{\alpha}\otimes\tilde{\alpha})^{(2)}_{\mu}+\frac{2^{3/2}}{\ell^3}\sum_{L}Q_{2L}\left(\tilde{\alpha}\otimes(\tilde{\alpha}\otimes\tilde{\alpha})^{(L)}\right)^2_{\mu}+\ldots\\ =&Q_0\left(d^{\dagger}_{\mu}+\tilde{d}_{\mu}\right)+Q_1\left[\left(d^{\dagger}\otimes d^{\dagger}\right)^{(2)}_{\mu}+\left(\tilde{d}\otimes\tilde{d}\right)^{(2)}_{\mu}+2\left(d^{\dagger}\otimes\tilde{d}\right)^{(2)}_{\mu}\right]+\ldots.\end{aligned} \tag{2.53}$$

Here, the factors $(\sqrt{2}/\ell)^n$ with n being the number of quadrupole tensors in a term, have been introduced for convenience.

At the breakdown scale Λ, every term of the $E2$ operator (2.53) must be of the same size as the LO contribution. Thus, from the scale of the quadrupole DOF at breakdown (2.18)

$$\begin{aligned}Q_0\sqrt{\frac{\Lambda}{\omega}}\sim Q_1\frac{\Lambda}{\omega}\implies Q_1\sim Q_0\sqrt{\frac{\omega}{\Lambda}},\\ Q_0\sqrt{\frac{\Lambda}{\omega}}\sim Q_{2L}\left(\frac{\Lambda}{\omega}\right)^{3/2}\implies Q_{2L}\sim Q_0\frac{\omega}{\Lambda},\end{aligned} \tag{2.54}$$

and so on.

The first and third terms of the $E2$ operator (2.53) couple states with $\Delta N=\pm 1$, and can be identified as the LO transition operator and its NLO correction, respectively. The second term has diagonal matrix elements, and can be employed to calculate the LO static quadrupole moments. The static quadrupole moment

of a state I^π is given by

$$Q(I^\pi) \equiv \langle I^\pi || \hat{\mathscr{M}}(E2) || I^\pi \rangle, \tag{2.55}$$

where the $E2$ reduced matrix element between the states $|i\rangle$ and $|f\rangle$ can be calculated employing the Wigner-Eckart theorem

$$\langle I_f || \hat{\mathscr{M}}(E2) || I_i \rangle = \frac{\sqrt{2I_f+1}}{C^{I_f M_f}_{I_i M_i 2\mu}} \langle \beta I_f M_f | \hat{\mathscr{M}}(E2)_\mu | \alpha I_i M_i \rangle. \tag{2.56}$$

Here the subindices i and f are used to differentiate the spins and projections of the initial and final states, respectively, and α and β are employed to denote all the quantum numbers that are not required to calculate a reduced matrix element. The static quadrupole moment of the first excited state is

$$\begin{aligned} \langle 2_1^+ || \hat{\mathscr{M}}(E2) || 2_1^+ \rangle &= \frac{\sqrt{5}}{C^{20}_{2M20}} \langle \beta 2M | 2Q_1 \left(d^\dagger \otimes \tilde{d} \right)^{(2)}_0 | \alpha 2M \rangle \\ &= \frac{2\sqrt{5}}{C^{2M}_{2M20}} Q_1 \langle 0 | \sum_{mn} (-1)^n C^{20}_{2m2n} d_M d^\dagger_m d_{-n} d^\dagger_M | 0 \rangle \\ &= 2\sqrt{5} Q_1. \end{aligned} \tag{2.57}$$

In order to reach this expression, the commutation relations of the quadrupole operators (2.1) and the symmetry properties of the Clebsch-Gordan coefficients [50] have been employed. Similarly, for the 2_2^+ and 4_1^+ states one finds

$$\langle 2_2^+ || \hat{\mathscr{M}}(E2) || 2_2^+ \rangle = -\frac{6\sqrt{5}}{7} Q_1, \qquad \langle 4_1^+ || \hat{\mathscr{M}}(E2) || 4_1^+ \rangle = \frac{6\sqrt{110}}{7} Q_1. \tag{2.58}$$

Thus, within the EFT the static quadrupole moments are non vanishing and scale as $Q_1 \sim Q_0 \sqrt{\omega/\Lambda}$. The low breakdown scale makes them sizable. This prediction strongly differs from that by the harmonic vibrator submodel.

The $E2$ operator (2.53) also couples states with the same number of phonons. The reduced matrix elements for the transitions $0_2^+ \to 2_2^+$ and $4_1^+ \to 2_2^+$ between two-phonon states are

$$\langle 2_2^+ || \hat{\mathscr{M}}(E2) || 0_2^+ \rangle = 4Q_1, \qquad \langle 2_2^+ || \hat{\mathscr{M}}(E2) || 4_1^+ \rangle = \frac{24}{7} Q_1. \tag{2.59}$$

Transitions between states with the same phonon number are forbidden within the harmonic vibrator submodel. Within the EFT, these transitions are completely determined at LO by the LEC Q_1.

2.3.3 Reduced matrix elements uncertainty quantification

The theoretical uncertainty in the $B(E2)$ values for LO transitions arises from omitted corrections to the transition operator and the LO states. In order to write an effective expansion for the reduced matrix elements of the LO transitions, it is necessary to estimate the sizes of both corrections. Nonminimal coupling terms inducing $E2$ transitions between the LO states are of the form $\Delta\hat{\mathscr{M}}(E2) \propto \hat{\mathscr{M}}_{\mathrm{LO}}(E2)(d^\dagger\tilde{d})^n$, with $n \geq 1$. They correct the reduced matrix elements for $E2$ transitions with contributions naively expected to scale as $Q^n Q_0$, so that

$$\langle f||\Delta\hat{\mathscr{M}}(E2)||i\rangle \sim Q_0 Q^n, \tag{2.60}$$

As mentioned before, the states are also corrected order by order. The largest correction to the reduced matrix elements of $E2$ transitions comes from a correction to the Hamiltonian with four quadrupole operators coupling states for which $\Delta N = \pm 2$. The correction to a state due to this term scales as Q^2, implying the correction to the reduced matrix elements of $E2$ transitions due to this correction scales as

$$\langle f||\hat{\mathscr{M}}(E2)||\Delta i\rangle \sim \langle \Delta f||\hat{\mathscr{M}}(E2)||i\rangle \sim Q_0 Q^2, \tag{2.61}$$

To understand this, note that the correction to an N-phonon state due to the discussed term is a linear combination of states with $N \pm 2$ phonons, implying the matrix elements of the LO transition operator between a state with $N \pm 1$ phonons and the mentioned correction do not vanish.

From this discussion, the following effective expansion in powers of Q for the reduced matrix elements for LO decays arises

$$\langle f||\hat{\mathscr{M}}(E2)||i\rangle = \langle f||\hat{\mathscr{M}}(E2)||i\rangle_{\mathrm{LO}} \left(1 + \sum_i \mathscr{D}_i Q^i\right), \tag{2.62}$$

with $i \geq 1$. The expansion coefficients $\mathscr{D}_i$ are expected to be of order one. The $B(E2)$ values can be calculated from the reduced matrix elements via

$$B(E2, i \to f) = \frac{1}{2I_i + 1}\left|\langle f||\hat{\mathscr{M}}(E2)||i\rangle\right|^2. \tag{2.63}$$

This definition leads to an effective expansion for the $B(E2)$ values in terms of the expansion (2.62). The later defines a normalized residual for the $B(E2)$ values, analog to the residual for the energies defined in Section 2.1.3. Bayesian statistics leads to the pdf for this residual. The interval $[-\delta, \delta]$ for which this pdf has

$\mathrm{DOB}(-\delta, \delta) = 0.68$, can be employed to quantify the theoretical uncertainty in the calculated $B(E2)$ values as $Q_0\delta$.

Similar expansions are found for the reduced matrix elements whose leading order contribution is proportional to Q_1. The contribution from the first omitted term in these expansions is expected to scale as $Q_0 Q^{3/2}$. The theoretical uncertainty at LO for these matrix elements can be quantified similarly to the theoretical uncertainty for the $B(E2)$ values for the LO decays.

2.4 Comparison to electric quadrupole properties

In this section the EFT for nuclear vibrations coupled to an electromagnetic field is tested. For this purpose, data on $E2$ reduced transition probabilities and static quadrupole moments are compared to LO calculations. The EFT is consistent with experimental data on $E2$ reduced transitions probabilities for the LO decays. The static quadrupole moments of the 2_1^+ state scale as expected. For the palladium isotopes studied in this work and ^{114}Cd, the static quadrupole moments of the 2_1^+, 2_2^+ and 4_1^+ states are used to fix the LEC Q_1. Reduced matrix elements for transitions between two-phonon states are predictions. Experimental data for these transitions is in agreement with the EFT.

2.4.1 Electric quadrupole transitions

In order to test predictions within the EFT on $E2$ transitions, data on $E2$ reduced transition probabilities for decays from states up to the two-phonon level were compared against LO calculations. Experimental data were mostly taken from the Nuclear Data Sheets for the studied nuclei [76, 79, 80, 87, 88, 92, 93, 94, 102, 46, 103]. For ^{62}Ni, data were complemented with that from Ref. [69]. For ^{98}Ru, conflicting $B(E2)$ values for the decay from the 4_1^+ state have been reported in Refs. [84, 86, 111, 63]. Data from Ref. [63], which established a ratio $B_{4/2} = B(E2, 4_1^+ \to 2_1^+)/B(E2, 2_1^+ \to 0_1^+) = 1.86(16)$ in agreement with expectations for collective motion, were used instead of data for which this ratio has anomalous values [84, 86, 111]. The lack of data for ^{118}Te makes it impossible to perform a χ^2 fit. For ^{120}Te, Q_0^2 was fixed to the only experimental value, giving rise to a range of acceptable $B(E2)$ values for decays from the two-phonon states.

The comparisons between experimental and calculated $B(E2)$ values (in Weisskopf units) for each individual nucleus are reported in Table 2.3. The decays from the one- and two-phonon states can be found on the left and right sides of

Table 2.3: $B(E2)$ values (in Weisskopf units) for decays from states below the three-phonon level in the ensemble of all studied nuclei. The theoretical uncertainty is given by 68% DOB intervals for the normalized residual for $B(E2)$ values.

	$B(E2, N=1 \to N=0)$		$B(E2, N=2 \to N=1)$			
Nucleus	$2_1^+ \to 0_1^+$	EFT	$0_2^+ \to 2_1^+$	$2_2^+ \to 2_1^+$	$4_1^+ \to 2_1^+$	EFT
^{62}Ni	12.1(4)	11(4)	42(23)	14.9(42)	21(6)	21(7)
^{98}Ru	31(1)	28(9)		47(5)	57.6(40)	56(19)
^{100}Ru	35.6(4)	24(8)	35(5)	30.9(4)	51(4)	47(16)
^{106}Pd	44.3(15)	30(10)	35(8)	44(4)	76(11)	61(20)
^{108}Pd	49.5(13)	37(12)	52(5)	71(5)	73(8)	74(25)
^{110}Cd	27.0(8)	21(7)		30(5)	42(9)	42(14)
^{112}Cd	30.2(3)	23(8)	51(14)	15(3)	61(6)	46(15)
^{114}Cd	31.1(19)	22(7)	27.4(17)	22(6)	62(4)	43(15)
^{120}Te	31 (6)	31(10)				62(21)
^{122}Te	36.9(3)	41(14)		100(30)		81(27)

the table, respectively. Experimental data for the transition between the initial state I_i and the final state I_i can be found under the columns labeled by $I_i \to I_f$, while calculations within the EFT can be found under the columns labeled by EFT. The theoretical uncertainty is given by 68% DOB intervals for the pdf for the normalized residual for the $B(E2)$ values, whose functional form is analogous to that of Equation (2.36), if Gaussian priors with a scale factor set to $s = 1$ are assumed for the expansion coefficients $\mathscr{D}_i$. Notice that even small $B(E2)$ values for decays from non yrast two-phonon states are consistent with the EFT within theoretical uncertainty.

Excluding ^{118}Te and ^{120}Te, it is possible to compare the EFT against the data set of $B(E2)$ values for decays from the one- and two-phonon states in the ensemble of nuclei studied in this work. This comparison is shown in Figure 2.10. There, the experimental data and LO calculations are shown as black and red lines respectively. The theoretical uncertainty, displayed as a shaded red area, was obtained from 68% DOB intervals for the pdf for the $B(E2)$ values. The mentioned pdf was obtained assuming a Gaussian prior for the expansion coefficients $\mathscr{D}_i$ with a scale factor $s = 1$. Such a pdf is equivalent to that in Equation (2.36). The choice of the scale factor $s = 1$ leads to a conservative theoretical uncertainty, within 81% of the normalized $B(E2)$ values for decays from the one- and two-phonon states lie. Once again, this is in agreement with the expected 68% within one standard deviation $\sigma = \sqrt{1/32} = 18\%$ defined by the size of the data set.

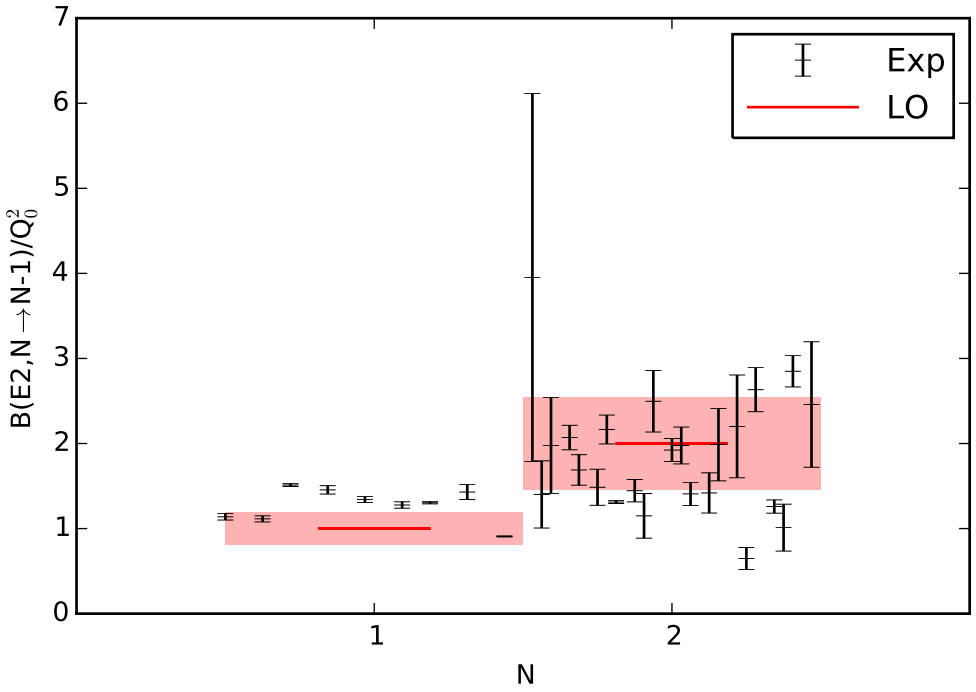

Figure 2.10: Normalized $B(E2)$ values for decays from the one- and two-phonon states in the ensemble of the nuclei studied in this work. Experimental $B(E2)$ values are shown as black lines. Experimental and theoretical uncertainty are shown as error bars.

2.4.2 Static quadrupole moments

Predictions within the EFT on the static quadrupole moments of the 2_1^+, 2_2^+ and 4_1^+ states and transitions between two-phonon states are compared to experimental data for the palladium isotopes studied in this work and ^{114}Cd. This comparison is shown in Figure 2.11 for palladium isotopes and Figure 2.12 for ^{114}Cd. For the palladium isotopes, data were taken from Ref. [56]. For ^{114}Cd data were taken from Ref. [112]. For all these nuclei, the static quadrupole moments of the 2_1^+, 2_2^+ and 4_1^+ states were employed to fix the LEC Q_1 via χ^2 fits. These fits lead to $Q_1 = -0.14\,e\text{b}$ in palladium isotopes and $Q_1 = -0.09\,e\text{b}$ in ^{114}Cd. Recall that for a nucleus with A nucleons W. U. $= 5.94 \times 10^{-6} A^{4/3}\ e^2\text{b}^2$. This expression allow us to compare the sizes of the LECs Q_0 and Q_1 in these nuclei. The ratios $Q_1/Q_0 = 0.47, 0.41, 0.33$ for ^{106}Pd, ^{108}Pd and ^{114}Cd, respectively, are all consistent with $\sqrt{\omega/\Lambda} \sim \sqrt{1/3} \sim 0.58$. On the right side of Figures 2.11 and 2.12, predictions for the absolute values of the reduced matrix elements for transitions between two-phonon states are compared to the absolute values of reduced matrix elements obtained from experimental data. It is clear that the strength of these transitions is of natural size within the EFT.

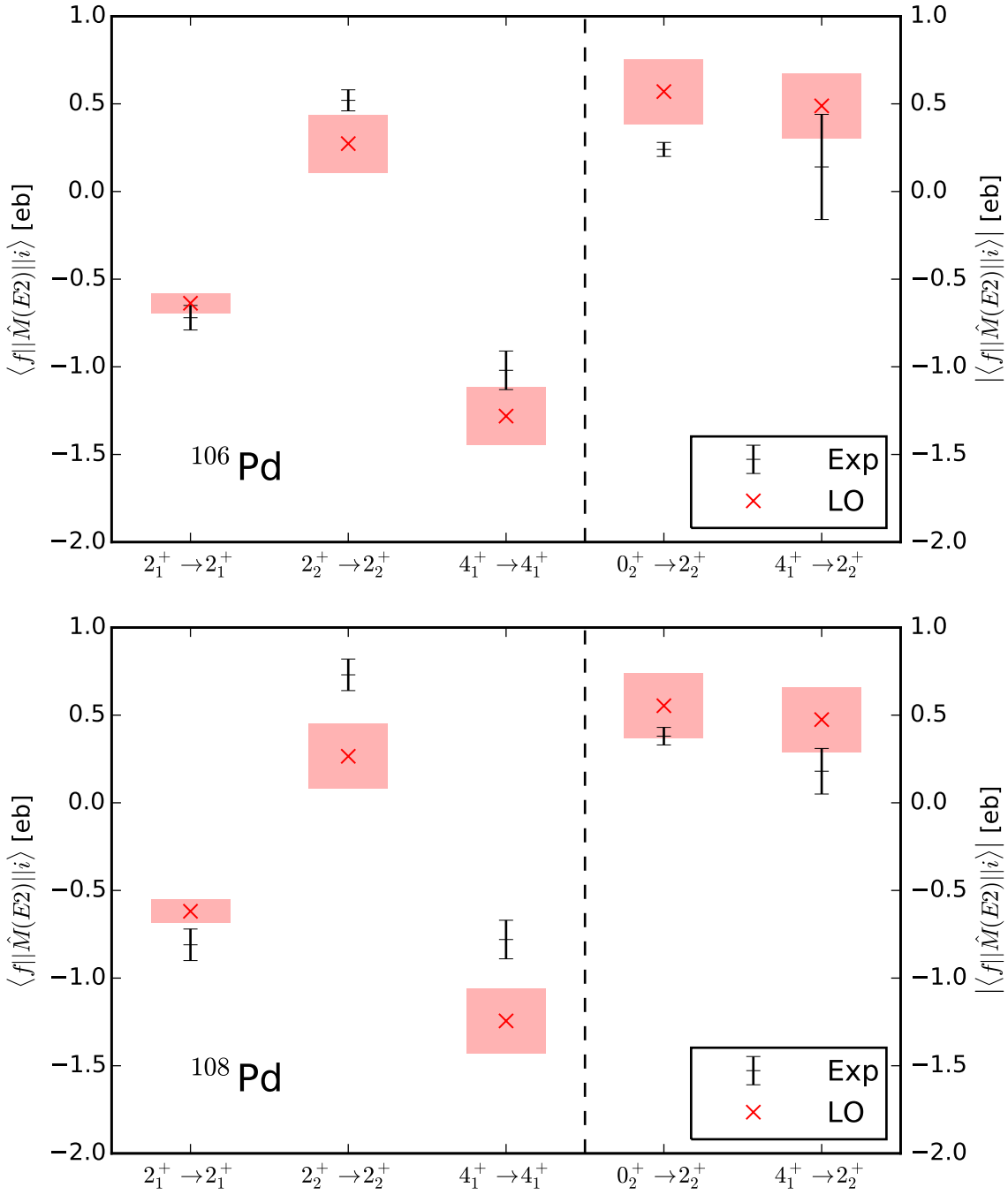

Figure 2.11: Comparison between data and EFT results for the reduced quadrupole matrix elements in ^{106}Pd (top) and ^{108}Pd (bottom). Experimental data are shown as black lines, while EFT results from LO calculations are shown as red crosses with uncertainties as shaded 68% DOB intervals. The left part shows diagonal quadrupole matrix elements employed in the fit of the LEC constant Q_1. The right part shows predictions for the absolute values of the reduced quadrupole matrix elements governing $E2$ transitions between two-phonon states.

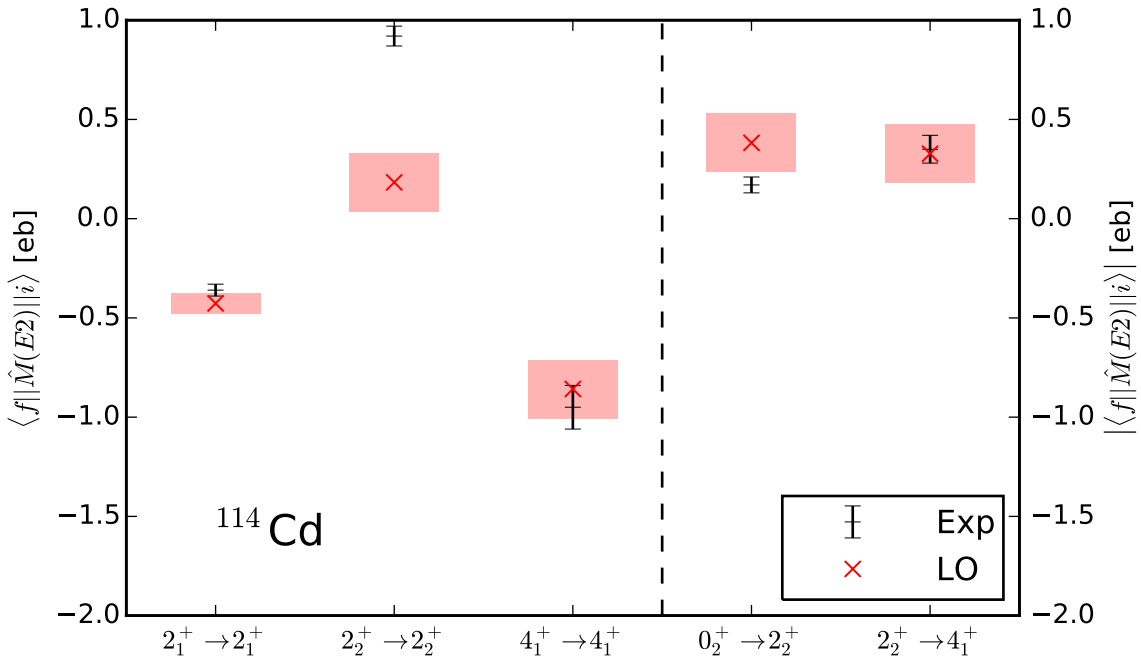

Figure 2.12: Comparison between data and EFT results for the reduced quadrupole matrix elements in ^{114}Cd. Experimental data are shown as black lines, while EFT results from LO calculations are shown as red crosses with uncertainties as shaded 68% DOB intervals. The left part shows diagonal quadrupole matrix elements employed in the fit of the LEC constant Q_1. The right part shows predictions for the absolute values of the reduced quadrupole matrix elements governing $E2$ transitions between two-phonon states.

2.5 Summary

In this Chapter, the EFT for nuclear vibrations coupled to an electromagnetic field was developed in order to consistently describe the energy spectra and electric quadrupole reduced transition probabilities of nuclei near shell closures. At LO, the energy spectrum and electric quadrupole transition probabilities for decays from multiphonon states are equal to those predicted by the Bohr collective model. The systematic construction of the effective Hamiltonian allows us to identify the relevant corrections at NLO, which differ from those used by phenomenological models.

The systematic construction of the Hamiltonian allows one to write the energy as an effective expansion in terms of the small quantity Q. Calculations within the EFT at a given order truncate this expansion. In this work, Bayesian statistics were employed to calculate the pdf function for the missing contribution to the energies. The key ingredients for this calculation are the priors for the expansion

coefficients, which encode assumptions on the size of such coefficients. Different functional forms for these priors yield similar results as long as the assumptions are correct. The pdf for the missing contribution is calculated and used to quantify the theoretical uncertainty at each order. This quantification gives a statistical interpretation to the theoretical uncertainty. A similar procedure can be employed to quantify the theoretical uncertainties in calculated electric quadrupole reduced transition probabilities for decays from multiphonon states.

In nuclei near shell closures, the appearance of nonvibrational states at low-energies suggests that none of these nuclei should be expected to exhibit quadrupole excitations beyond the two-phonon level.

Electric quadrupole reduced transition probabilities for decays from states up to the two-phonon level are consistent with the EFT at LO. The construction of the most general $E2$ operator from nonminimal coupling terms between the effective DOF and an electric field, allows for the precise description of nonvanishing static quadrupole moments and $E2$ reduced matrix elements for transitions between two-phonon states in palladium isotopes and ^{114}Cd. The scale of these reduced matrix elements is completely understood from the power counting.

All of the nuclei studied in this Chapter can be characterized as anharmonic vibrators up to the two-phonon level, based on the statistical comparison between data and calculations within the EFT. The existence of states fulfilling the requirements to be characterized as three-phonon excitations is unlikely, because of the low breakdown scale Λ. In general, experimental data on $E2$ reduced transition probabilities and static quadrupole moments with higher precision would be desired. It would be particularly interesting to measure the lifetimes of excited states in tellurium isotopes, which within the EFT approach are the ones with a behavior closest to that of a harmonic vibrator.

3
ROTATIONAL NUCLEI

Many heavy nuclei far from shell closures exhibit energy spectra consisting of rotational excitations on top of vibrational bandheads. Figure 1.1 shows the full energy spectrum of ^{168}Er, one of the most extensively studied nuclei, below 2 MeV. In this figure, the separation of scales between the energies of the rotational and vibrational modes, denoted by ξ and ω, respectively, is evident. The excitation energy of the rotational mode is $\xi \sim 80$ and $\xi \sim 40$ keV for nuclei in the rare-earth and actinide regions, respectively, while that of the vibrational mode lies around 1 and 0.6 MeV in rare-earth nuclei and actinides. This kind of spectrum is correctly described within the adiabatic Bohr model if an axially symmetric shape is assumed for the atomic nucleus. Within this model, electric quadrupole reduced transition probabilities for inband transitions are well reproduced. However, interband transitions tend to be overpredicted by factors ranging from two to ten [25]. Studies on the electromagnetic properties of the 0_2^+ state in deformed nuclei [67, 113] aim to characterize such states as either collective or noncollective. Such characterization is based on the consistency between experimental data and predictions by diverse collective models. In this chapter, the EFT for the axially-symmetric nonrigid rotor coupled to an electromagnetic field developed in Ref. [29] is described in detail. A model-independent and consistent description of the energy spectra and electric quadrupole reduced transition probabilities is provided. The expansion parameter of the EFT scales as $\xi/\omega \sim 1/10$ in rotational nuclei. Nuclei for which the deformation of the ground state is small, known as transitional nuclei, are characterized by expansion parameters $\xi/\omega \sim 1/5$. One of the main results in [29] is the accurate description of interband transitions at the expense of two LECs. It is important that consistency between experimental data and the EFT is achieved for LECs of natural size.

3.1 Effective field theory for the ground band

Let us start reviewing the EFT for deformed nuclei developed in Refs. [26, 27, 28] for energies below the vibrational excitation energy ω. Below such an energy, the spectra of many nuclei in the rare earth and actinide regions of the nuclear chart exhibit a pattern with great resemblance to that of a rotational system, suggesting their description in terms of rotational DOF. We study the behavior of these

DOF under rotations in order to establish the building blocks for the EFT. At LO, the Hamiltonian constructed from such building blocks is equivalent to that of a particle restricted to move on the two-sphere, that of a rigid rotor, or that of the rotor submodel of the Bohr collective model. Also, the EFT is equivalent to the variable moment of inertia (VMI) model [114] as will be discussed later in this chapter. Within the EFT approach it is possible to estimate the theoretical uncertainty at each order. This theoretical uncertainty allows a meaningful comparison between experimental data and calculations within the EFT.

3.1.1 Rotational degrees of freedom and rotational invariance

As mentioned before, many nuclei exhibit low-energy spectra with an extraordinary resemblance to that predicted for a rigid rotor. States that cannot be characterized as rotational excitations appear at energies around ten times larger than the excitation energy of the rotational mode. This separation of scales motivates us to study these nuclei within an EFT for nonrigid rotors, written in terms of rotational DOF.

The EFT is based on the symmetry breaking from the rotational symmetry group $\mathcal{G} = \mathrm{SO}(3)$ of the Hamiltonian, to the axial symmetry subgroup $\mathcal{H} = \mathrm{SO}(2)$ assumed for the system at low-energies. The Nambu-Goldstone modes due to the broken symmetry are replaced by quantized time-dependent modes in finite systems [115, 36, 28], and must parametrize the coset $\mathcal{G}/\mathcal{H} = \mathrm{SO}(3)/\mathrm{SO}(2)$, where physics take place at low-energies [33, 32, 35, 116, 117, 118, 119]. This coset is isomorph to the two-sphere, parametrized by the polar and azimuthal angles θ and ϕ, from now on referred to as orientation angles, through the unit vector

$$\mathbf{e}_r \equiv \begin{pmatrix} \sin\theta\cos\phi \\ \sin\theta\sin\phi \\ \cos\theta \end{pmatrix}. \tag{3.1}$$

These orientation angles can be employed as the rotational DOF in terms of which the EFT for the nonrigid rotor will be written. The unit vector $\mathbf{e}_r$ has a very simple interpretation. It represents the orientation of the symmetry axis of the nonrigid rotor with respect to the laboratory reference frame. From now on this unit vector is referred to as orientation vector.

The dynamics of the system are then determined by the velocity vector $\mathbf{v}$, given

by the time derivative of the orientation vector

$$\begin{aligned}\mathbf{v} &\equiv d_t \mathbf{e}_r \\ &= \dot{\theta}\mathbf{e}_\theta + \dot{\phi}\sin\theta\mathbf{e}_\phi \\ &\equiv v_\theta \mathbf{e}_\theta + v_\phi \mathbf{e}_\phi.\end{aligned} \tag{3.2}$$

Here, dots are employed to denote the time derivative of a coordinate. The unit vectors

$$\mathbf{e}_\theta \equiv \begin{pmatrix} \cos\theta\cos\phi \\ \cos\theta\sin\phi \\ -\sin\theta \end{pmatrix}, \qquad \mathbf{e}_\phi \equiv \begin{pmatrix} -\sin\phi \\ \cos\phi \\ 0 \end{pmatrix}, \tag{3.3}$$

span a plane tangent to the orientation vector. From now on this plane is referred to as the tangent plane.

The effective Lagrangian must be invariant under rotations and time reversal. Thus, in order to construct the EFT, it is necessary to understand the behavior of the velocity $\mathbf{v}$ under rotations. Under an SO(3) rotation r defined by

$$r \equiv r(\alpha,\beta,\gamma) = \exp\left(-i\alpha\hat{I}_z\right)\exp\left(-i\beta\hat{I}_y\right)\exp\left(-i\gamma\hat{I}_z\right), \tag{3.4}$$

where α, β and γ are Euler angles, and $\hat{I}_i$, with $i = x, y, z$, are the Cartesian components of the angular momentum operator, the orientation angles θ and ϕ transform into a new set of orientation angles θ' and ϕ' (see Ref. [50] for details on such transformation). Thus, this SO(3) rotation transforms the velocity $\mathbf{v}$ into a new vector $\mathbf{v}'$ with components $v'_i = v_i$, with $i = \theta, \phi$, in the directions of the new unit vectors $\mathbf{e}'_i \equiv \mathbf{e}_i(\Omega')$, with $i = \theta, \phi$, that span a plane tangent to new orientation vector $\mathbf{e}'_r \equiv \mathbf{e}_r(\Omega')$. In other words, the rotation r is equivalent to an SO(2) rotation g in the tangent plane defined by the matrix

$$g \equiv g(\chi) = \begin{bmatrix} \cos\chi & -\sin\chi \\ \sin\chi & \cos\chi \end{bmatrix}, \tag{3.5}$$

which acts on the tangential components of a vector. The angle χ is a complicated function of the original orientation angles, and the Euler angles of the transformation (see, e.g. [50]). Under g, the components of the velocity $\mathbf{v}$ transform as

$$v_\theta \to v_\theta\cos\chi - v_\phi\sin\chi, \qquad v_\phi \to v_\theta\sin\chi + v_\phi\cos\chi. \tag{3.6}$$

Thus, under an SO(3) rotation, the velocity $\mathbf{v}$ is transformed as it is under an

SO(2) rotation in the tangent plane. This constitutes a nonlinear realization of the SO(3) symmetry group. Consequently, if a Lagrangian built from objects in the tangent plane is formally invariant under SO(2), it is also invariant under SO(3).

It is convenient to introduce the spherical components of the velocity in the tangent plane, defined by

$$v_{\pm 1} \equiv \sqrt{\frac{1}{2}}(v_\theta \pm i v_\phi). \tag{3.7}$$

Under g these components transform as

$$v_{\pm 1} \to \exp(\pm i\chi) v_{\pm 1}. \tag{3.8}$$

The construction of SO(2) invariant Lagrangians in terms of these spherical components is straightforward. As an example, let us consider the term $v_{+1}v_{-1}$. Under the SO(2) rotation g it transforms as

$$\begin{aligned} v_{+1}v_{-1} \to\ & \exp(i\chi)v_{+1}\exp(-i\chi)v_{-1} \\ =\ & v_{+1}v_{-1}. \end{aligned} \tag{3.9}$$

Thus, this term is invariant under both SO(2) and SO(3). This construction method is particularly useful when external DOF are coupled to the orientation angles, as will be discussed in Section 3.3.

This approach is different from the one employed for the Bohr collective model, where the function describing the nuclear surface $R \equiv R(\theta, \phi)$ is written as an expansion in terms of spherical harmonics, and the expansion coefficients are used as DOF [22, 23, 24, 25]. That is a linear representation of SO(3). The later transformation to the β_μ DOF introduces a nonlinear realization of SO(3) in terms of three Euler angles and two additional coordinates, as discussed in Chapter 1.

According to Noether's theorem, the conserved quantity of a rotationally invariant Lagrangian L written in terms $v_{\pm 1}$ is the angular momentum $\mathbf{I}$ of the system [26]. The spherical components I_{+1}, I_0 and I_{-1} are [50]

$$\begin{aligned} I_{+1} &= -\sqrt{\frac{1}{2}}e^{i\phi}(ip_\theta - p_\phi \cot\theta), \\ I_0 &= p_\phi, \\ I_{-1} &= -\sqrt{\frac{1}{2}}e^{-i\phi}(ip_\theta + p_\phi \cot\theta), \end{aligned} \tag{3.10}$$

where

$$p_\theta \equiv \partial_{\dot\theta} L, \qquad p_\phi \equiv \partial_{\dot\phi} L, \tag{3.11}$$

are the canonical momenta. In terms of these spherical components, the angular momentum squared can be written as

$$\begin{aligned} I^2 &= \sum_\mu (-1)^\mu I_\mu I_{-\mu} \\ &= p_\theta^2 + \frac{p_\phi^2}{\sin^2\theta}. \end{aligned} \tag{3.12}$$

The Hamiltonian of the EFT can be written as a series in powers of this rotational invariant.

3.1.2 Power counting and the next-to-leading order Hamiltonian

The simplest rotationally invariant Lagrangian is quadratic in the spherical components of $\mathbf{v}$

$$\begin{aligned} L_{\rm LO} &= C_0 v_{+1} v_{-1} \\ &= \frac{C_0}{2}\left(\dot\theta^2 + \dot\phi^2 \sin^2\theta\right). \end{aligned} \tag{3.13}$$

It is equivalent to that of a particle restricted to move on the two-sphere or that of a rigid rotor. The LEC C_0 may be thought of as the effective mass or the effective moment of inertia of the system, respectively. This parameter of the EFT must be fit to data.

The Legendre transformation of the LO Lagrangian yields the LO Hamiltonian

$$\begin{aligned} H_{\rm LO} &= \frac{1}{2C_0}\left(p_\theta^2 + \frac{p_\phi^2}{\sin^2\theta}\right) \\ &= \frac{1}{2C_0} I^2. \end{aligned} \tag{3.14}$$

A standard quantization transforms the angular momentum into the angular momentum operator $\hat{\mathbf{I}}$. The spherical components of this operator are [50]

$$\begin{aligned} \hat I_{+1} &= -\sqrt{\frac{1}{2}} e^{i\phi}\left(\partial_\theta + i\cot\theta\partial_\phi\right), \\ \hat I_0 &= -i\partial_\phi, \\ \hat I_{-1} &= -\sqrt{\frac{1}{2}} e^{-i\phi}\left(\partial_\theta - i\cot\theta\partial_\phi\right), \end{aligned} \tag{3.15}$$

as clearly seen from Equation (3.10). The eigenfunctions of the LO Hamiltonian (3.14) are spherical harmonics $Y_{IM}(\theta, \phi)$, and the energy spectrum is

$$E_{\mathrm{LO}}(I) = \frac{1}{2C_0} I(I+1). \tag{3.16}$$

To make progress, it is necessary to establish the power counting for the EFT. It is clear that the LO Lagrangian (3.13) must scale as ξ. Since the angles θ and ϕ are of order one, and $1/\Delta t \sim \Delta E$ according to Heisenberg's uncertainty principle, the naive scales of the components $v_{\pm 1}$ and the LEC C_0 are

$$v_{\pm 1} \sim \dot{\phi} \sim \dot{\theta} \sim \xi, \qquad C_0 \sim \xi^{-1}. \tag{3.17}$$

Deviations from the LO behavior can be accounted for by higher-order corrections to the LO Lagrangian (3.13). Such correction terms are proportional to higher powers of the rotational invariant $v_{+1}v_{-1}$. At NLO, the Lagrangian takes the form $L_{\mathrm{NLO}} = L_{\mathrm{LO}} + \Delta L_{\mathrm{NLO}}$ with

$$\Delta L_{\mathrm{NLO}} = C_2 (v_{+1} v_{-1})^2. \tag{3.18}$$

The Legendre transformation of the NLO Lagrangian yields the corresponding NLO Hamiltonian $H_{\mathrm{NLO}} = H_{\mathrm{LO}} + \Delta H_{\mathrm{NLO}}$ with

$$\begin{aligned} \Delta H_{\mathrm{NLO}} &= -\frac{C_2}{4C_0^4} \left(I^2\right)^2 \\ &= -\frac{C_2}{C_0^2} \left(H_{\mathrm{LO}}\right)^2 . \end{aligned} \tag{3.19}$$

Its eigenfunctions are also spherical harmonics, and the spectrum takes the form

$$E_{\mathrm{NLO}}(I) = \frac{1}{2C_0} I(I+1) - \frac{C_2}{4C_0^4} \left[I(I+1)\right]^2 . \tag{3.20}$$

Notice that C_2 must have units of energy^{-3}, and that the NLO correction arises due to high-energy modes at the energy scale ω where the EFT breaks. From here, the ratio of LECs $C_2/C_0 \sim \omega^{-2}$ is expected [26], implying that

$$C_2 \sim C_0/\omega^2 \tag{3.21}$$

and the ratio of the NLO correction to the LO contribution to the energies is expected to scale as

$$\frac{\langle \hat{H}_{\mathrm{NLO}} \rangle}{\langle \hat{H}_{\mathrm{LO}} \rangle} \sim \left(\frac{\xi}{\omega}\right)^2 I(I+1). \tag{3.22}$$

From here, the EFT is expected to break at a spin I_b for which the ratio (3.22) is of order one. For a given nucleus, $I_b \sim \omega/\xi$ is a naive estimate for this breakdown spin. An alternative estimate can be made from the LECs C_0 and C_2, as $I_b \sim \sqrt{C_0^3/C_2}$. This estimate agrees better with data than the naive one for the systems studied for this work. Thus, the EFT for nonrigid rotors is equivalent to the VMI model [114, 120], and the energy spectrum can be written as a series in powers of $I(I+1)$.

3.1.3 Energy uncertainty estimation

Unlike collective models employed to describe the low-energy behavior of rotational systems, the EFT approach allows us to estimate theoretical uncertainty at each order due to the omission of higher-order terms in the Hamiltonian or any other operator. This estimate is a highlight of EFT approaches (see Refs. [39, 38]).

In calculations for rotational nuclei for chronological reasons Bayesian analysis tools were not employed to quantify the theoretical uncertainty. Rotational systems were studied before vibrational systems, for which the quantification of the theoretical uncertainty was developed. The estimation of the theoretical uncertainty presented in this section is more rudimentary; nevertheless, it will suffice to compare experimental data against the EFT.

According to the EFT for the nonrigid rotor, the energy spectrum can be written as an expansion in powers of the parameter $Q \equiv (\xi/\omega)I(I+1)$ as

$$E = E_0 Q + \sum_i \mathscr{C}_i Q^i E_0, \tag{3.23}$$

with $i \geq 2$, and where the expansion coefficients $\mathscr{C}_i$ are expected to be of order one. This expansion allows for the estimation of the scale of the contribution to the energy by omitted terms at each order. Well below the breakdown scale, Q is a small parameter. The theoretical uncertainty is naively expected to scale as Q^2 in LO calculations, as Q^3 in NLO calculations, and so on. In general, the theoretical uncertainty in calculations at order k in the EFT are naively expected to scale as Q^{k+1}.

This naive analysis provides uncertainty estimates only. In other words, it estimates the scale of the theoretical uncertainty, and not its precise value. Let us write the theoretical uncertainty at order k as $\sigma_{\text{th}}^{(k)} = \alpha^{(k)} Q^{k+1}$, where $\alpha^{(k)}$ is a parameter expected to be of order one, that is, $1/3 \lesssim \alpha^{(k)} \lesssim 3$, for the

uncertainty to be in agreement with the naive estimate. Choosing $\alpha^{(k)} = 1$ is a simple way to present the theoretical uncertainty in EFT calculations, similar to the idea of presenting order-of-magnitude estimates for remainders in polynomial approximations to functions.

In what follows, $\alpha^{(k)}$ is chosen such that a reduced χ^2 of one is obtained from fits to data that employ the theoretical uncertainty $\sigma_{\text{th}}^{(k)}$. The theoretical uncertainty may be thought of as the statistical one-σ band, where 68% of the data must lie for it to be consistent with the EFT. If the studied system is well described by this theory, the theoretical uncertainty at order $k+1$ is expected to overlap with that at order k, since the data must be described at each order within theoretical uncertainty.

At a given order, a value $\alpha^{(k)} \ll 1$ resulting from a χ^2 fit indicates that the EFT describes the data within the experimental uncertainty. In this case, a higher-order description would require experimental data with higher precision. On the other hand, a very large value of $\alpha^{(k)} \gg 1$ signals the breakdown of the theory, since a large uncertainty implies large contributions from higher order terms, which is inconsistent with the effective expansion (3.23).

When comparing to data, the LECs C_0 and C_2 are computed from the experimental energies of the 2^+ and 4^+ states in the ground-state rotational band. The uncertainty of these LECs can be neglected because energies are known with high precision. Then, we perform χ^2 fits to data

$$\chi^2 = \sum_d \left[\frac{E_{\text{exp}}(d) - E_{\text{th}}^{(k)}(d)}{\sigma_{\text{th}}^{(k)}(d)} \right]^2 \tag{3.24}$$

varying the uncertainty parameter until a reduced χ^2 of one is obtained, in agreement with statistical analysis [39]. In equation (3.24), the sum is over all data points, and $E_{\text{exp}}(d)$ and $E_{\text{th}}^{(k)}(d)$ are the experimental energies and the theoretical energies at order k, respectively. The reduced χ^2, or χ^2 per DOF, is defined as

$$\chi^2_{\text{pdof}} = \frac{\chi^2}{N_d - N_p^{(2n)}}, \tag{3.25}$$

where N_d and $N_p^{(k)}$ are the number of data points and LECs at order k, respectively.

3.2 Effective field theory for the nonrigid rotor with vibrations

The nonrigidity of the nucleus can be explicitly taken into account by the introduction of three additional DOF representing vibrational modes. The explicit inclusion of these DOF raises the breakdown scale, allowing us to describe the system at higher energies. First, we study the behavior of the vibrational DOF under rotations, and the scale of rotationally invariant terms involving them, in order to systematically construct the EFT. At NLO, the Hamiltonian constructed from these blocks yields an energy spectrum consisting of rotational bands on top of vibrational excitations, equivalent to that of the adiabatic Bohr model [25]. NNLO corrections to this Hamiltonian are important for the accurate description of interband transitions, as will be discussed in Section 3.3. Deformed and transitional nuclei in the rare earth and actinide regions exhibit spectra with this pattern, suggesting their description in terms of the EFT. A naive estimate for the theoretical uncertainty in the NLO energy spectrum is given.

3.2.1 Vibrational degrees of freedom and rotational invariance

The energy spectra of even-even nuclei in the rare earth and actinide regions of the nuclear chart suggest us to write the EFT for the nonrigid rotor in terms of quadrupole DOF. Thus, the Nambu-Goldstone modes due to the emergent symmetry breaking from the SO(3) symmetry to the SO(2) symmetry are represented as a quadrupole field with two of its components replaced by the rotational DOF $v_{\pm 1}$. These quadrupole DOF are different from the ones employed by Bohr's to describe surface quadrupole oscillations, as discussed in Section 3.1.

The quadrupole field is in the intrinsic reference frame. In other words, it can be thought of as being attached to the particle restricted to move on the two-sphere employed to describe the nonrigid rotor at low energies. We write the field in this reference frame as

$$\Psi = (\Psi_{+2}, 0, \Psi_0, 0, \Psi_{-2})\,. \tag{3.26}$$

In order to facilitate the construction of rotationally invariant Lagrangians, we write the components Ψ_i, $i = \pm 2, 0$, from now on referred to as vibrational DOF, as

$$\Psi_0 = \zeta + \psi_0, \qquad \Psi_{\pm 2} = \psi_2 e^{\pm i 2\gamma}, \tag{3.27}$$

where ζ is the non-zero vacuum expectation value of Ψ_0, associated with the deformation of the system, and ψ_0 represents small oscillations around such value.

The phase in the exponentials is written as $\pm i2\gamma$ for convenience, and constrains the angle γ to $0 \leq \gamma \leq \pi$. The scales of these DOF are

$$\dot{\psi_0} \sim \dot{\psi_2} \sim \omega^{1/2}, \qquad \psi_0 \sim \psi_2 \sim \omega^{-1/2}, \qquad \zeta \sim \xi^{-1/2}, \qquad \dot{\gamma} \sim \omega. \tag{3.28}$$

A detailed discussion on this scales will be given later.

The vibrational DOF may be thought of as a "vector" with radial component Ψ_0 and spherical components in the tangent plane $\Psi_{\pm 2}$. Thus, under the SO(3) rotation $r(\alpha, \beta, \gamma)$ they transform as

$$\psi_0 \to \psi_0, \qquad \psi_2 \to \psi_2, \qquad \gamma \to \gamma + \chi, \tag{3.29}$$

where the angle χ is the same complicated function of the original orientation angles and the Euler angles of the rotation of Section 3.1. Similarly to the spherical components of $\mathbf{v}$, the vibrational DOF transform under an SO(3) rotation as they will under an SO(2) rotation in the tangent plane. Consequently, the rotational symmetry is realized nonlinearly by all the DOF of the EFT [26].

The most general rotationally invariant Lagrangian must be constructed from vectors in the tangent plane and their time derivatives. The time derivatives of such vectors possess components outside the tangent plane in general. For low-energy physics to lie in the tangent plane, the ordinary time derivative d_t must be replaced by the covariant time derivative, defined by

$$D_t \equiv d_t - i\dot{\phi} \cos\theta \hat{I}_z, \tag{3.30}$$

which is the projection of the ordinary time derivative onto the tangent plane. Thus, any Lagrangian L written in terms of $v_\pm$, $\Psi_{\pm 2}$, Ψ_0, $D_t\Psi_{\pm 2}$ and $D_t\Psi_0$ that is formally invariant under SO(2), is actually invariant under SO(3) due to the nonlinear realization of the rotational symmetry.

According to Noether's theorem, the conserved quantity of a rotationally invariant Lagrangian L written in terms of the quadrupole field Ψ and its covariant time derivative is the total angular momentum $\mathbf{J}$ of the system [26]. The coupling between rotational and vibrational DOF makes the total angular momentum $\mathbf{J}$ different from the angular momentum $\mathbf{I}$ of the EFT developed for a single rotational

band. Its spherical components are [26]

$$\begin{aligned} J_{+1} =& -\sqrt{\frac{1}{2}}e^{i\phi}(ip_\theta - p_\phi \cot\theta) - \sqrt{\frac{1}{2}}e^{i\phi}\frac{p_\gamma}{\sin\theta}, \\ J_0 =& p_\phi, \\ J_{-1} =& -\sqrt{\frac{1}{2}}e^{-i\phi}(ip_\theta + p_\phi \cot\theta) + \sqrt{\frac{1}{2}}e^{-i\phi}\frac{p_\gamma}{\sin\theta}, \end{aligned} \tag{3.31}$$

where

$$p_\theta \equiv \partial_{\dot\theta} L, \qquad p_\phi \equiv \partial_{\dot\phi} L, \qquad p_\gamma \equiv \partial_{\dot\gamma} L, \tag{3.32}$$

are the canonical momenta, and the total angular momentum squared is

$$\begin{aligned} J^2 =& \sum_{-\mu} (-1)^\mu J_\mu J_{-\mu} \\ =& p_\theta^2 + \left(\frac{p_\phi - p_\gamma \cos\theta}{\sin\theta}\right)^2 + p_\gamma^2. \end{aligned} \tag{3.33}$$

The total angular momentum of the system can be written as

$$\mathbf{J} = \mathbf{e}_r \times \mathbf{p}_{\Omega\gamma} + \mathbf{e}_r p_\gamma. \tag{3.34}$$

where

$$\mathbf{p}_{\Omega\gamma} = \mathbf{e}_\theta p_\theta + \mathbf{e}_\phi p_{\phi\gamma}, \qquad p_{\phi\gamma} \equiv \frac{p_\phi - p_\gamma \cos\theta}{\sin\theta}, \tag{3.35}$$

is the component of the total angular momentum in the tangent plane. In expression (3.34) the total angular was decomposed into a contribution in the tangential plane associated to rotations that change the orientation of the symmetry axis $\mathbf{e}_r$, and a contribution in the direction of such axis, associated to rotations around this vector. For quantum systems, rotations around $\mathbf{e}_r$ can only take place after the axial symmetry is broken by a vibrational excitation.

3.2.2 Power counting and the next-to-next-to-leading order Hamiltonian

The effective Lagrangian must be invariant under rotations and time reversal. Its systematic construction requires us to employ the naive scales of the DOF, in order to identify relevant terms at each order. The scales in Equation (3.28) arise from the following reasoning [26]. First, it is required that the scale of the dimensionfull DOF ψ_i with $i = 0, 2$ is such that $\dot\psi_i^2 \sim \omega$. Recall that the vacuum expectation value of Ψ_0 is associated with the rotational mode and its energy scale ξ. Also, recall that the angle γ is of order one, and $1/\Delta t \sim \Delta E$.

The naive scale of the vibrational DOF combined with the power counting (3.17), is sufficient to estimate the size of any rotational invariant contribution to the Lagrangian. The LO contribution

$$L_{\mathrm{LO}} = \frac{1}{2}\dot{\psi}_0^2 + \dot{\psi}_2^2 + 4\dot{\gamma}^2\psi_2^2 - \frac{\omega_0^2}{2}\psi_0^2 - \frac{\omega_2^2}{4}\psi_2^2 \tag{3.36}$$

describes vibrations at the high-energy scale ω. The LECs ω_0 and ω_2 in this contribution scale as

$$\omega_0 \sim \omega_2 \sim \omega, \tag{3.37}$$

and must be fit to data.

The NLO correction

$$\Delta L_{\mathrm{NLO}} = \frac{C_0}{2}\left(\dot{\theta}^2 + \dot{\phi}^2\sin^2\theta\right) + 4\psi_2^2\dot{\gamma}\dot{\phi}\cos\theta \tag{3.38}$$

scales as ξ, and couples vibrations to rotations. The LEC $C_0 \sim \xi^{-1}$ must be fit to data.

The highest-order contribution considered in this work is the next-to-next-to leading (NNLO) correction

$$\begin{aligned}\Delta L_{\mathrm{NNLO}} = {} & \frac{C_\beta}{2}\psi_0\left(\dot{\theta}^2 + \dot{\phi}^2\sin^2\theta\right) \\ & + \frac{C_\gamma}{2}\psi_2\left(\dot{\theta}^2 - \dot{\phi}^2\sin^2\theta\right)\cos 2\gamma + C_\gamma\psi_2\dot{\theta}\dot{\phi}\sin 2\gamma\sin\theta.\end{aligned} \tag{3.39}$$

It scales as $\xi(\xi/\omega)^{1/2}$ [26]. According to the scales (3.28) and (3.17) the LECs in this correction scale as

$$C_\beta \sim C_\gamma \sim \xi^{-1/2}. \tag{3.40}$$

The Legendre transformation of the NNLO Lagrangian $L_{\mathrm{NNLO}} = L_{\mathrm{LO}} + \Delta L_{\mathrm{NLO}} + \Delta L_{\mathrm{NNLO}}$ yields the NNLO Hamiltonian $H_{\mathrm{NNLO}} = H_{\mathrm{LO}} + \Delta H_{\mathrm{NLO}} + \Delta H_{\mathrm{NNLO}}$. In what follows, we solve the eigenvalue problem for the NLO Hamiltonian and treat the NNLO correction as a perturbation. We notice that at such order γ is a cyclic coordinate, implying that the component of the total angular momentum in the direction of the symmetry axis, p_γ, is a conserved quantity in addition to $\mathbf{J}$.

The LO contribution to the Hamiltonian

$$H_{\mathrm{LO}} = \frac{p_0^2}{2} + \frac{\omega_0^2}{2}\psi_0^2 + \frac{p_2^2}{4} + \frac{1}{4\psi_2^2}\left(\frac{p_\gamma}{2}\right)^2 + \frac{\omega_2^2}{4}\psi_2^2 \tag{3.41}$$

is equivalent to that of a harmonic oscillator with frequency ω_0 coupled to a two-dimensional harmonic oscillator with frequency ω_2[51]. The quantization

$$\hat{p}_0 = -i\partial_{\psi_0}, \qquad \hat{p}_2 = -i\partial_{\psi_2}, \qquad \hat{p}_\gamma = -i\partial_\gamma, \tag{3.42}$$

yields an eigenvalue problem which eigenstates, denoted as $|n_0 n_2 K/2\rangle$, can be written as the product of the states of a harmonic oscillator and the states of the two-dimensional oscillator

$$|n_0 n_2 K/2\rangle \equiv |n_0\rangle |n_2 K/2\rangle. \tag{3.43}$$

The quantum label n_0 is the number of excited quanta of the harmonic oscillator, while n_2 and $K/2$ are the number of excited radial and angular quanta of the two-dimensional harmonic oscillator. The quantum number K can only take even values, as will be discussed later.

In terms of the tangential component of the total angular momentum (3.35), the NLO correction in the effective Hamiltonian can be written as

$$\begin{aligned} \Delta H_{\text{NLO}} &= \frac{1}{2C_0}\mathbf{p}^2_{\Omega_\gamma} \\ &= \frac{1}{2C_0}\left[p_\theta^2 + \left(\frac{p_\phi - p_\gamma\cos\theta}{\sin\theta}\right)^2\right] \\ &= \frac{1}{2C_0}\left(J^2 - p_\gamma^2\right). \end{aligned} \tag{3.44}$$

This correction is equivalent to the Hamiltonian of a symmetric top [51]. A standard quantization yields the total angular momentum operator $\hat{\mathbf{J}}$. From Equation (3.31), the spherical components of this operator are

$$\begin{aligned} \hat{J}_{+1} =& i\sqrt{\frac{1}{2}}e^{i\phi}\left(-\cot\theta\partial_\phi + i\partial_\theta + \frac{1}{\sin\theta}\partial_\gamma\right), \\ \hat{J}_0 =& -i\partial_\phi, \\ \hat{J}_{-1} =& i\sqrt{\frac{1}{2}}e^{-i\phi}\left(\cot\theta\partial_\phi + i\partial_\theta - \frac{1}{\sin\theta}\partial_\gamma\right). \end{aligned} \tag{3.45}$$

The eigenvalue problem for this correction takes the form

$$\Delta\hat{H}_{\text{NLO}}|IMK\rangle = \frac{1}{2C_0}\left[I(I+1) - K^2\right]|IMK\rangle, \tag{3.46}$$

where the quantum labels I, M and K are the magnitude of the total angular

momentum, and its projections into the fixed and intrinsic z-axis, respectively. These states must be consistent with the positive $\mathcal{R}$ parity possessed by axially symmetric systems, as rotations of π around any axis perpendicular to the symmetry axis do not change the wave functions. Such functions are written as linear combinations of Wigner D-functions consistent with this symmetry

$$\langle \Omega\gamma | IMK \rangle = \sqrt{\frac{2I+1}{8\pi^2}} \left[D^I_{MK}(\phi,\theta,\gamma) + (-1)^I D^I_{M-K}(\phi,\theta,\gamma) \right]. \tag{3.47}$$

The Wigner D-functions fulfill the relations [50]

$$\begin{aligned} \hat{J}_z D^J_{MK}(\phi,\theta,\gamma) &= -\, M D^I_{MK}(\phi,\theta,\gamma), \\ \hat{J}_{z'} D^J_{MK}(\phi,\theta,\gamma) &= -\, K D^I_{MK}(\phi,\theta,\gamma), \\ \hat{\mathbf{J}}^2 D^J_{MK}(\phi,\theta,\gamma) &= I(I+1) D^I_{MK}(\phi,\theta,\gamma). \end{aligned} \tag{3.48}$$

The constraint in the range of the angle γ and the boundary conditions of the wave functions, limit the quantum number K to even values, as mentioned above. For $K = 0$, the wave function cannot take odd spin values due to the positive $\mathcal{R}$ parity. In this particular case, the wave functions take the form

$$\langle \Omega\gamma | IM0 \rangle = \sqrt{\frac{2I+1}{4\pi^2}} D^I_{M0}(\phi,\theta,\gamma) = \frac{(-1)^m}{\sqrt{\pi}} Y_{I-M}(\theta,\phi). \tag{3.49}$$

It is possible to solve the eigenvalue problem for the NLO Hamiltonian $H_{\rm LO} + H_{\rm NLO}$ exactly. The energy spectrum at this order takes the form

$$E_{\rm NLO}(n_0,n_2,I,K) = \omega_0 \left(n_0 + \frac{1}{2} \right) + \frac{\omega_2}{2} \left(2n_2 + \frac{K}{2} + 1 \right) + \frac{I(I+1) - K^2}{2C_0}. \tag{3.50}$$

It consists of rotational bands with rotational constant $1/2C_0$ on top of vibrational bandheads. The observed variation of the rotational constant from band to band is correctly described by the EFT at next-to-next-to-next-to-leading order ($\mathrm{N^3LO}$) [27]. Such variations depend linearly in the number of excited vibrational quanta. In analogy with the Bohr collective model, the bands on top of the bandheads with quantum numbers $n_0 = 1$, $n_2 = 0$, $K = 0$ and $n_0 = 0$, $n_2 = 0$, $K = 2$ will be referred to as β and γ band, respectively.

The NNLO correction in the effective Hamiltonian is

$$H_{\rm NNLO} = -\frac{1}{2C_0^2} \left(C_\beta \psi_0 \mathbf{p}^2_{\Omega\gamma} + C_\gamma \psi_2 \mathbf{p}^T_{\Omega\gamma} \hat{\Gamma} \mathbf{p}_{\Omega\gamma} \right), \tag{3.51}$$

where the matrix

$$\hat{\Gamma} \equiv \begin{bmatrix} \cos 2\gamma & \sin 2\gamma \\ \sin 2\gamma & -\cos 2\gamma \end{bmatrix} \tag{3.52}$$

acts on vectors in the tangent plane. The operator $\hat{H}_{\mathrm{NNLO}}$ arising from the quantization of this correction is off-diagonal when acting on the states of the NLO Hamiltonian, denoted as $|n_0 n_2 IMK\rangle$. Thus, it corrects the energies at second-order in perturbation theory, or N^{3}LO in the EFT. The inclusion of this correction is of importance for the accurate description of interband transitions, as will be discussed in Section 3.3.

Corrections to this Hamiltonian arise due to omitted physics at the breakdown scale $\Lambda \sim 3$ MeV, where pair-breaking effects become relevant and more DOF need to be explicitly taken into account [28]. Thus, deviations from the harmonic behavior of the vibrational bandheads are expected to scale as ω/Λ.

3.3 Electromagnetic coupling

In this section, an electromagnetic field is minimally coupled to the effective DOF by gauging the effective Hamiltonian. In Ref. [29], a toy model for nonrigid rotors was studied in order to gain insight on how this gauging must be done. The gauging leads to transition operators consistent with the Hamiltonian. This consistency is a highlight of EFT approaches. Corrections to such an operator can be written as nonminimal coupling terms. The power counting establishes inband and interband as leading and subleading order effects, respectively, in agreement with experimental observations. Electric quadrupole reduced transitions probabilities can be calculated from these transition operators. At each order, the theoretical uncertainty in the calculated $B(E2)$ values is adjusted in order to get a reduced χ^2 of one. In most cases, as will be discussed later, the adjusted theoretical uncertainty is in very good agreement with the naive estimate.

3.3.1 Toy model. Nonrigid rotor

In order to gain insight on how to couple an electromagnetic field to the DOF of the EFT, the following model is studied. Assume a particle with charge q and mass m is restricted to move in a spherical shell of thickness $\rho \ll R$ around $r \approx R$, due to a potential $V(r)$. The precise form of the potential is not relevant, as long as it confines the wave function of the system within the shell. A potential with

hard walls at $R \pm \rho/2$ fulfills this condition. The Hamiltonian for this system

$$\hat{H} = -\frac{\hbar^2}{2m}\Delta + V(r) \tag{3.53}$$

has states of the form

$$\begin{aligned} \langle r\theta\phi|NIM\rangle =& \psi(r,\theta,\phi) \\ =& \frac{u_N(r)}{r} Y_{IM}(\theta,\phi) \end{aligned} \tag{3.54}$$

due to the spherical symmetry of the problem.

Since the energy scale of rotations $E_{\text{rot}} \sim \hbar^2 I(I+1)/2mR^2$ is smaller than that of radial excitations $E_{\text{rad}} \sim \hbar^2/2m\rho^2$ for sufficiently small I, the spectrum consists of rotational bands on top of radial excitations, and the EFT for the nonrigid rotor can be employed to describe the low-energy physics of the system.

The Hamiltonian of the toy model can be minimally coupled to an electromagnetic field with vector potential $\mathbf{A}$ though the gauging

$$-i\hbar\nabla \to -i\hbar\nabla - q\mathbf{A}. \tag{3.55}$$

This procedure yields a Hamiltonian of the form $\hat{H}_{\text{EM}} = \hat{H} + \hat{H}^{(\mathbf{A})}$, where the interaction term is

$$\begin{aligned} \hat{H}^{(\mathbf{A})} =& i\frac{\hbar q}{2m}\left(\nabla\cdot\mathbf{A} + \mathbf{A}\cdot\nabla\right) \\ =& i\frac{\hbar q}{2m}\left(\frac{1}{r}\nabla_\Omega\cdot\mathbf{A} + \mathbf{A}\cdot\frac{1}{r}\nabla_\Omega + \mathbf{e}_r\partial_r\cdot\mathbf{A} + \mathbf{A}\cdot\mathbf{e}_r\partial_r\right). \end{aligned} \tag{3.56}$$

Here, the angular derivative in the tangent plane is given by

$$\nabla_\Omega = \mathbf{e}_\theta\partial_\theta + \mathbf{e}_\phi\frac{\partial_\phi}{\sin\theta}, \tag{3.57}$$

and terms of order $\mathcal{O}(q^2A^2)$ have been neglected since they represent suppressed two-photon processes.

If the wavelength λ of the electromagnetic field fulfills the long wavelength condition $\rho/\lambda \ll 1$, the rate of change of $\mathbf{A}$ with r is small within the shell where the wave functions are confined, and can be neglected. This condition is fulfilled by the nuclei we want to describe as will be discussed below. The matrix elements of this operator between an initial state $|i\rangle$ and a final state $|f\rangle$ within the same

rotational band are

$$\begin{aligned}\langle f|\hat{H}^{(\mathbf{A})}|i\rangle =& i\frac{\hbar q}{2m}\langle I_f M_f|\left(\nabla_\Omega\cdot\mathbf{A}+\mathbf{A}\cdot\nabla_\Omega\right)|I_i M_i\rangle\langle N|\frac{1}{r}|N\rangle \\ &+ i\frac{\hbar q}{m}\langle I_f M_f|\mathbf{A}\cdot\mathbf{e}_r|I_i M_i\rangle\langle N|\partial_r|N\rangle.\end{aligned} \tag{3.58}$$

The radial matrix elements in the last expression can be evaluated as follows. For $\rho \ll R$, the inverse of the distance is given by $r^{-1} = R^{-1} + \mathcal{O}(\rho/R)$. Then

$$\begin{aligned}\langle N|\frac{1}{r}|N\rangle =& \int_0^\infty dr\frac{u_N^2(r)}{r} \\ \approx& \frac{1}{R}\int_0^\infty dr\, u_N^2(r) \\ =& R^{-1}.\end{aligned} \tag{3.59}$$

Since the radial wave functions are confined within the shell of radius ρ at $r = R$, they vanish at the integration limits, that is, $u_N(0) = 0 = u_N(\infty)$. Thus,

$$\begin{aligned}\langle N|\partial_r|N\rangle =& \int_0^\infty dr\, r^2\frac{u_N(r)}{r}\partial_r\frac{u_N(r)}{r} \\ =& \int_0^\infty dr\left[u_N(r)u_N'(r)-\frac{u_N^2(r)}{r}\right] \\ \approx& \frac{u_N^2(r)}{2}\bigg|_0^\infty - \frac{1}{R}\int_0^\infty dr\, u_N^2(r) \\ =& -R^{-1}.\end{aligned} \tag{3.60}$$

Thus, in the long wavelength limit, the inband matrix elements of the interaction at LO in ρ/R take the form

$$\begin{aligned}\langle f|\hat{H}^{(\mathbf{A})}|i\rangle =& i\frac{\hbar q}{2mR}\langle I_f M_f|\left(\nabla_\Omega\cdot\mathbf{A}+\mathbf{A}\cdot\nabla_\Omega\right)|I_i M_i\rangle \\ &- i\frac{\hbar q}{mR}\langle I_f M_f|\mathbf{A}\cdot\mathbf{e}_r|I_i M_i\rangle.\end{aligned} \tag{3.61}$$

Notice that the commutator between the angular momentum operator squared

and a spherical harmonic is

$$\begin{aligned}\left[\hat{I}^2, Y_{IM}(\theta,\phi)\right] =& \hat{I}^2 Y_{IM}(\theta,\phi) + 2\sum_{\mu}(-1)^{\mu}\hat{I}_{\mu}Y_{IM}(\theta,\phi)\hat{I}_{-\mu} \\ =& I(I+1)Y_{IM}(\theta,\phi) + 2\sum_{\mu}(-1)^{\mu}\sqrt{I(I+1)}C^{IM+\mu}_{IM1\mu}Y_{IM+\mu}(\theta,\phi)\hat{I}_{-\mu} \\ =& I(I+1)Y_{IM}(\theta,\phi) + 2\sum_{\mu}\sqrt{I(I+1)}C^{IM}_{IM+\mu1-\mu}Y_{IM+\mu}(\theta,\phi)\hat{I}_{-\mu} \\ =& I(I+1)Y_{IM}(\theta,\phi) + 2\sqrt{I(I+1)}\left(Y_I \otimes \hat{\mathbf{I}}\right)_{IM},\end{aligned} \tag{3.62}$$

implying that

$$\left[\hat{I}^2, \mathbf{e}_r\right] = 2\mathbf{e}_r + i2\left(\mathbf{e}_r \times \hat{\mathbf{I}}\right). \tag{3.63}$$

The angular momentum operator may be written as

$$\hat{\mathbf{I}} = -i\mathbf{e}_r \times \nabla_{\Omega}. \tag{3.64}$$

Inserting Equation (3.64) into Equation (3.63) leads to

$$-i\nabla_{\Omega} = \frac{i}{2}\left[\hat{I}^2, \mathbf{e}_r\right] - i\mathbf{e}_r. \tag{3.65}$$

allowing for the LO inband interaction operator to be written as

$$\begin{aligned}\hat{H}^{(\mathbf{A})} =& -\frac{\hbar q}{2mR}\left[(-i\nabla_{\Omega} + i\mathbf{e}_r)\cdot\mathbf{A} + \mathbf{A}\cdot(-i\nabla_{\Omega} + i\mathbf{e}_r)\right] \\ =& -i\frac{\hbar q}{4mR}\left(\left[\hat{I}^2, \mathbf{e}_r\right]\cdot\mathbf{A} + \mathbf{A}\cdot\left[\hat{I}^2, \mathbf{e}_r\right]\right).\end{aligned} \tag{3.66}$$

Corrections to this operator and its matrix elements are of order $\mathcal{O}(\rho/R)$. In order to reach the final expression for this operator, the identity (3.65) was employed.

The matrix elements of the LO inband interaction (3.66) are independent of the functional form of the potential $V(r)$, and the radial factor of the wave functions $u_N(r)$ is not required for their calculation. The radial zero-point motion causes the contribution from $\mathbf{A}\cdot\mathbf{e}_r$. Referencing the radial component of $\mathbf{A}$, associated with radial excitations, is against the expectation for the low-energy inband interaction to lie in the tangent plane. However, if the vector potential is decomposed into its radial and tangential components

$$\mathbf{A} = A_r\mathbf{e}_r + \mathbf{A}_{\Omega}, \qquad \mathbf{A}_{\Omega} \equiv A_{\theta}\mathbf{e}_{\theta} + A_{\phi}\mathbf{e}_{\phi}, \tag{3.67}$$

it is possible to use the identity

$$-i\nabla_\Omega \cdot \mathbf{A} = -i\nabla_\Omega \cdot \mathbf{A}_\Omega - i2\mathbf{A} \cdot \mathbf{e}_r \tag{3.68}$$

to write the inband interaction operator (3.66) as

$$\hat{H}^{(\mathbf{A})} = i\frac{\hbar q}{2mR}\left(\nabla_\Omega \cdot \mathbf{A}_\Omega + \mathbf{A}_\Omega \cdot \nabla_\Omega\right), \tag{3.69}$$

in agreement with the before mentioned expectation. While the last form of the inband interaction operator involves objects in the tangent plane only, the appearance of the non-Hermitian operator $-i\nabla_\Omega$ makes the calculation of its matrix elements nontrivial. An equivalent expression involving Hermitian operators exclusively can be obtained if the expression for the angular momentum operator in Equation (3.64) is inserted into the inband interaction operator (3.69). This yields

$$\hat{H}^{(\mathbf{A})} = -\frac{\hbar q}{2mR}\left[\hat{\mathbf{I}} \cdot (\mathbf{e}_r \times \mathbf{A}_\Omega) + (\mathbf{e}_r \times \mathbf{A}_\Omega) \cdot \hat{\mathbf{I}}\right]. \tag{3.70}$$

The forms of the inband interaction operator in Equations (3.69) and (3.70) suggest that the coupling between the rotational DOF in the toy model and an electromagnetic field is achieved through the gauging

$$-i\nabla_\Omega \to -i\nabla_\Omega - q\mathbf{A}_\Omega, \qquad \hat{\mathbf{I}} \to \hat{\mathbf{I}} - q\mathbf{e}_r \times \mathbf{A}_\Omega. \tag{3.71}$$

3.3.2 Gauging the effective field theory for the ground band

Let us couple the rotational DOF in the EFT to an electromagnetic field. To do this, we start with the LO Hamiltonian (3.14), and require it to remain invariant under local gauge transformations of its wave functions $\psi(\Omega)$. Such transformations are given by

$$\psi(\theta, \phi) \to \exp\left[i\lambda(\theta, \phi)\right]\psi(\theta, \phi), \tag{3.72}$$

where $\lambda(\Omega)$ is a function of the orientation angles only. For this symmetry to hold, gauge fields must be introduced according to

$$-i\nabla_\Omega \to -i\nabla_\Omega - q\mathbf{A}_\Omega, \qquad \hat{\mathbf{I}} \to \hat{\mathbf{I}} - q\mathbf{e}_r \times \mathbf{A}_\Omega, \tag{3.73}$$

with $\mathbf{A}_\Omega \equiv -\nabla_\Omega \lambda(\Omega)$. Here, the effective charge q is a LEC and must be fit to data. Thus, requiring the EFT to be invariant under local gauge transformations of its wave functions introduces gauge fields that lie in the tangent plane.

Gauging the LO Hamiltonian (3.14) yields the LO EFT for a nonrigid rotor coupled to an electromagnetic field. The Hamiltonian is of the form $\hat{H}_{\mathrm{LO}} + \hat{H}_{\mathrm{LO}}^{(\mathbf{A})}$ with the LO interaction given by

$$\begin{aligned}\hat{H}_{\mathrm{LO}}^{(\mathbf{A})} =& -\frac{q}{2C_0}\left[\hat{\mathbf{I}}\cdot(\mathbf{e}_r\times\mathbf{A}_\Omega)+(\mathbf{e}_r\times\mathbf{A}_\Omega)\cdot\hat{\mathbf{I}}\right]\\ =& i\frac{q}{2C_0}\left(\nabla_\Omega\cdot\mathbf{A}_\Omega+\mathbf{A}_\Omega\cdot\nabla_\Omega\right),\end{aligned} \tag{3.74}$$

and terms of order $\mathcal{O}(q^2A^2)$ have been neglected. This LO interaction operator is equivalent to that of Equation (3.69). Thus, gauging the EFT yields the same inband interaction as the one obtained integrating out the radial DOF in the toy model, associated with high-energy excitations.

In order to facilitate the calculation of the matrix elements of the inband interaction, the identity (3.68) is employed to rewrite it as

$$\begin{aligned}\hat{H}_{\mathrm{LO}}^{(\mathbf{A})} =& -\frac{q}{2C_0}\left[(-i\nabla_\Omega+i\mathbf{e}_r)\cdot\mathbf{A}+\mathbf{A}\cdot(-i\nabla_\Omega+i\mathbf{e}_r)\right]\\ =& -i\frac{q}{4C_0}\left(\left[\hat{I}^2,\mathbf{e}_r\right]\cdot\mathbf{A}+\mathbf{A}\cdot\left[\hat{I}^2,\mathbf{e}_r\right]\right)\\ =& -i\frac{q}{2}\left(\left[\hat{H}_{\mathrm{LO}},\mathbf{e}_r\right]\cdot\mathbf{A}+\mathbf{A}\cdot\left[\hat{H}_{\mathrm{LO}},\mathbf{e}_r\right]\right).\end{aligned} \tag{3.75}$$

This expression for the inband interaction operator is particularly useful when calculating its matrix elements.

If the NLO correction to the Hamiltonian (3.19) is minimally coupled to an electromagnetic field via the gauging in Equation (3.73), and terms of order $\mathcal{O}(q^2A^2)$ or higher are neglected, a contribution of the form $\hat{H}_{\mathrm{NLO}} + \hat{H}_{\mathrm{NLO}}^{(\mathbf{A})}$ arises. Here, the coupling term is

$$\begin{aligned}\hat{H}_{\mathrm{NLO}}^{(\mathbf{A})} =& \frac{qC_2}{4C_0^4}\left\{\hat{I}^2\left[\hat{\mathbf{I}}\cdot(\mathbf{e}_r\times\mathbf{A})+(\mathbf{e}_r\times\mathbf{A})\cdot\hat{\mathbf{I}}\right]+\left[\hat{\mathbf{I}}\cdot(\mathbf{e}_r\times\mathbf{A})+(\mathbf{e}_r\times\mathbf{A})\cdot\hat{\mathbf{I}}\right]\hat{I}^2\right\}\\ =& -\frac{C_2}{2C_0^3}\left[\hat{I}^2\hat{H}_{\mathrm{LO}}^{(\mathbf{A})}+\hat{H}_{\mathrm{LO}}^{(\mathbf{A})}\hat{I}^2\right].\end{aligned} \tag{3.76}$$

Notice that the LECs in this coupling term appear in the NLO correction to the Hamiltonian (3.19) and the LO interaction (3.75). Thus, once the LECs of the those terms are fitted to data, the NLO correction to the inband interaction (3.76) is completely determined.

Let us employ a plane wave vector potential $\mathbf{A} = A\mathbf{e}_z e^{i(kx-wt)}$ and a multipole

expansion to describe electromagnetic transitions with different multipolarities. This expansion is valid when the wavelength of the radiation λ is larger than the linear dimension of the system R. If k is the wavenumber of the electromagnetic field, this quantity scales as $k \sim \xi$ for inband transitions. Also, if m is the mass of the nonrigid rotor, then $mR^2 \sim C_0 \sim \xi^{-1}$ and $R \sim 1/\sqrt{m\xi}$. Thus, we expect $kR \sim \sqrt{\xi/m}$. In rare earth nuclei $kR \sim 1/300$, and the multipole expansion converges rapidly.

When the quadrupole component of the vector potential

$$\mathbf{A}^{(2)} = Akr \sin\theta \cos\phi \mathbf{e}_z \tag{3.77}$$

is inserted into the LO inband interaction (3.75), it yields the LO component of the quadrupole inband interaction. The subleading contribution to the dipole inband interaction will be neglected in what follows. The LO inband quadrupole interaction is

$$\begin{aligned}
\hat{H}^{(\mathbf{A})}_{\mathrm{LO}} =& -i\frac{q}{2}\left(\left[\hat{H}_{\mathrm{LO}}, \mathbf{e}_r\right] \cdot \mathbf{A}^{(2)} + \mathbf{A}^{(2)} \cdot \left[\hat{H}_{\mathrm{LO}}, \mathbf{e}_r\right]\right) \\
=& -i\frac{q}{2}\left[\hat{H}_{\mathrm{LO}}, \mathbf{A}^{(2)} \cdot \mathbf{e}_r\right] + i\frac{q}{4C_0}\left(\mathbf{e}_r \cdot \hat{I}^2 \mathbf{A}^{(2)} - \mathbf{A}^{(2)} \cdot \hat{I}^2 \mathbf{e}_r\right) \\
=& -i\frac{q}{2} w \mathbf{A}^{(2)} \cdot \mathbf{e}_r + i\frac{q}{4C_0}\left(\mathbf{e}_r \cdot \hat{I}^2 \mathbf{A}^{(2)} - \mathbf{A}^{(2)} \cdot \hat{I}^2 \mathbf{e}_r\right).
\end{aligned} \tag{3.78}$$

Here $w \equiv E_f - E_i$ is the difference between the LO energies of the final and initial states. The absolute value of this energy difference is the energy of the photon involved in the transition.

The matrix elements of $\mathbf{A}^{(2)} \cdot \mathbf{e}_r$ between the initial state $|i\rangle$ and the final state $|f\rangle$ are

$$\begin{aligned}
\langle f|\mathbf{A}^{(2)} \cdot \mathbf{e}_r|i\rangle =& AkR\langle f|\sin\theta\cos\phi\cos\theta|i\rangle \\
=& AkR\sqrt{\frac{8\pi^2}{9}}\langle f|(Y_{1-1} - Y_{11})Y_{10}|i\rangle \\
=& AkR\sum_I \sqrt{\frac{2\pi}{2I+1}} C^{I0}_{1010}\langle f|\left(C^{I-1}_{1-110}Y_{I-1} - C^{I1}_{1110}Y_{I1}\right)|i\rangle,
\end{aligned} \tag{3.79}$$

where the value of the vector potential at $r = R$ was employed and the product of two spherical harmonics was expanded in a Clebsch-Gordan series [50]

$$Y_{I_1M_1}Y_{I_2M_2} = \sum_I \sqrt{\frac{(2I_1+1)(2I_2+1)}{4\pi(2I+1)}} C^{I0}_{I_10I_20} C^{IM}_{I_1M_1I_2M_2} Y_{IM}, \tag{3.80}$$

with $|I_1 - I_2| \leq I \leq I_1 + I_2$ and $M = M_1 + M_2$. Since the spherical harmonics are not defined for $|M| \geq I$, the term with $I = 0$ do not contribute to the matrix elements (3.79). Also, because of the symmetry properties of the Clebsch-Gordan coefficients [50], the term with $I = 1$ vanishes. From here, the matrix elements (3.79) take the form

$$\begin{aligned}\langle f|\mathbf{A}^{(2)} \cdot \mathbf{e}_r|i\rangle =& AkR\sqrt{\frac{2\pi}{15}}\langle f|(Y_{2-1} - Y_{21})|i\rangle \\ =& AkR\sqrt{\frac{2I_i+1}{6(2I_f+1)}}C^{I_f 0}_{I_i 020}\left(C^{I_f M_f}_{I_i M_i 2-1} - C^{I_f M_f}_{I_i M_i 21}\right).\end{aligned} \tag{3.81}$$

In order to facilitate the calculation of the matrix elements of $\mathbf{A}^{(2)} \cdot \hat{I}^2\mathbf{e}_r$, we employ the identity operator

$$\hat{\mathbb{I}} = \sum_{\mathcal{I}} |\mathcal{I}\rangle\langle\mathcal{I}|. \tag{3.82}$$

The mentioned matrix elements take the form

$$\begin{aligned}\langle f|\mathbf{A}^{(2)} \cdot \hat{I}^2\mathbf{e}_r|i\rangle =& AkR\sqrt{\frac{8\pi^2}{9}}\langle f|(Y_{1-1} - Y_{11})\hat{I}^2 Y_{10}|i\rangle \\ =& AkR\sqrt{\frac{8\pi^2}{9}}\sum_{\mathcal{I}}\langle f|(Y_{1-1} - Y_{11})\hat{I}^2|\mathcal{I}\rangle\langle\mathcal{I}|Y_{10}|i\rangle \\ =& AkR\sqrt{\frac{2I_i+1}{2(2I_f+1)}}C^{I_f 0}_{I010}\left(C^{I_f M_f}_{IM_i 1-1} - C^{I_f M_f}_{IM_i 11}\right)C^{I0}_{I_i 010}C^{IM_i}_{I_i M_i 10}I(I+1).\end{aligned} \tag{3.83}$$

The symmetry properties of the Clebsch-Gordan coefficients impose the conditions $I_f + 1 = I = I_i - 1$ and $I_f - 1 = I = I_i + 1$ for decays and excitations, respectively. In both cases, the explicit form of the Clebsch-Gordan coefficients [50] allows us to reach the following expressions for the matrix elements (3.83)

$$\langle f|\mathbf{A}^{(2)} \cdot \hat{I}^2\mathbf{e}_r|i\rangle = AkR\sqrt{\frac{2I_i+1}{6(2I_f+1)}}C^{I_f 0}_{I_i 020}\left(C^{I_f M_f}_{I_i M_i 2-1} - C^{I_f M_f}_{I_i M_i 21}\right)I(I+1). \tag{3.84}$$

Finally, for the matrix elements of $\mathbf{e}_r \cdot \hat{I}^2\mathbf{A}^{(2)}$ one finds

$$\langle f|\mathbf{e}_r \cdot \hat{I}^2\mathbf{A}^{(2)}|i\rangle = \left(\langle i|\mathbf{A}^{(2)} \cdot \hat{I}^2\mathbf{e}_r|f\rangle\right)^*. \tag{3.85}$$

Working out these matrix elements similarly to those of $\mathbf{A}^{(2)} \cdot \hat{I}^2\mathbf{e}_r$ leads to

$$\langle f|\mathbf{e}_r \cdot \hat{I}^2\mathbf{A}^{(2)}|i\rangle = \langle f|\mathbf{A}^{(2)} \cdot \hat{I}^2\mathbf{e}_r|i\rangle. \tag{3.86}$$

Let the matrix elements of the LO inband interaction be denoted by

$$M_{\mathrm{LO}}(i \to f) \equiv \langle f|\hat{H}^{(\mathbf{A})}_{\mathrm{LO}}|i\rangle. \tag{3.87}$$

The matrix elements of the NLO correction take the form

$$\begin{aligned} M_{\mathrm{NLO}}(i \to f) \equiv & \langle f|\hat{H}^{(\mathbf{A})}_{\mathrm{NLO}}|i\rangle \\ = & -\frac{C_2}{2C_0^3}\left[I_f(I_f+1)+I_i(I_i+1)\right] M_{\mathrm{LO}}(i \to f). \end{aligned} \tag{3.88}$$

The matrix elements (3.81), (3.84) and (3.86) are employed to calculate the matrix elements of the LO inband quadrupole interaction. They are given by

$$\begin{aligned} M_{\mathrm{LO}}(E2, i \to f) \equiv & -i\frac{q}{2} w \langle f|\mathbf{A}^{(2)} \cdot \mathbf{e}_r|i\rangle \\ = & -i\frac{qAkR}{2} w \sqrt{\frac{2I_i+1}{6(2I_f+1)}} C^{I_f 0}_{I_i 020}\left(C^{I_f M_f}_{I_i M_i 2-1} - C^{I_f M_f}_{I_i M_i 21}\right) \end{aligned} \tag{3.89}$$

The corresponding matrix elements of the NLO correction to the inband quadrupole interaction can be obtained by inserting the matrix elements (3.89) into Equation (3.88). Then, the matrix elements of the inband quadrupole interaction at NLO are analogous to those of Equation (3.89) with w being the difference between the NLO energies of the final and initial states. In what follows the factor kR is absorbed into the effective charge by redefining $qkR \to q$.

3.3.3 Nonminimal couplings and corrections to the inband operator

Nonminimal couplings, that is, interaction terms that couple the rotational DOF to either the electric or magnetic field, arise because the DOF in terms of which the EFT is written describe composite objects. Such terms are gauge-invariant, and must be consistent with the symmetries of the systems.

Terms coupling the rotational DOF to the electric field $\mathbf{E}$ describe electric interactions. The power counting for these terms is in derivatives on the electric field and number of times the rotational "fields" appear. The lowest order nonminimal interaction involving the electric field is

$$\hat{H}^{(\mathbf{E})}_{\mathrm{LO}} \equiv d_0 \mathbf{E} \cdot \mathbf{e}_r. \tag{3.90}$$

Here, the dimensionless LEC d_0 must be fit to data. Notice that, if we assume it is of natural size, $\mathbf{E} \sim \xi \mathbf{A}$ for low-energy interactions. Thus, the LO nonminimal

interaction involving $\mathbf{E}$ is of the same order as as the LO inband interaction (3.75). If we employ the plane wave vector potential introduced in the previous section, the quadrupole component of the electric field is given by

$$\mathbf{E}^{(2)} = iw\mathbf{A}^{(2)}, \tag{3.91}$$

and the matrix elements of the LO nonminimal quadrupole interaction (3.91) are equivalent to those of the LO inband quadrupole interaction (3.89) after identifying the LECs $d_0 = q/2$. Thus, the application of Siegert's theorem, which states that the current density operator can be replaced with the charge density operator in order to facilitate the calculation of its matrix elements (since a vector operator is replaced by a scalar operator), is valid for the LO electric interactions, as expected. A detailed discussion on the derivation of Siegert's theorem is given in Ref. [121].

Let us now turn to higher-order nonminimal interactions. In principle, every single term involving the electric or magnetic field that is invariant under rotations, parity and time reversal must be considered by the EFT. However, the power counting allows us to establish which terms must be considered at each order. Since the building blocks for the nonminimal coupling interactions are operators, the order in which they are coupled is relevant. Thus, the following terms that are linear in $\hat{\mathbf{I}}$ are allowed within the EFT

$$\begin{aligned} i\left(\mathbf{e}_r \times \hat{\mathbf{I}}\right)\cdot\mathbf{E} + \text{h.c.} &= -\mathbf{e}_r\cdot\mathbf{E} + \frac{1}{2}\left[\hat{I}^2, \mathbf{e}_r\right]\cdot\mathbf{E} + \text{h.c.} \\ &= -2\mathbf{e}_r\cdot\mathbf{E} + \frac{1}{2}\left\{\hat{I}^2\mathbf{e}_r\cdot\mathbf{E} + \mathbf{e}_r\cdot\mathbf{E}\hat{I}^2\right\} - \frac{1}{2}\left\{\mathbf{e}_r\cdot\hat{I}^2\mathbf{E} + \mathbf{E}\cdot\hat{I}^2\mathbf{e}_r\right\} \end{aligned} \tag{3.92}$$

and

$$\begin{aligned} i\mathbf{E}\cdot\left(\mathbf{e}_r \times \hat{\mathbf{I}}\right) + \text{h.c.} &= -\mathbf{e}_r\cdot\mathbf{E} + \frac{1}{2}\mathbf{E}\cdot\left[\hat{I}^2, \mathbf{e}_r\right] + \text{h.c.} \\ &= -2\mathbf{e}_r\cdot\mathbf{E} - \frac{1}{2}\left\{\hat{I}^2\mathbf{e}_r\cdot\mathbf{E} + \mathbf{e}_r\cdot\mathbf{E}\hat{I}^2\right\} + \frac{1}{2}\left\{\mathbf{e}_r\cdot\hat{I}^2\mathbf{E} + \mathbf{E}\cdot\hat{I}^2\mathbf{e}_r\right\}, \end{aligned} \tag{3.93}$$

where h.c. stands for Hermitian conjugate. Thus, any operator linear in $\hat{\mathbf{I}}$ can be written as a linear combination of the LO nonminimal interaction, and terms quadratic in $\hat{\mathbf{I}}$.

To find all the relevant nonminimal interactions quadratic in $\hat{\mathbf{I}}$, the following

identities were employed

$$\left[\hat{I}^2, f(\Omega)\right] = \hat{I}^2 f(\Omega) + 2\sum_i \hat{I}_i f(\Omega)\hat{I}_i \tag{3.94}$$

and

$$\begin{aligned}\hat{\mathbf{I}}\cdot f(\Omega)\hat{\mathbf{I}} =& \sum_i \hat{I}_i f(\Omega)\hat{I}_i + f(\Omega)\hat{I}^2 \\ =& \frac{1}{2}\left[\hat{I}^2, f(\Omega)\right] - \frac{1}{2}\hat{I}^2 f(\Omega) + f(\Omega)\hat{I}^2 \\ =& \frac{1}{2}\left\{\hat{I}^2, f(\Omega)\right\} - \frac{1}{2}\hat{I}^2 f(\Omega).\end{aligned} \tag{3.95}$$

Here $\hat{I}_i$ are the Cartesian components of the angular momentum operator, and the anticommutator of two operators $\hat{A}$ and $\hat{B}$ is defined by $\{\hat{A}, \hat{B}\} = \hat{A}\hat{B} + \hat{B}\hat{A}$. Besides the terms quadratic in $\hat{\mathbf{I}}$ in Equations (3.92) and (3.93), the EFT allows the following nonminimal interactions quadratic in $\hat{\mathbf{I}}$

$$\begin{aligned}\hat{I}_i(\mathbf{e}_r)_j\hat{I}_i E_j + \text{h.c.} =& -\mathbf{e}_r\cdot\mathbf{E} + \frac{1}{2}\left\{\hat{I}^2, \mathbf{e}_r\right\}\cdot\mathbf{E} + \text{h.c.} \\ =& -2\mathbf{e}_r\cdot\mathbf{E} + \frac{1}{2}\left\{\hat{I}^2\mathbf{e}_r\cdot\mathbf{E} + \mathbf{e}_r\cdot\mathbf{E}\hat{I}^2\right\} + \frac{1}{2}\left\{\mathbf{e}_r\cdot\hat{I}^2\mathbf{E} + \mathbf{E}\cdot\hat{I}^2\mathbf{e}_r\right\}\end{aligned} \tag{3.96}$$

$$\begin{aligned}(\mathbf{e}_r)_i\hat{I}_j E_i\hat{I}_j + \text{h.c.} =& -\frac{1}{2}\mathbf{e}_r\cdot\left(\hat{I}^2\mathbf{E}\right) + \frac{1}{2}\mathbf{e}_r\cdot\left\{\hat{I}^2, \mathbf{E}\right\} + \text{h.c.} \\ =& -\mathbf{e}_r\cdot\left(\hat{I}^2\mathbf{E}\right) + \frac{1}{2}\left\{\hat{I}^2\mathbf{e}_r\cdot\mathbf{E} + \mathbf{e}_r\cdot\mathbf{E}\hat{I}^2\right\} + \frac{1}{2}\left\{\mathbf{e}_r\cdot\hat{I}^2\mathbf{E} + \mathbf{E}\cdot\hat{I}^2\mathbf{e}_r\right\}\end{aligned} \tag{3.97}$$

and

$$\hat{I}_i\left(\mathbf{e}_r\cdot\mathbf{E}\right)\hat{I}_i = \frac{1}{2}\left\{\hat{I}^2\mathbf{e}_r\cdot\mathbf{E} + \mathbf{e}_r\cdot\mathbf{E}\hat{I}^2\right\} - \frac{1}{2}\hat{I}^2\left(\mathbf{e}_r\cdot\mathbf{E}\right). \tag{3.98}$$

Thus, all relevant non-minimal interactions at NLO are quadratic in $\hat{\mathbf{I}}$. There are only two linearly independent terms. From here, the NLO nonminimal interaction is written as the linear combination

$$\hat{H}^{(\mathbf{E})}_{\text{NLO}} = -\frac{qd_1}{4}\left(\hat{I}^2\mathbf{E}\cdot\mathbf{e}_r + \mathbf{E}\cdot\mathbf{e}_r\hat{I}^2\right) - \frac{qd_2}{4}\left(\mathbf{e}_r\cdot\hat{I}^2\mathbf{E} + \mathbf{E}\cdot\hat{I}^2\mathbf{e}_r\right), \tag{3.99}$$

where d_1 and d_2 are LECs that must be fit to data, and the factor $q/4$ have been included for convenience. If the quadrupole component of the electric field $\mathbf{E}^{(2)}$ is inserted into the nonminimal interaction, its matrix elements become

$$\langle f|\hat{H}^{(\mathbf{E})}_{\text{NLO}}|i\rangle = M_{\text{LO}}(E2, i\to f)\times\left[d_1\frac{I_f(I_f+1) + I_i(I_i+1)}{2} + d_2 I(I+1)\right], \tag{3.100}$$

where $I_f + 1 = I = I_i - 1$ and $I_f - 1 = I = I_i + 1$ for decays and excitations, respectively.

As a NLO correction, it is expected to fulfill a relation similar to that for the ratio of the NLO correction to the LO contribution for the energies in Equation (3.22)

$$\frac{\langle f|\hat{H}^{(\mathbf{E})}_{\mathrm{NLO}}|i\rangle}{\langle f|\hat{H}^{(\mathbf{E})}_{\mathrm{LO}}|i\rangle} \sim \frac{\langle f|\hat{H}^{(\mathbf{E})}_{\mathrm{NLO}}|i\rangle}{\langle f|\hat{H}^{(\mathbf{A})}_{\mathrm{LO}}|i\rangle} \sim \left(\frac{\xi}{\omega}\right)^2 f(I_i, I_f), \tag{3.101}$$

where $f(I_i, I_f)$ is a function of the angular momenta of the initial and final states involved in the transitions. From this ratio, it is expected that the LECs in these corrections scale as

$$d_1 \sim d_2 \sim (\xi/\omega)^2. \tag{3.102}$$

In this work, we study only $E2$ transitions. In order to study magnetic dipole transitions, expected to be similar in strength to the studied electric transitions, other nonminimal interactions involving the magnetic field $\mathbf{B}$ must be included in the EFT.

3.3.4 Inband quadrupole transition moments

The inband transition operator at NLO in the EFT is defined as

$$\hat{\mathscr{M}}(E\lambda) \equiv \frac{\hat{H}^{(\mathbf{A})}_{\mathrm{NLO}} + \hat{H}^{(\mathbf{E})}_{\mathrm{NLO}}}{wA}, \tag{3.103}$$

where the multipolarity of the transition induced by it depends on which multipole components of the fields $\mathbf{A}$ and $\mathbf{E}$ are employed for the calculation of its matrix elements, and the factor A renders such calculation independent of the intensity of the vector potential. According to Fermi's golden rule, the reduced transition probabilities of multipolarity λ or $B(E\lambda)$ values for are given by

$$B(E\lambda, i \to f) = \frac{1}{2I_i + 1}\left|\langle f||\hat{\mathscr{M}}(E\lambda)||i\rangle\right|^2. \tag{3.104}$$

Thus, the $B(E2)$ values for decays within the ground band at NLO are

$$B(E\lambda, i \to f) = \frac{(aq)^2}{60}\left(C^{I_f 0}_{I_i 020}\right)^2\left[1 + \frac{b}{a}I_i(I_i+1)\right], \tag{3.105}$$

where $a \equiv 1 + d_1$ and $b \equiv 2(d_1 + d_2)$, and only terms linear in the LECs d_1 and d_2 were kept.

To understand the transition strengths within the EFT for the ground band, it is very useful to remove the trivial dependence in the angular momenta of the initial and final states involved in the transition, contained in the Clebsch-Gordan coefficient. For this reason we define the $E2$ transition moments Q_{if} as

$$Q_{if}^2 \equiv \frac{B(E2, i \to f)}{\left(C_{I_i 020}^{I_f 0}\right)^2}. \tag{3.106}$$

The $E2$ transition moments for decays within the ground band are given by

$$\begin{aligned} Q_{if}^2 =& \frac{(aqR)^2}{60}\left[1 + \frac{b}{a} I_i(I_i - 1)\right] \\ =& Q_0^2 \left[1 + \frac{b}{a} I_i(I_i - 1)\right], \end{aligned} \tag{3.107}$$

where $Q_0 \equiv \sqrt{(aqR)^2/60}$ may be thought of as the effective quadrupole moment of the system.

Thus, at LO, the EFT for the ground band predicts constant quadrupole transition moments, consistent with the expectation for a rigid rotor. The NLO correction accounts for deviations from this behavior, which are quadratic in the angular momentum of the initial state. Notice that the NLO correction to the $E2$ transition moments are similar in size and functional form to the NLO correction of the energy spectrum of the ground band.

3.3.5 Gauging the effective field theory for the nonrigid rotor

In order to couple the EFT for the nonrigid rotor to an electromagnetic field the following gauging was used

$$-i\nabla_{\Omega\gamma} \to -i\nabla_{\Omega\gamma} - q\mathbf{A}_\Omega, \qquad \hat{\mathbf{J}} \to \hat{\mathbf{J}} - q\mathbf{e}_r \times \mathbf{A}_\Omega. \tag{3.108}$$

It is analogous to that used to gauge the EFT for the ground band (3.73). In the last expression

$$\begin{aligned} -i\nabla_{\Omega\gamma} \equiv& \hat{\mathbf{p}}_{\Omega\gamma} \\ =& -\mathbf{e}_r \times \hat{\mathbf{J}} \\ =& -i\mathbf{e}_\theta \partial_\theta - i\mathbf{e}_\phi \frac{\partial_\phi - \partial_\gamma \cos\theta}{\sin\theta}. \end{aligned} \tag{3.109}$$

Thus, the Euler angles θ, ϕ, and γ are gauged. If it is assumed that the vibrational DOF ψ_0 and ψ_2 also carry a charge, it would be possible to construct rotationally invariant terms coupling these DOF to the radial component of the vector potential $\mathbf{A}$ (such coupling is consistent with the expectation of high-energy transitions to reference the radial component of the electromagnetic field). As will be discussed below, these interactions do not yield independent contributions to interband transitions. Therefore, they are neglected.

Gauging the NLO contribution in the Hamiltonian (3.44) yields the LO inband interaction

$$\begin{aligned}\hat{H}_{\mathrm{NLO}} =& -\frac{q}{2C_0}\left[\hat{\mathbf{J}}\cdot(\mathbf{e}_r\times\mathbf{A}_\Omega)+(\mathbf{e}_r\times\mathbf{A}_\Omega)\cdot\hat{\mathbf{J}}\right]\\ =& i\frac{q}{2C_0}\left(\nabla_{\Omega\gamma}\cdot\mathbf{A}_\Omega+\mathbf{A}_\Omega\cdot\nabla_{\Omega\gamma}\right)\\ =& -i\frac{q}{4C_0}\left(\left[\hat{J}^2,\mathbf{e}_r\right]\cdot\mathbf{A}+\mathbf{A}\cdot\left[\hat{J}^2,\mathbf{e}_r\right]\right),\end{aligned} \tag{3.110}$$

analogous to the inband interaction of the EFT for the ground band (3.74). The identity

$$-i\nabla_{\Omega\gamma}=\frac{i}{2}\left[\hat{J}^2,\mathbf{e}_r\right]-i\mathbf{e}_r \tag{3.111}$$

was employed to reach the final form of the LO inband interaction (3.110). When the quadrupole component of the vector potential is inserted into this interaction, its matrix elements between states in a band with quantum number $K=0$ are equivalent to those in Equation (3.89).

Gauging the NNLO contribution in the Hamiltonian (3.51) yields the LO interband interaction operator

$$\begin{aligned}\hat{H}^{(\mathbf{A})}_{\mathrm{NNLO}} =& i\frac{q}{2C_0}\frac{C_\beta}{C_0}\psi_0\left(\nabla_{\Omega\gamma}\cdot\mathbf{A}_\Omega+\mathbf{A}_\Omega\cdot\nabla_{\Omega\gamma}\right)\\ &+i\frac{q}{2C_0}\frac{C_\gamma}{C_0}\psi_2\left(\nabla^T_{\Omega\gamma}\hat{\Gamma}\mathbf{A}_\Omega+\mathbf{A}_\Omega\hat{\Gamma}\nabla_{\Omega\gamma}\right).\end{aligned} \tag{3.112}$$

The first and second terms in the LO interband interaction describe interactions between states in different bands fulfilling the conditions $\Delta n_0=\pm1$ and $\Delta n_2=\pm1$, respectively. Thus, the first and second terms of the interband interaction couple states in the β and γ bands to states in the ground band, respectively. As the interband interactions originate from a higher-order term in the Hamiltonian than the inband interaction, the former is expected to be an order of magnitude weaker than the later.

The calculation of the matrix elements interband interaction (3.112) required to compute the quadrupole reduced transition probabilities for decays from the β or γ bands to the ground band is tedious. In Appendix C the corresponding calculation is presented in detail.

Finally, gauging the vibrational DOF ψ_0 and ψ_2 would add terms of the form $q_0\mathbf{A}\cdot\mathbf{e}_r\hat{p}_0$ + h.c. and $q_2\mathbf{A}\cdot\mathbf{e}_r\hat{p}_2$ + h.c. to the Hamiltonian. The first of these operators yields transition matrix elements that do not differ from those of the operator (3.112). The matrix elements of the second one vanish. They are therefore neglected.

3.3.6 Interband quadrupole transition moments

The $B(E\lambda)$ values for transitions within the EFT for the nonrigid rotor are given by Fermi's golden rule

$$B(E\lambda, i\to f)=\frac{1}{2I_i+1}\left|\langle f||\hat{\mathscr{M}}(E\lambda)||i\rangle\right|^2. \tag{3.113}$$

where the transition operator is defined by

$$\hat{\mathscr{M}}(E\lambda)\equiv\frac{\hat{H}^{(\mathbf{A})}_{\rm NLO}+\hat{H}^{(\mathbf{A})}_{\rm NNLO}}{wA}, \tag{3.114}$$

with $w\equiv[I_f(I_f+1)-I_i(I_i+1)+K_i^2]/2C_0$, and where the multipolarity of the operator is defined by which component of the field $\mathbf{A}$ is employed.

The LO interband $B(E2)$ values for transitions from the β and γ bands to the ground band are

$$B(E2, i_\beta\to f_g)=\frac{1}{2\omega_0}\left(\frac{C_\beta}{C_0}\right)^2\frac{q^2}{60}\left(C^{I_f0}_{I_i020}\right)^2 \tag{3.115}$$

and

$$B(E2, i_\gamma\to f_g)=\frac{3}{2\omega_2}\left(\frac{C_\gamma}{C_0}\right)^2\frac{q^2}{60}\left(C^{I_f0}_{I_i22-2}\right)^2. \tag{3.116}$$

The definition of the $E2$ transition moments can be generalized to

$$Q^2_{if}\equiv\frac{B(E2, i\to f)}{\left(C^{I_fK_f}_{I_iK_i2K_f-K_i}\right)^2}, \tag{3.117}$$

thus taking into account interband transitions. Then

$$Q^2_{i_\beta f_g} = \frac{1}{2\omega_0}\left(\frac{C_\beta}{C_0}\right)^2 Q^2, \qquad Q^2_{i_\gamma f_g} = \frac{3}{2\omega_2}\left(\frac{C_\gamma}{C_0}\right)^2 Q^2, \tag{3.118}$$

where $Q \equiv \sqrt{q^2/60}$ is the effective quadrupole moment. Thus, the strengths of transitions from the γ band are expected to be larger than those of transitions from the β band for LECs C_β and C_γ of similar size.

Notice that the reduced transition probabilities of interband transitions depend on the LECs C_β and C_γ. Recall that these LECs enter the Hamiltonian at NNLO, and correct the energies at N^{3}LO. Since many other LECs enters at that order, it is convenient to fix the values of C_β and C_γ in order to reproduce a $B(E2)$ value for a decay from the β and γ band, respectively. All other interband transitions are predictions within the EFT.

In the collective models, the strength of decays from the β or γ bands is completely determined by the energy of the bandhead ω_0 or ω_2, respectively. As a result, these faint transitions are overpredicted, some times by an order of magnitude (see, e.g., Ref. [25]). Within the adiabatic Bohr model, the transition strengths for decays from such bands are

$$\begin{aligned} B(E2, i_\beta \to f_g) =& \frac{\xi}{2\omega_0}\left(\frac{Ze\beta_0}{A}\right)^2 \left(C^{l_f 0}_{l_i 020}\right)^2, \\ B(E2, i_\gamma \to f_g) =& \frac{2\xi}{\omega_2}\left(\frac{Ze\beta_0}{A}\right)^2 \left(C^{l_f 0}_{l_i 22-2}\right)^2. \end{aligned} \tag{3.119}$$

From these expressions (written in terms of the LEC ω_2, which is two times larger than the constant ω_2 employed in the collective model) implies that interband transitions from the β band are only a factor two weaker than those from the γ band. Here, β_0 is a deformation parameter. The EFT results (3.115) and (3.116) are richer in structure than those of the collective models. This structure comes from a theory based on symmetry principles only, and allows for the precise description of interband transitions. It is worth mentioning that the ratios of $B(E2)$ values within the EFT are equivalent to those of the collective models at LO.

3.3.7 Transition probability uncertainty estimation

In order to estimate the theoretical uncertainty in calculated inband $B(E2)$ values, we follow the procedure discussed in Section 3.1.3. First, the quadrupole transition moments for decays within the ground band are written as an effective expansion

in powers of the parameter $Q \equiv (C_2/C_0^3) I_i (I_i - 1)$

$$Q_{if} = Q_0^2 + Q_0^2 \sum_i \mathscr{D}_i Q^i, \tag{3.120}$$

with $i \geq 1$, and where the expansion coefficients $\mathscr{D}_i$ are expected to be of order one. From Equation (3.107), the identification $b/a = \mathscr{D}_1 (C_2/C_0^3)$ can be make.

Next, the theoretical uncertainty at order k is written as $\sigma_{\text{th}}^{(k)} = \alpha^{(k)} Q^{k+1}$, where $\alpha^{(k)}$ is expected to be of order one, and perform χ^2 fits

$$\chi^2 = \sum_d \left[\frac{B(E2)_{\text{exp}}(d) - B(E2)_{\text{th}}^{(k)}(d)}{\sigma^{(k)}(d)} \right]^2 \tag{3.121}$$

varying the uncertainty parameter, until a reduced χ^2 of one is obtained. In equation (3.121), the sum is over all data points, $B(E2)_{\text{exp}}(d)$ and $B(E2)_{\text{th}}^{(k)}(d)$ are the experimental $B(E2)$ values and the theoretical $B(E2)$ values at order k, respectively, and $\sigma^{(k)}$ is the square root of the sum of the squares of the experimental and theoretical uncertainties at order k.

3.4 Comparison to data

In this Section, we compare the EFT against experimental data on $E2$ reduced transition probabilities. First, transitions within the ground state band of systems with a behavior close to that of a rigid rotor are studied. A rigid rotor is characterized by the energy ratios

$$R_{4/2} = 10/3, \qquad \xi/\omega = 0. \tag{3.122}$$

Molecules are a perfect starting point to test the EFT due to the large separation of scales between rotations and higher-energy modes. After a brief introduction, rotational nuclei in the rare earth and actinide regions are considered. These systems exhibit the largest separation of scales between rotations and vibrations in atomic nuclei. Finally, transitional nuclei for which the separation of scales is smaller, making NLO corrections appreciable even at low energies, are studied within the EFT.

The rotors against which the EFT was compared are listed in Table 3.1 along with the energy ratios of Equation (3.122). These ratios were employed to classify the systems into rotational and transitional systems. The values of the LECs C_0

Table 3.1: Energy ratios $R_{4/2}$ and ξ/ω, and dimensionless ratios of the LECs and the naive estimate for their scales for the systems studied in this work. The ratio ξ/ω measures the energy scales of rotations and vibrations.

Rotor	$R_{4/2}$	ξ/ω	$C_0\xi$	$(C_2/C_0)\omega^2$	$(\xi/\omega)^2$	C_2/C_0^3
N_2	3.33	0.005	3.00	2.1	0.000026	0.000006
H_2	3.30	0.08	2.99	2.2	0.0062	0.0015
^{236}U	3.30	0.05	2.99	2.3	0.0043	0.0011
^{174}Yb	3.31	0.05	2.99	3.4	0.0026	0.0010
^{168}Er	3.31	0.10	2.99	1.0	0.0094	0.0010
^{166}Er	3.29	0.10	2.98	1.6	0.011	0.0020
^{162}Dy	3.29	0.09	2.98	1.9	0.0083	0.0017
^{154}Sm	3.25	0.07	2.97	5.2	0.0056	0.0033
^{188}Os	3.08	0.24	2.91	1.5	0.06	0.012
^{154}Gd	3.01	0.18	2.88	3.3	0.033	0.013
^{152}Sm	3.01	0.18	2.88	3.5	0.032	0.013
^{150}Nd	2.93	0.19	2.85	3.6	0.037	0.017

and C_2 are compared against the naive estimate for their scales in columns three and four of Table 3.1. These LECs were calculated from the energies of the 2^+ and 4^+ states in the ground band. For a rigid rotor the dimensionless ratios $C_0\xi = 3$ and $C_2/C_0^3 = 0$ are expected. Notice that the sizes of the NLO correction to the energies C_0/C_2^3 scale as the naive estimates $(\xi/\omega)^2$. The correction is consistently smaller than the estimate, implying the breakdown scale of the EFT for the ground band is slightly above the energy scale of vibrations ω.

The effective quadrupole moments of the systems studied in this work, and the LEC of the NLO correction to the inband $B(E2)$ values are listed in Table 3.2. Notice that $b/a \sim C_2/C_0^3$, that is, the NLO correction to the quadrupole transition moments scales as the NLO correction to the energy spectrum. In the last two columns of Table 3.2, the LO and NLO uncertainty parameters are listed. These parameters indicate the size of the theoretical uncertainty required to achieve a reduced χ^2 of one. Uncertainty parameters of order one imply the uncertainty due to omitted terms scales as expected.

Next, the EFT for the nonrigid rotor is tested by comparing it to data on interband transitions strengths in ^{166}Er, ^{168}Er and ^{154}Sm. The erbium isotopes possess energy ratios close to those of a rigid rotor (3.122), while the energy ratios of ^{154}Sm exhibit considerable deviations from this limit.

Table 3.2: LECs and uncertainty parameters for inband $B(E2)$ values for the systems studied in this work. The uncertainty parameters $\alpha_{\rm LO}$ and $\alpha_{\rm NLO}$ are obtained from LO and NLO χ^2 fits, respectively, and indicate the size of theoretical uncertainty required to achieve a reduced χ^2 of one. A blank space implies experimental data was not precise enough to perform NLO calculations.

Rotor	$Q_0[eb]$	b/a	C_2/C_0^3	$\alpha_{\rm LO}$	$\alpha_{\rm NLO}$
N_2	1.00[1]	-0.000010	0.000006	2.18	0.70
H_2	1.00[1]	0.0022	0.0015	1.45	0.10
^{236}U	3.29			0.00	
^{174}Yb	2.44			1.07	
^{168}Er	2.42			3.02	
^{166}Er	2.42			0.00	
^{162}Dy	2.29			0.33	
^{154}Sm	2.08			0.23	
^{188}Os	1.58	0.004	0.012	0.32	0.43
^{154}Gd	1.96	0.004	0.013	0.35	0.00
^{152}Sm	1.86	0.004	0.013	0.20	0.00
^{150}Nd	1.65	0.008	0.017	0.38	0.32

1. Arbitrary units used for molecules.

3.4.1 Inband transitions in linear molecules

Linear molecules provide an ideal testing ground for the EFT, since their energy ratios are close to those for a rigid rotor (3.122), and the separation of scales between rotations and higher-energy modes for these systems is extremely large.

For homonuclear diatomic molecules, that is, molecules composed of two atoms of the same element, an antiparallel alignment of the nuclear spins defines a state referred to as the "para" state. Such a state possesses positive $\mathcal{R}$ parity. As mentioned before, this symmetry is also possessed by axially symmetric nuclei, and causes states in the ground band to have even spins. Thus, in the long wavelength limit, $E2$ transitions are the most relevant within the ground band.

Results on inband transitions within the ground band of the N_2 and H_2 molecules in their "para" state, are shown in the top and bottom of Figure 3.1, respectively. Experimental data taken from the HITRAN database [122] (shown as black dots) are compared against LO and NLO calculations (shown as a solid red line and blue dashed line, respectively). The data from the HITRAN database do not include experimental uncertainties. During the fits, a constant uncertainty $\sigma_{\rm exp} = 0.0002Q_0^2$ was used.

The N_2 molecule posses energy ratios $R_{4/2}$ and ξ/ω extremely close to those

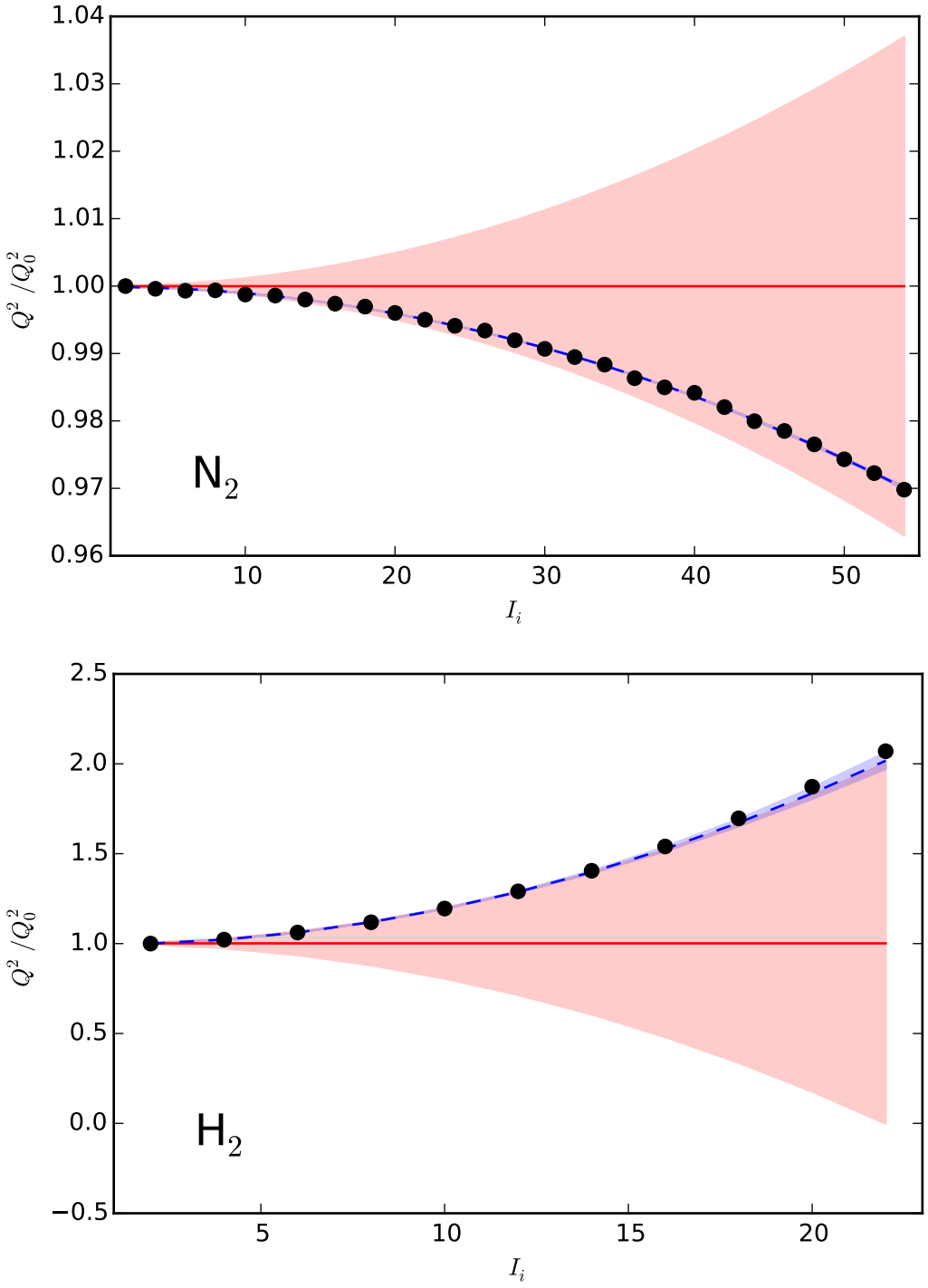

Figure 3.1: Quadrupole transition moments for decays within the ground band of N_2 and H_2. Experimental data, shown as black circles, are compared to LO and NLO calculations, shown as a red and blue dashed line, respectively. Theoretical uncertainty is shown as bands.

of a rigid rotor. Deviations of the data from the LO calculations are less than 1% for decays from states with initial angular momenta $I_i \lesssim 30$. This deviation is quadratic in the spin of the initial state, as predicted by the EFT for the ground band. Deviations from the NLO calculations are less than 0.1% for all the transitions shown in the figure. The theoretical uncertainty at LO and NLO (shown as a red and blue band, respectively) are given by $\alpha_{\rm LO} Q$ and $\alpha_{\rm NLO} Q^2$, respectively, where the uncertainty parameters were obtained from χ^2 fits at LO and NLO, respectively, and $Q \equiv (C_2/C_0^3) I_i (I_i - 1)$.

The energy ratios of the H_2 molecule are not as close to the rigid rotor, as those of the N_2 molecule, because of the former has a much smaller mass than the later. The results for this molecule are shown in the bottom part of Figure 3.1. LO calculations are in agreement with data from the HITRAN database [122] within the theoretical uncertainty. At NLO, a reduced χ^2 of one is obtained for $\alpha_{\rm NLO} \ll 1$, suggesting the theoretical uncertainty has been overestimated.

For both molecules the data is close to the limit of the LO uncertainty band by construction. This is because we vary the parameter $\alpha_{\rm LO}$ until a reduced χ^2 of one is obtained. Values of $\alpha_{\rm LO}$ of order one indicates that the deviations from the LO behavior scale as expected within the EFT. The small size of these deviations even at high spins allow us to classify these system as "good" rotors.

3.4.2 Inband transitions in rotational nuclei

In what follows, we test the EFT against atomic nuclei classified as rotational. The energy spectra of many nuclei in the actinide region make them good candidates to test the EFT. From this region, ^{236}U possesses energy ratios $R_{4/2} \approx 3.3$ and $\xi/\omega \approx 0.05$, suggesting a rotational behavior at low energies. The results for this nucleus are shown in Figure 3.2. The experimental data on $B(E2)$ values for decays within the ground band [123] are consistent with LO calculations up to the 16^+ state, where the EFT is expected to break. The large experimental uncertainty, allows a reduced χ^2 of one even for an uncertainty parameter $\alpha_{\rm LO} = 0$, making a comparison against NLO calculations meaningless. In Figure 3.2, the theoretical uncertainty for $\alpha_{\rm LO} = 1$, is displayed.

The rare earth region also offers good candidates to test the EFT. Among these, ^{174} Yb exhibit the energy ratios in closest agreement with the rigid rotor limit, $R_{4/2} \approx 3.31$ and $\xi/\omega \approx 0.05$. Experimental data [124] are compared against the EFT in Figure 3.3. Data and LO calculations are consistent for an uncertainty

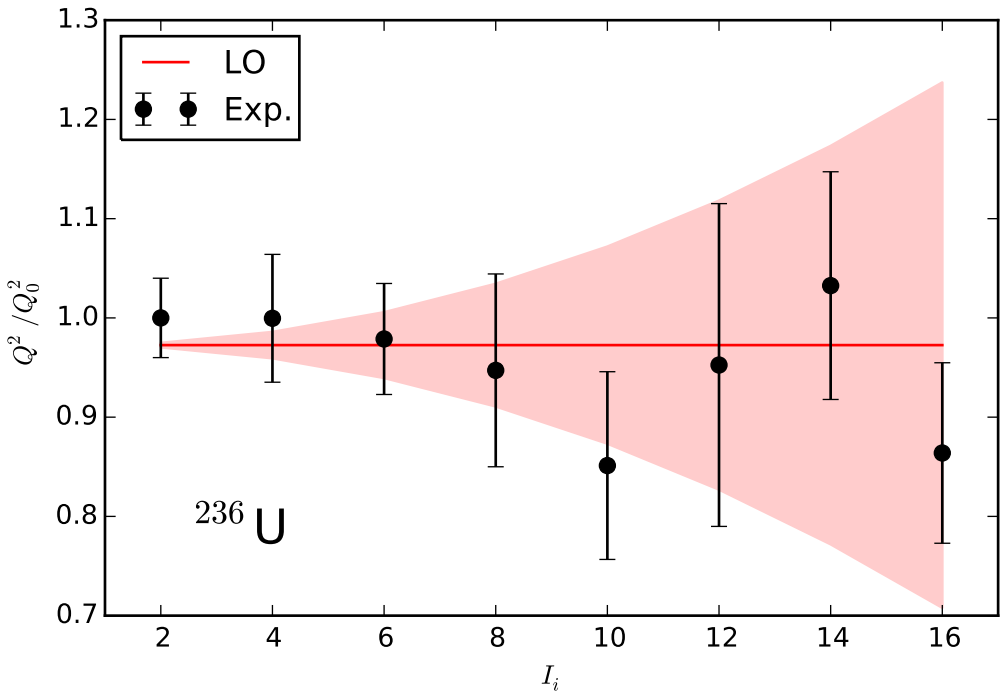

Figure 3.2: Quadrupole transition moments for decays within the ground band of ^{236}U. Experimental data, shown as black circles, are compared against LO calculations, shown as a red line. Experimental uncertainty is shown as error bars. Theoretical uncertainty is shown as a band.

parameter of order one. The experimental uncertainty makes a NLO comparison meaningless. It would be interesting to remeasure or reevaluate the decay from the 8^+ state of the ground band, as its large quadrupole transition moment is not expected within the EFT.

The erbium isotopes with $A = 166, 168$ are two of the most studied rotational nuclei [42, 125, 126, 54, 55]. Figure 3.4 shows our results for ^{168}Er and ^{166}Er in its top and bottom parts, respectively. The energy ratios in ^{168}Er, $R_{4/2} \approx 3.31$ and $\xi/\omega \approx 0.1$, suggest this nucleus is a "better" rotor than ^{166}Er with energy ratios $R_{4/2} \approx 3.29$ and $\xi/\omega \approx 0.1$. However, the experimental data for ^{168}Er [41] exhibits an oscillatory pattern that cannot be understood within the EFT. In this system, a large value for $\alpha_{\rm LO}$ is required to obtain a reduced χ^2 of one in LO fits. For this nucleus it would be interesting to remeasure or reevaluate the $B(E2)$ value for the decay from the 6^+ state of the ground band, as this value deviates significantly from the theoretical prediction. On the other hand, the behavior of ^{166}Er identifies it as one of the best rotational nuclei. The high precision experimental data [127] are consistent with LO calculations, even for an uncertainty parameter $\alpha_{\rm LO} = 0$. The theoretical uncertainty in Figure 3.4 is obtained by setting $\alpha_{\rm LO} = 1$.

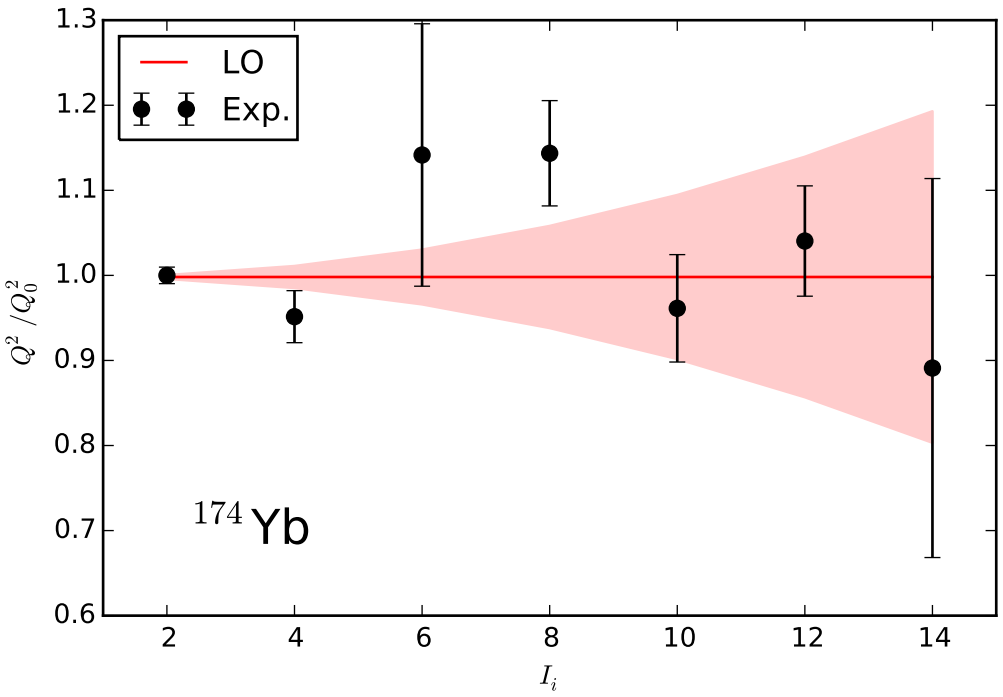

Figure 3.3: Quadrupole transition moments for decays within the ground band of ^{174}Yb. Experimental data, shown as black circles, are compared against LO calculations, shown as a red line. Experimental uncertainty is shown as error bars. Theoretical uncertainty is shown as a band.

Some isotopes in the dysprosium chain exhibit rotational behavior at low energies. From this, ^{162}Dy with energy ratios $R_{4/2} \approx 3.29$ and $\xi/\omega \approx 0.1$, have been extensively studied [128, 68]. In Figure 3.5 experimental data [129] are compared against the EFT. For this nucleus, data are consistent with the LO calculation up to the 8^+ state. Naively, the EFT is expected to break at a higher spins $I_b \sim 10$. Nevertheless, remeasuring or reevaluating the $B(E2)$ value for the decay from the 10^+ state will be interesting.

Finally, the EFT is tested against experimental data for ^{154}Sm [130], a rotational nucleus which energy ratios $R_{4/2} \approx 3.25$ and $\xi/\omega \approx 0.1$ deviate the most from those of a rigid rotor. Results for this nucleus are shown in Figure 3.6. The data are consistent with LO calculations up to the 12^+ state for an uncertainty parameter of order one, despite showing an oscillatory behavior similar to that exhibit by ^{168}Er. However, this oscillation around Q_0^2 has a smaller amplitude in ^{154}Sm than in ^{168}Er.

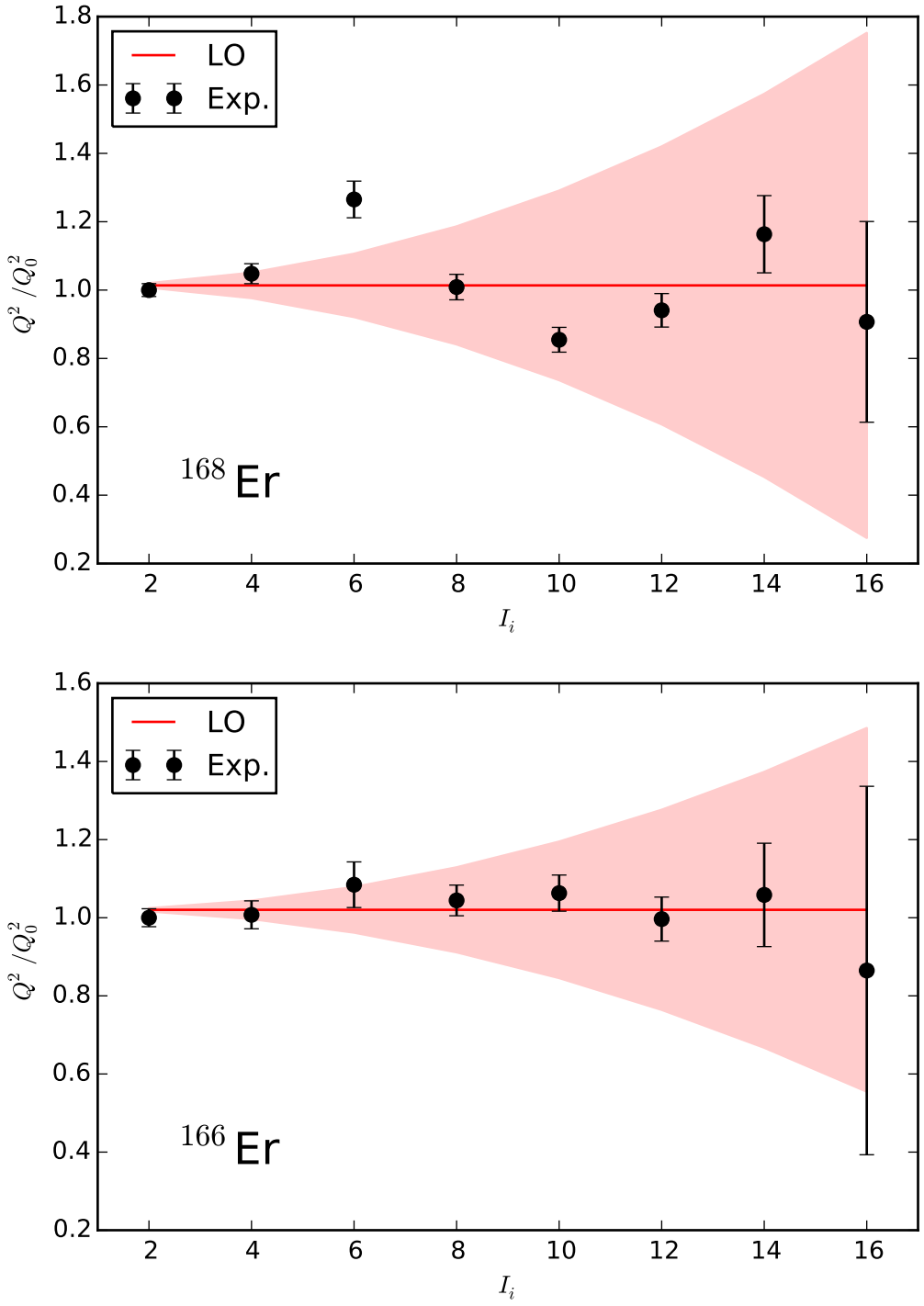

Figure 3.4: Quadrupole transition moments for decays within the ground band of ^{168}Er (top) and ^{166}Er (bottom). Experimental data, shown as black circles, are compared against LO calculations, shown as a red line. Experimental uncertainty is shown as error bars. Theoretical uncertainty is shown as a band.

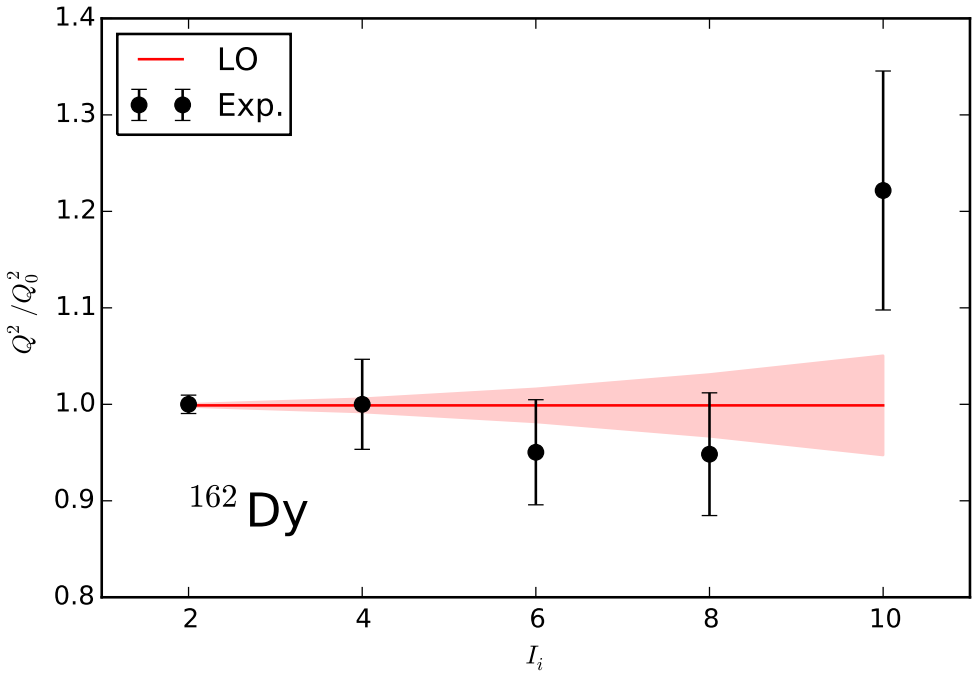

Figure 3.5: Quadrupole transition moments for decays within the ground band of ^{162}Dy. Experimental data, shown as black circles, are compared against LO calculations, shown as a red line. Experimental uncertainty is shown as error bars. Theoretical uncertainty is shown as a band.

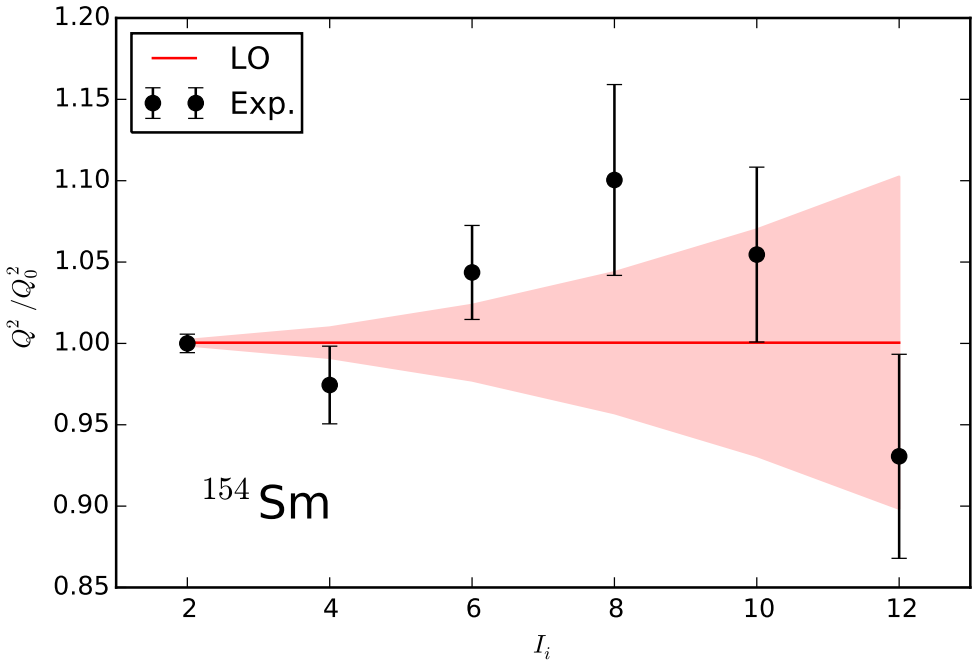

Figure 3.6: Quadrupole transition moments for decays within the ground band of ^{154}Sm. Experimental data, shown as black circles, are compared against LO calculations, shown as a red line. Experimental uncertainty is shown as error bars. Theoretical uncertainty is shown as a band.

3.4.3 Inband transitions in transitional nuclei

The ground band of transitional nuclei, characterized by energy ratios away from those of a rigid rotor, exhibit appreciable deviations from the $I(I+1)$ pattern (see Table 3.1). Thus, NLO corrections become relevant for the description of both the energy spectrum and the decays within the ground band of these systems.

The transitional nuclei studied in this work ^{188}Os, ^{154}Gd, ^{152}Sm and ^{150}Nd, posses very similar energy ratios with values around $R_{4/2} \approx 3$ and $\xi/\omega \approx 0.2$. As seen in Figure 3.7 and Figure 3.8, the $B(E2)$ values for decays within the ground band clearly exhibit a deviation from the rigid rotor behavior, quadratic in the spin of the initial state, as expected within the EFT. The experimental data on these nuclei [57, 131, 132, 61] are consistent with NLO calculations, for spins below the naive breakdown spin $I_b \approx 10$. For ^{154}Gd and ^{152}Sm, a reduced χ^2 of one was obtained in NLO fits, even for an uncertainty parameter $\alpha_{\rm NLO} = 0$. For these nuclei, the NLO theoretical uncertainty shown in the Figures is obtained for $\alpha_{\rm NLO} = \alpha_{\rm LO}$.

3.4.4 Interband transitions

In order to test the EFT against data on interband transition strengths, we compare its predictions against experimental data for ^{168}Er and ^{166}Er, some of the most extensively studied deformed nuclei.

Let us start the study with ^{168}Er. Table 3.3 shows a comparison between experimental and theoretical $B(E2)$ values for inband transitions within the ground and as well as interband transitions in this nucleus. The energy scale of the rotational mode in this system is $\xi \approx 79.8$ keV, while the energies of the bandheads of the β and γ bands, denoted by 0^+_β and 2^+_γ, respectively, are $\omega_0 \approx 1217.2$ keV, and $\omega_2/2 \approx 821.2$ keV, respectively. The LECs are calculated in order to reproduce the following transitions. The LEC Q^2 is calculated from the $B(E2)$ value for the $2^+_g \to 0^+_g$ transition, given by the LO term in Equation (3.105). The subindex g is employed for states in the ground band. The LECs C_β and C_γ are calculated from the $2^+_\beta \to 0^+_g$ and $2^+_\gamma \to 2^+_g$ transitions, respectively, given in Equations (3.115) and (3.116), respectively. Experimental data were taken from Refs. [41, 54]. Employing these transitions to calculate the LECs is in agreement with the expectation for the EFT to describe the low-energy physics of the system. The calculated values $C_\beta = 0.077$ keV$^{-1/2}$ and $C_\gamma = 0.203$ keV$^{-1/2}$, are both consistent with the naive estimation for their scale $\xi^{-1/2} \approx 0.112$ keV$^{-1/2}$ in

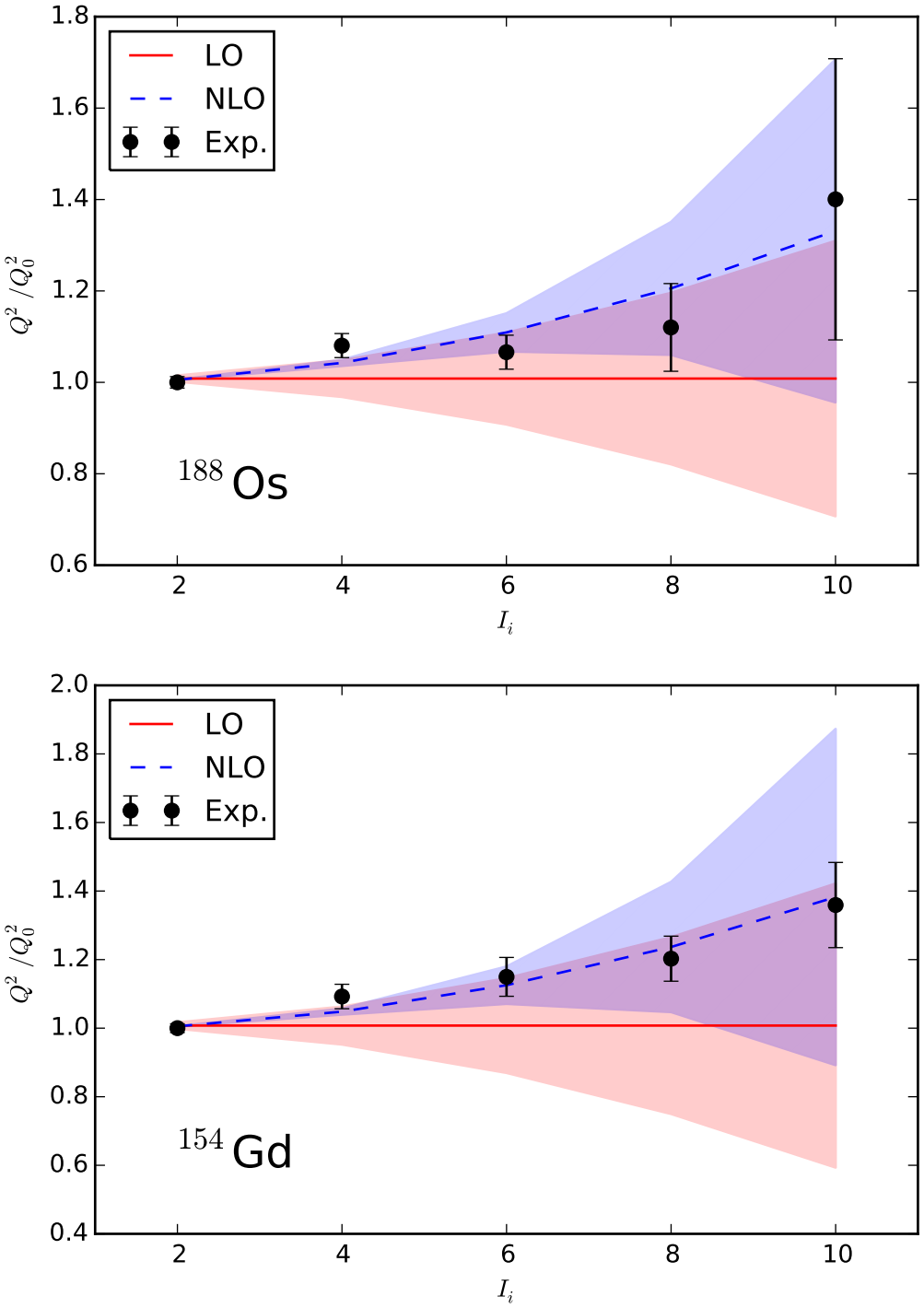

Figure 3.7: Quadrupole transition moments for decays within the ground band of ^{188}Os (top) and ^{154}Gd (bottom). Experimental data, shown as black circles, are compared against LO calculations, shown as a red line. Experimental uncertainty is shown as error bars. Theoretical uncertainty is shown as a band.

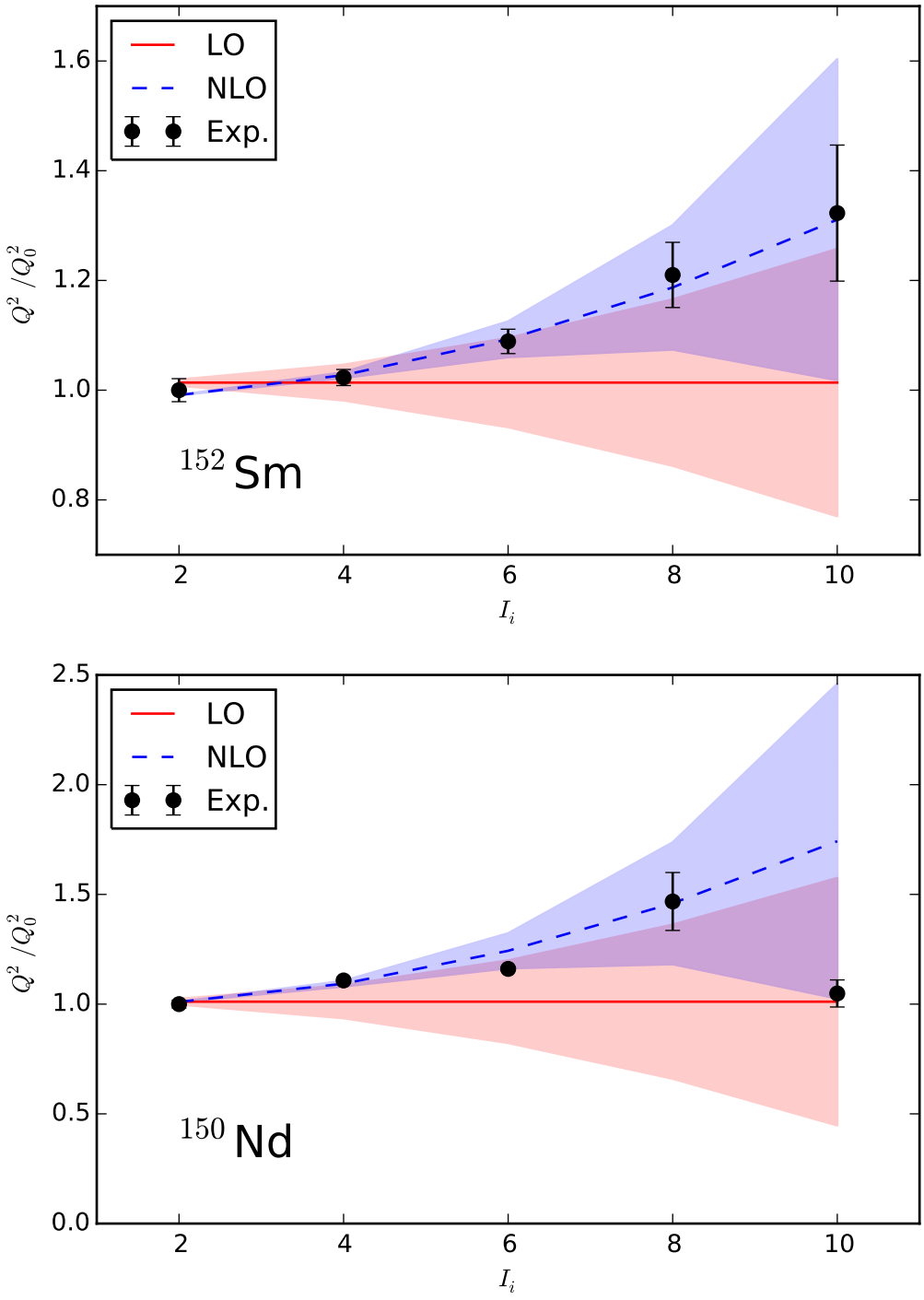

Figure 3.8: Quadrupole transition moments for decays within the ground band of ^{152}Sm (top) and ^{150}Nd (bottom). Experimental data, shown as black circles, are compared against LO calculations, shown as a red line. Experimental uncertainty is shown as error bars. Theoretical uncertainty is shown as a band.

^{168}Er. The rest of $B(E2)$ values for interband transitions in Table 3.3 are predictions within the EFT. The theoretical uncertainty in calculated $B(E2)$ values for interband transitions is naively estimated as $B(E2)(\omega/\Lambda)^2 \sim B(E2)/4$.

Unfortunately, the precision of the data on decays from the β to the ground band is not sufficient to calculate the value of C_β precisely. The theoretical uncertainty in the calculated inband transitions are calculated as described in Section 3.3. Within this uncertainty, experimental data is consistent with the EFT calculations.

Table 3.4 shows a comparison between experimental [127] and theoretical $B(E2)$ values for inband and interband transitions in ^{166}Er. For this nucleus, the relevant energy scales are $\xi \approx 80.6$ keV, $\omega_0 \approx 1460$ keV and $\omega_2/2 \approx 785.9$ keV. Adjusting the LECs C_β and C_γ in order to reproduce the experimental $B(E2)$ values for the $2^+_\beta \to 0^+_g$ and $2^+_\gamma \to 2^+_g$ transitions yields $C_\beta = 0.111$ keV$^{-1/2}$ and $C_\gamma = 0.213$ keV$^{-1/2}$. Once again, both values are consistent with the naive estimate of their scale $\xi^{-1/2} \approx 0.111$ keV$^{-1/2}$.

Experimental data with higher precision would be required to establish the value of C_β precisely. Particularly, it would be interesting to remeasure the $B(E2)$ value for the $2^+_\beta \to 4^+_g$ decay, since its large value is inconsistent with EFT predictions.

Table 3.3: Reduced transition probabilities of ^{168}Er in e^2b^2. Experimental data labeled as $B(E2)_{\rm exp}$ are compared to theoretical results from the EFT, $B(E2)_{\rm EFT}$, and the adiabatic Bohr Hamiltonian, $B(E2)_{\rm BH}$. Experimental data are taken from [41] unless otherwise specified. Values for the adiabatic Bohr Hamiltonian are taken from [25].

$i \to f$	$B(E2)_{\rm exp}$	$B(E2)_{\rm EFT}$	$B(E2)_{\rm BH}$
$2^+_g \to 0^+_g$	1.173 (22)	1.173[2]	1.173
$4^+_g \to 2^+_g$	1.756 (50)	1.676 (36)	1.677
$6^+_g \to 4^+_g$	2.335 (99)	1.846 (91)	1.842
$8^+_g \to 6^+_g$	1.949 (72)	1.932 (169)	1.935
$2^+_\gamma \to 0^+_g$	0.0258 (9)	0.0309 (77)	0.1126
$2^+_\gamma \to 2^+_g$	0.0442 (38)[1]	0.0442[2]	0.1610
$2^+_\gamma \to 4^+_g$	0.0034 (2)	0.0022 (5)	0.0080
$2^+_\beta \to 0^+_g$	0.0020 $(^{+8}_{-20})$	0.0020[2]	0.0387
$2^+_\beta \to 2^+_g$		0.0029 (7)	0.0553
$2^+_\beta \to 4^+_g$	0.0121 $(^{+44}_{-121})$	0.0051 (13)	0.0995

1. From Ref. [54].
2. Values employed to adjust LECs of the EFT.

Finally we compare the EFT to experimental data on interband transitions in ^{154}Sm, the rotational nucleus whose energy ratios are furthest away from those of a rigid rotor within the rotational nuclei studied in this work. Table 3.5 shows a comparison between experimental data on inband [130] and interband $B(E2)$ values [62] against the EFT, the confined β soft model, and the adiabatic Bohr model. The LECs $C_\beta = 0.092$ keV$^{-1/2}$ and $C_\gamma = 0.181$ keV$^{-1/2}$, calculated from the $B(E2)$ values for the $2^+_\beta \to 2^+_g$ and $2^+_\gamma \to 2^+_g$ transitions, respectively, are both consistent with the naive estimate for their scale $\xi^{-1/2} \approx 0.110$ keV$^{-1/2}$. In this nucleus, the high-precision experimental data on interband transitions from Ref. [62] are consistent with LO calculations.

The confined β soft model is a submodel of the Bohr collective model for which the values of β are confined within a hard-wall potential. For more details on this see Ref. [133]. While calculations with this submodel [62] improve over those of the adiabatic Bohr model, they still overpredict interband transition strengths, as shown in Table 3.5.

3.5 Summary

In this chapter, the EFT for a nonrigid rotor coupled to an electromagnetic field was developed in order to consistently describe the energy spectra and electric quadrupole reduced transition probabilities of axially symmetric nuclei. While the energy spectrum predicted by this theory is equivalent to that arising from the

Table 3.4: Reduced transition probabilities of ^{166}Er in $e^2\text{b}^2$. Experimental data labeled as $B(E2)_{\text{exp}}$ are compared to theoretical results from the EFT $B(E2)_{\text{EFT}}$ and the adiabatic Bohr Hamiltonian $B(E2)_{\text{BH}}$. Experimental data are taken from [127]. Values for the adiabatic Bohr Hamiltonian are taken from [25].

$i \to f$	$B(E2)_{\text{exp}}$	$B(E2)_{\text{EFT}}$	$B(E2)_{\text{BH}}$
$2^+_g \to 0^+_g$	1.175 (27)	1.175[1]	1.175
$4^+_g \to 2^+_g$	1.718 (61)	1.679 (24)	1.680
$6^+_g \to 4^+_g$	2.037 (110)	1.849 (60)	1.845
$8^+_g \to 6^+_g$	2.054 (77)	1.935 (112)	1.939
$2^+_\gamma \to 0^+_g$	0.0285 (12)	0.0370 (93)	0.1205
$2^+_\gamma \to 2^+_g$	0.0529 (33)	0.0529[1]	0.1721
$2^+_\gamma \to 4^+_g$	0.0043 (2)	0.0026 (7)	0.0086
$2^+_\beta \to 0^+_g$	0.0036 (4)	0.0036[1]	0.0324
$2^+_\beta \to 2^+_g$		0.0051 (13)	0.0463
$2^+_\beta \to 4^+_g$	0.2113 (325)	0.0093 (23)	0.0834

1. Values employed to adjust the LECs of the EFT.

Table 3.5: Reduced transition probabilities of ^{154}Sm in $e^2\mathrm{b}^2$. Experimental data labeled as $B(E2)_{\mathrm{exp}}$ are compared to theoretical results from the EFT $B(E2)_{\mathrm{EFT}}$, the confined β soft model $B(E2)_{\mathrm{CBS}}$ [133] and the adiabatic Bohr Hamiltonian $B(E2)_{\mathrm{BH}}$. Experimental data are taken from [130, 62]. Values for the confined β soft model are taken from [62]. Values for the adiabatic Bohr Hamiltonian are taken from [25].

$i \to f$	$B(E2)_{\mathrm{exp}}$	$B(E2)_{\mathrm{ET}}$	$B(E2)_{\mathrm{CBS}}$	$B(E2)_{\mathrm{BH}}$
$2_g^+ \to 0_g^+$	0.863 (5)	0.863[1]	0.853	0.863
$4_g^+ \to 2_g^+$	1.201 (29)	1.233 (9)	1.231	1.234
$6_g^+ \to 4_g^+$	1.417 (39)	1.358 (23)	1.378	1.355
$8_g^+ \to 6_g^+$	1.564 (83)	1.421 (43)	1.471	1.424
$2_\gamma^+ \to 0_g^+$	0.0093 (10)	0.0110 (28)		0.0492
$2_\gamma^+ \to 2_g^+$	0.0157 (15)	0.0157[1]		0.0703
$2_\gamma^+ \to 4_g^+$	0.0018 (2)	0.0008 (2)		0.0050
$2_\beta^+ \to 0_g^+$	0.0016 (2)	0.0025 (6)	0.0024	0.0319
$2_\beta^+ \to 2_g^+$	0.0035 (4)	0.0035[1]	0.0069	0.0456
$2_\beta^+ \to 4_g^+$	0.0065 (7)	0.0063 (16)	0.0348	0.0821

1. Values employed to adjust the LECs of the EFT.

Bohr collective model, the transition operators have a richer structure that allow us to accurately describe $E2$ interband transitions at the expense of two additional LECs. The ability to estimate the theoretical uncertainty order by order allows us to compare meaningfully experimental data against the EFT.

With respect to the mentioned $E2$ transitions, the EFT is in qualitative agreement with the Bohr collective model. Within both approaches, inband and interband transitions are established as leading and subleading order effects, respectively. Nevertheless, the richer structure of the interband quadrupole transition operators, consistent with the Hamiltonian, allows for a better description of these transitions. It is important to remember that this description is achieved for LECs of natural size. Particularly, the small reduced transition probabilities for decays from the β band, seem to be of natural size within the EFT. This allows for the characterization of the β bandhead as a vibrational excitation of the ground state.

The results from the comparison against experimental data can be summarized as follows.

(i) Transitions within the ground band of rotational nuclei with energy ratios close to those for a rigid rotor, are consistent with LO calculations within the EFT, below the expected breakdown spin $I_b \approx \omega/\xi$. A NLO comparison

requires experimental data with higher precision, in order for such comparison to be meaningful.

(ii) Transitions within the ground band of the transitional nuclei ^{188}Os, ^{154}Gd, ^{152}Sm and ^{150}Nd, are consistent with NLO calculations below the expected breakdown spin I_b. Deviations from the rigid rotor behavior in these systems follow the quadratic in the spin of the initial state pattern predicted by the EFT.

(iii) Interband transition strengths in the rotational nuclei ^{168}Er, ^{166}Er and ^{154}Sm, are consistent with LO calculations for LECs C_β and C_γ of natural size, that is, consistent with the naive estimate for their scale. Thus, the EFT suggests a solution for the overestimation of these faint transitions at the expense of two additional LECs. Data with higher precision would be desired in order to determine the value of these LECs precisely.

4
SUMMARY AND OUTLOOK

In this work, collective motion in heavy atomic nuclei has been studied within an EFT approach, motivated by the separation of scales between the quadrupole excitation modes and others. Nuclei near shell closures and midshell nuclei are described by two different EFTs. The EFT describing the former is based on the spherical symmetry exhibited by these systems. The later are described by an EFT based on the emergent breaking of the spherical symmetry into the axial symmetry assumed for the ground states of midshell nuclei.

The power counting of the EFT allows for the systematic construction of the most general Lagrangian or Hamiltonian consistent with the symmetries of atomic nuclei. The energy spectra arising from these operators are equivalent to those predicted by some submodels of the Bohr collective model [22, 23, 24, 25]. Thus, the precise description of the spectra within the Bohr collective model, one of its great successes, is also achieved within the EFT.

Coupling the effective DOF to an electromagnetic field leads to transition operators that are consistent with the Hamiltonian. In vibrational nuclei near shell closures, the LO $E2$ operator is equivalent to the $E2$ operator proposed by Bohr. Within the EFT, it is possible to systematically correct this operator by the inclusion of nonminimal couplings between the effective DOF and the electric field. These nonminimal couplings arise due to the fact that the DOF describe composite objects. The NLO correction to the $E2$ operator allows for the description of large static quadrupole moments [30] unlike the Bohr collective model, which predicts vanishing static quadrupole moments. This correction also allows for the description of transitions between states with the same phonon number [30], forbidden within the model.

In the case of rotational nuclei, the coupling of the EFT to an electromagnetic field leads to inband and interband transition operators. These operators arise from the gauging of the NLO and NNLO contributions to the Hamiltonian, respectively. Thus, within the EFT inband and interband transitions are leading and subleading order effects, respectively. Consequently, interband reduced transition probabilities are small when compared to inband ones [29]. Qualitatively, this is in agreement with the Bohr collective model; nevertheless the richer structure

(in the form of two additional LECs) of the transition operators within the EFT, allows for the precise description of interband transitions, thus proposing a solution for their overestimation within the collective model. It is important to notice that this description is achieved for LECs of natural size [29]. The inband transition operator can be corrected by the inclusion of nonminimal couplings between the effective DOF and the electric field. The NLO correction to this operators allows for the precise description of transitions within the ground band of transitional nuclei below certain spin where the EFT is expected to break [29].

The quantification of the theoretical uncertainty via Bayesian analysis methods, allows for a statistical comparison between experimental data and the EFT. Within an EFT, observables can be written as an expansion in powers of a small parameter Q. The quantification of the theoretical uncertainty is based on the assumption that the expansion coefficients are independent of each other, and of order one. These assumptions, encoded in the pdfs for the expansion coefficients, were tested. Coefficients of natural sizes suggest the power counting of the EFT is appropriate. The statistical interpretation of the quantified theoretical uncertainty is studied in Ref. [30], where the data set formed from the energies and $E2$ reduced transition probabilities of some nuclei near shell closures is compared against the EFT employing intervals with a 68% DOB. The percentage of experimental data points that lie within the theoretical uncertainty is in agreement with the expected 68%, for the size of the data set.

Within these EFT approaches to collective motion in atomic nuclei, it is possible to describe electromagnetic transitions of different multipolarities. The study of magnetic dipole transitions, expected to be comparable in strength to $E2$ transitions, is required to complete the description of electromagnetic transitions at this order in the multipole expansion. Therefore, nonminimal couplings between the effective DOF and the magnetic field consistent with the symmetries of the system must be constructed.

The EFTs presented here can be extended by the inclusion of additional DOF. For rotational nuclei, the inclusion of fermionic DOF will enable the study of even-odd systems. The fermion orbitals can be inferred from the Nilsson model. In nuclei near shell closures, the distinction between protons and neutrons, and the inclusion of octopole degrees of freedom would raise the low breakdown scale, enabling the EFT to describe these systems at higher energies.

REFERENCES

[1] S. Weinberg, "Nuclear forces from chiral lagrangians," *Physics Letters B*, vol. 251, no. 2, pp. 288 – 292, 1990.

[2] S. Weinberg, "Effective chiral lagrangians for nucleon-pion interactions and nuclear forces," *Nuclear Physics B*, vol. 363, no. 1, pp. 3 – 18, 1991.

[3] S. Weinberg, "Three-body interactions among nucleons and pions," *Physics Letters B*, vol. 295, no. 1, pp. 114 – 121, 1992.

[4] E. Epelbaum, H.-W. Hammer, and U.-G. Meißner, "Modern theory of nuclear forces," *Rev. Mod. Phys.*, vol. 81, pp. 1773–1825, Dec 2009.

[5] R. Machleidt and D. Entem, "Chiral effective field theory and nuclear forces," *Physics Reports*, vol. 503, no. 1, pp. 1 – 75, 2011.

[6] P. Bedaque and U. van Kolck, "Nucleon-deuteron scattering from an effective field theory," *Physics Letters B*, vol. 428, no. 34, pp. 221 – 226, 1998.

[7] P. F. Bedaque, H.-W. Hammer, and U. van Kolck, "Renormalization of the three-body system with short-range interactions," *Phys. Rev. Lett.*, vol. 82, pp. 463–467, Jan 1999.

[8] P. Bedaque, H.-W. Hammer, and U. van Kolck, "Effective theory of the triton," *Nuclear Physics A*, vol. 676, no. 14, pp. 357 – 370, 2000.

[9] P. F. Bedaque, G. Rupak, H. W. Griehammer, and H.-W. Hammer, "Low energy expansion in the three body system to all orders and the triton channel," *Nuclear Physics A*, vol. 714, no. 34, pp. 589 – 610, 2003.

[10] A. Gezerlis, I. Tews, E. Epelbaum, S. Gandolfi, K. Hebeler, A. Nogga, and A. Schwenk, "Quantum monte carlo calculations with chiral effective field theory interactions," *Phys. Rev. Lett.*, vol. 111, p. 032501, Jul 2013.

[11] I. Tews, S. Gandolfi, A. Gezerlis, and A. Schwenk, "Quantum Monte Carlo calculations of neutron matter with chiral three-body forces," *ArXiv e-prints*, July 2015.

[12] C. Bertulani, H.-W. Hammer, and U. van Kolck, "Effective field theory for halo nuclei: shallow p-wave states," *Nuclear Physics A*, vol. 712, no. 12, pp. 37 – 58, 2002.

[13] E. Ryberg, C. Forssén, H.-W. Hammer, and L. Platter, "Effective field theory for proton halo nuclei," *Phys. Rev. C*, vol. 89, p. 014325, Jan 2014.

[14] E. Ryberg, C. Forssén, H.-W. Hammer, and L. Platter, "Constraining low-energy proton capture on beryllium-7 through charge radius measurements," *The European Physical Journal A*, vol. 50, no. 11, 2014.

[15] X. Zhang, K. M. Nollett, and D. R. Phillips, "Combining *ab initio* calculations and low-energy effective field theory for halo nuclear systems: The case of $^7\mathrm{Li} + n \to ^8\mathrm{Li} + \gamma$," *Phys. Rev. C*, vol. 89, p. 024613, Feb 2014.

[16] X. Zhang, K. M. Nollett, and D. R. Phillips, "Combining *ab initio* calculations and low-energy effective field theory for halo nuclear systems: The case of $^7\mathrm{Be} + p \to ^8\mathrm{B} + \gamma$," *Phys. Rev. C*, vol. 89, p. 051602, May 2014.

[17] G. Hagen, T. Papenbrock, D. J. Dean, and M. Hjorth-Jensen, "*Ab initio* coupled-cluster approach to nuclear structure with modern nucleon-nucleon interactions," *Phys. Rev. C*, vol. 82, p. 034330, Sep 2010.

[18] P. Navrátil, R. Roth, and S. Quaglioni, "*Ab initio* many-body calculations of nucleon scattering on ^{4}He, ^{7}Li, ^{7}Be, ^{12}C, and ^{16}O," *Phys. Rev. C*, vol. 82, p. 034609, Sep 2010.

[19] G. Hagen, M. Hjorth-Jensen, G. R. Jansen, R. Machleidt, and T. Papenbrock, "Evolution of shell structure in neutron-rich calcium isotopes," *Phys. Rev. Lett.*, vol. 109, p. 032502, Jul 2012.

[20] B. R. Barrett, P. Navrtil, and J. P. Vary, "Ab initio no core shell model," *Progress in Particle and Nuclear Physics*, vol. 69, no. 0, pp. 131 – 181, 2013.

[21] G. Hagen, P. Hagen, H.-W. Hammer, and L. Platter, "Efimov physics around the neutron-rich ^{60}Ca isotope," *Phys. Rev. Lett.*, vol. 111, p. 132501, Sep 2013.

[22] A. Bohr, "The coupling of nuclear surface oscillations to the motion of individual nucleons," *Dan. Mat. Fys. Medd.*, vol. 26, p. no. 14, 1952.

[23] A. Bohr and B. R. Mottelson, "Collective and individual-particle aspects of nuclear structure," *Dan. Mat. Fys. Medd.*, vol. 27, p. no. 16, 1953.

[24] A. Bohr and B. R. Mottelson, *Nuclear Structure*, vol. II: Nuclear Deformations. New York: W. A. Benjamin, 1975.

[25] D. J. Rowe and J. L. Wood, *Fundamentals of Nuclear Models*, vol. I: Foundational Models. Singapore: World Scientific, 2010.

[26] T. Papenbrock, "Effective theory for deformed nuclei," *Nuclear Physics A*, vol. 852, no. 1, pp. 36 – 60, 2011.

[27] J. Zhang and T. Papenbrock, "Rotational constants of multi-phonon bands in an effective theory for deformed nuclei," *Phys. Rev. C*, vol. 87, p. 034323, Mar 2013.

[28] T. Papenbrock and H. A. Weidenmüller, "Effective field theory for finite systems with spontaneously broken symmetry," *Phys. Rev. C*, vol. 89, p. 014334, Jan 2014.

[29] E. A. Coello Pérez and T. Papenbrock, "Effective theory for the nonrigid rotor in an electromagnetic field: Toward accurate and precise calculations of $e2$ transitions in deformed nuclei," *Phys. Rev. C*, vol. 92, p. 014323, Jul 2015.

[30] E. A. Coello Pérez and T. Papenbrock, "Effective field theory for nuclear vibrations with quantified uncertainties," *ArXiv e-prints*, Oct. 2015.

[31] S. Weinberg, "Nonlinear realizations of chiral symmetry," *Phys. Rev.*, vol. 166, pp. 1568–1577, Feb 1968.

[32] C. G. Callan, S. Coleman, J. Wess, and B. Zumino, "Structure of phenomenological lagrangians. ii," *Phys. Rev.*, vol. 177, pp. 2247–2250, Jan 1969.

[33] S. Coleman, J. Wess, and B. Zumino, "Structure of phenomenological lagrangians. i," *Phys. Rev.*, vol. 177, pp. 2239–2247, Jan 1969.

[34] J. Goldstone, A. Salam, and S. Weinberg, "Broken symmetries," *Phys. Rev.*, vol. 127, pp. 965–970, Aug 1962.

[35] H. Leutwyler, "Nonrelativistic effective lagrangians," *Phys. Rev. D*, vol. 49, pp. 3033–3043, Mar 1994.

[36] P. Hasenfratz and F. Niedermayer, "Finite size and temperature effects in the af heisenberg model," *Zeitschrift für Physik B Condensed Matter*, vol. 92, no. 1, pp. 91–112, 1993.

[37] J. D. Jackson, *Classical Electrodynamics*. New York: Wiley, third ed., 1998.

[38] R. J. Furnstahl, D. R. Phillips, and S. Wesolowski, "A recipe for EFT uncertainty quantification in nuclear physics," *Journal of Physics G: Nuclear and Particle Physics*, vol. 42, no. 3, p. 034028, 2015.

[39] J. Dobaczewski, W. Nazarewicz, and P.-G. Reinhard, "Error estimates of theoretical models: a guide," *Journal of Physics G: Nuclear and Particle Physics*, vol. 41, no. 7, p. 074001, 2014.

[40] R. J. Furnstahl, N. Klco, D. R. Phillips, and S. Wesolowski, "Quantifying truncation errors in effective field theory," *Phys. Rev. C*, vol. 92, p. 024005, Aug 2015.

[41] C. M. Baglin, "Nuclear data sheets for A = 168," *Nuclear Data Sheets*, vol. 111, no. 7, pp. 1807 – 2080, 2010.

[42] W. F. Davidson, D. D. Warner, R. F. Casten, K. Schreckenbach, H. G. Börner, J. Simic, M. Stojanovic, M. Bogdanovic, S. Koicki, W. Gelletly, G. B. Orr, and M. L. Stelts, "Identification of all intrinsic excitations below 2 mev in 168 er," *Journal of Physics G: Nuclear Physics*, vol. 7, no. 4, p. 455, 1981.

[43] A. Bohr and B. R. Mottelson, "Interpretation of isomeric transitions of electric quadrupole type," *Phys. Rev.*, vol. 89, pp. 316–317, Jan 1953.

[44] A. Bohr and B. R. Mottelson, "Rotational states in even-even nuclei," *Phys. Rev.*, vol. 90, pp. 717–719, May 1953.

[45] G. Alaga, K. Alder, A. Bohr, and B. R. Mottelson, "Intensity rules for beta and gamma transitions to nuclear rotational states," *Dan. Mat. Fys. Medd.*, vol. 29, p. no. 9, 1955.

[46] K. Kitao, Y. Tendow, and A. Hashizume, "Nuclear data sheets for A = 120," *Nuclear Data Sheets*, vol. 96, no. 2, pp. 241 – 390, 2002.

[47] V. F. Weisskopf, "Radiative transition probabilities in nuclei," *Phys. Rev.*, vol. 83, pp. 1073–1073, Sep 1951.

[48] S. Raman, C. N. JR., and P. Tikkanen, "Transition probability from the ground to the first 2^+ state of even-even nuclides," *Atomic Data and Nuclear Data Tables*, vol. 78, no. 1, pp. 1 – 128, 2001.

[49] N. Stone, "Table of nuclear magnetic dipole and electric quadrupole moments," *Atomic Data and Nuclear Data Tables*, vol. 90, no. 1, pp. 75 – 176, 2005.

[50] D. A. Varshalovich, A. N. Moskalev, and V. K. Khersonskii, *Quantum Theory of Angular Momentum*. Singapore: World Scientific Pub., 1988.

[51] E. Merzbacher, *Quantum Mechanics*. New York: Wiley, third ed., 1998.

[52] P. E. Garrett and J. L. Wood, "On the robustness of surface vibrational modes: case studies in the cd region," *Journal of Physics G: Nuclear and Particle Physics*, vol. 37, no. 6, p. 069701, 2010.

[53] R. O. Sayer, E. Eichler, N. R. Johnson, D. C. Hensley, and L. L. Riedinger, "Coulomb excitation of ground bands in ^{160,162,164}Dy with ^{20}Ne and ^{35}Cl ions," *Phys. Rev. C*, vol. 9, pp. 1103–1112, Mar 1974.

[54] B. Kotliński, D. Cline, A. Bcklin, K. Helmer, A. Kavka, W. Kernan, E. Vogt, C. Wu, R. Diamond, A. Macchiavelli, and M. Deleplanque, "Coulomb excitation of ^{168}Er," *Nuclear Physics A*, vol. 517, no. 2, pp. 365 – 385, 1990.

[55] C. Fahlander, I. Thorslund, B. Varnestig, A. Bcklin, L. Svensson, D. Disdier, L. Kraus, I. Linck, N. Schulz, J. Pedersen, and D. Cline, "Triaxiality in ^{166}Er," *Nuclear Physics A*, vol. 537, no. 12, pp. 183 – 206, 1992.

[56] L. Svensson, C. Fahlander, L. Hasselgren, A. Bcklin, L. Westerberg, D. Cline, T. Czosnyka, C. Wu, R. Diamond, and H. Kluge, "Multiphonon vibrational states in ^{106,108}Pd," *Nuclear Physics A*, vol. 584, no. 3, pp. 547 – 572, 1995.

[57] C. Wu, D. Cline, T. Czosnyka, A. Backlin, C. Baktash, R. Diamond, G. Dracoulis, L. Hasselgren, H. Kluge, B. Kotliński, J. Leigh, J. Newton, W. Phillips, S. Sie, J. Srebrny, and F. Stephens, "Quadrupole collectivity and shapes of Os-Pt nuclei," *Nuclear Physics A*, vol. 607, no. 2, pp. 178 – 234, 1996.

[58] C. Fahlander, A. Axelsson, M. Heinebrodt, T. Härtlein, and D. Schwalm, "Two-phonon γ-vibrational states in 166er," *Physics Letters B*, vol. 388, no. 3, pp. 475 – 480, 1996.

[59] T. Härtlein, M. Heinebrodt, D. Schwalm, and C. Fahlander, "Collective excitations built on the 2+ γ state in 168er," *The European Physical Journal A - Hadrons and Nuclei*, vol. 2, pp. 253–261, 1998.

[60] O. Kenn, K.-H. Speidel, R. Ernst, J. Gerber, N. Benczer-Koller, G. Kumbartzki, P. Maier-Komor, and F. Nowacki, "Striking harmony between the nuclear shell model and new experimental $\boldsymbol{g}$ factors and $b(e2)$ values of even ni isotopes," *Phys. Rev. C*, vol. 63, p. 021302, Dec 2000.

[61] R. Krücken, B. Albanna, C. Bialik, R. F. Casten, J. R. Cooper, A. Dewald, N. V. Zamfir, C. J. Barton, C. W. Beausang, M. A. Caprio, A. A. Hecht, T. Klug, J. R. Novak, N. Pietralla, and P. von Brentano, "$B(E2)$ values in ^{150}Nd and the critical point symmetry X(5)," *Phys. Rev. Lett.*, vol. 88, p. 232501, May 2002.

[62] T. Möller, N. Pietralla, G. Rainovski, T. Ahn, C. Bauer, M. P. Carpenter, L. Coquard, R. V. F. Janssens, J. Leske, C. J. Lister, E. A. McCutchan, O. Möller, D. Seweryniak, and S. Zhu, "Absolute β-to-ground band transition strengths in ^{154}Sm," *Phys. Rev. C*, vol. 86, p. 031305, Sep 2012.

[63] D. Radeck, V. Werner, G. Ilie, N. Cooper, V. Anagnostatou, T. Ahn, L. Bettermann, R. J. Casperson, R. Chevrier, A. Heinz, J. Jolie, D. McCarthy, M. K. Smith, and E. Williams, "Simultaneous deorientation and lifetime measurement in ^{98}Ru using the recoil distance Doppler shift method in inverse Coulomb excitation," *Phys. Rev. C*, vol. 85, p. 014301, Jan 2012.

[64] H. Lehmann, P. Garrett, J. Jolie, C. McGrath, M. Yeh, and S. Yates, "On the nature of three-phonon excitations in 112cd," *Physics Letters B*, vol. 387, no. 2, pp. 259 – 265, 1996.

[65] P. Garrett, M. Kadi, C. McGrath, V. Sorokin, M. Li, M. Yeh, and S. Yates, "The nature of 0+ excitations in 166er," *Physics Letters B*, vol. 400, no. 34, pp. 250 – 254, 1997.

[66] F. Corminboeuf, T. B. Brown, L. Genilloud, C. D. Hannant, J. Jolie, J. Kern, N. Warr, and S. W. Yates, "Characterization of three-phonon states in ^{110}Cd," *Phys. Rev. Lett.*, vol. 84, pp. 4060–4063, May 2000.

[67] P. E. Garrett, "Characterization of the β vibration and 0_2^+ states in deformed nuclei," *Journal of Physics G: Nuclear and Particle Physics*, vol. 27, no. 1, p. R1, 2001.

[68] A. Aprahamian, X. Wu, S. R. Lesher, D. D. Warner, W. Gelletly, H. G. Börner, F. Hoyler, K. Schreckenbach, R. F. Casten, Z. R. Shi, D. Kusnezov, M. Ibrahim, A. O. Macchiavelli, M. A. Brinkman, and J. A. Becker, "Complete spectroscopy of the ^{162}Dy nucleus," *Nuclear Physics A*, vol. 764, no. 0, pp. 42 – 78, 2006.

[69] A. Chakraborty, J. N. Orce, S. F. Ashley, B. A. Brown, B. P. Crider, E. Elhami, M. T. McEllistrem, S. Mukhopadhyay, E. E. Peters, B. Singh, and

S. W. Yates, "Status of vibrational structure in ^{62}Ni," *Phys. Rev. C*, vol. 83, p. 034316, Mar 2011.

[70] P. E. Garrett, K. L. Green, and J. L. Wood, "Breakdown of vibrational motion in the isotopes $^{110\text{-}116}$Cd," *Phys. Rev. C*, vol. 78, p. 044307, Oct 2008.

[71] G. Gneuss, U. Mosel, and W. Greiner, "A new treatment of the collective nuclear hamiltonian," *Physics Letters B*, vol. 30, no. 6, pp. 397–399, 1969.

[72] G. Gneuss, U. Mosel, and W. Greiner, "On the relationship between the level-structures in spherical and deformed nuclei," *Physics Letters B*, vol. 31, no. 5, pp. 269 – 272, 1970.

[73] G. Gneuss and W. Greiner, "Collective potential energy surfaces and nuclear structure," *Nuclear Physics A*, vol. 171, no. 3, pp. 449 – 479, 1971.

[74] P. Hess, M. Seiwert, J. Maruhn, and W. Greiner, "General collective model and its application to 92 238 u," *Zeitschrift für Physik A Atoms and Nuclei*, vol. 296, no. 2, pp. 147–163, 1980.

[75] P. O. Hess, J. Maruhn, and W. Greiner, "The general collective model applied to the chains of pt, os and w isotopes," *Journal of Physics G: Nuclear Physics*, vol. 7, no. 6, p. 737, 1981.

[76] A. L. Nichols, B. Singh, and J. K. Tuli, "Nuclear data sheets for A = 62," *Nuclear Data Sheets*, vol. 113, no. 4, pp. 973 – 1114, 2012.

[77] O. Kenn, K.-H. Speidel, R. Ernst, J. Gerber, P. Maier-Komor, and F. Nowacki, "Measurements of g factors and lifetimes of low lying states in $^{58\check{}64}$Ni and their shell model implications," *Phys. Rev. C*, vol. 63, p. 064306, May 2001.

[78] J. N. Orce, B. Crider, S. Mukhopadhyay, E. Peters, E. Elhami, M. Scheck, B. Singh, M. T. McEllistrem, and S. W. Yates, "Determination of the $2_1^+ \rightarrow 0_1^+$ transition strengths in ^{58}Ni and ^{60}Ni," *Phys. Rev. C*, vol. 77, p. 064301, Jun 2008.

[79] B. Singh and Z. Hu, "Nuclear data sheets for A = 98," *Nuclear Data Sheets*, vol. 98, no. 2, pp. 335 – 513, 2003.

[80] B. Singh, "Nuclear data sheets for A = 100," *Nuclear Data Sheets*, vol. 109, no. 2, pp. 297 – 516, 2008.

[81] A. Giannatiempo, A. Nannini, P. Sona, and D. Cutoiu, "Full-symmetry and mixed-symmetry states in even ruthenium isotopes," *Phys. Rev. C*, vol. 52, pp. 2969–2983, Dec 1995.

[82] A. Giannatiempo, A. Nannini, A. Perego, P. Sona, and D. Cutoiu, "Spin-parity assignments and evidence for mixed-symmetry states in ^{100}Ru," *Phys. Rev. C*, vol. 53, pp. 2770–2775, Jun 1996.

[83] H. Klein, A. F. Lisetskiy, N. Pietralla, C. Fransen, A. Gade, and P. von Brentano, "Proton-neutron mixed-symmetry $2^+_{\rm ms}$ and $3^+_{\rm ms}$ states in ^{96}Ru," *Phys. Rev. C*, vol. 65, p. 044315, Mar 2002.

[84] B. Kharraja, U. Garg, S. S. Ghugre, H. Jin, R. V. F. Janssens, I. Ahmad, H. Amro, M. P. Carpenter, S. Fischer, T. L. Khoo, T. Lauritsen, D. Nisius, W. Reviol, W. F. Mueller, L. L. Riedinger, R. Kaczarowski, E. Ruchowska, W. C. Ma, and I. M. Govil, "Recoil-distance lifetime measurements in ^{96,97,98}Ru : search for possible onset of collectivity at $N >\sim 52$," *Phys. Rev. C*, vol. 61, p. 024301, Dec 1999.

[85] J. Timár, J. Gizon, A. Gizon, D. Sohler, B. M. Nyakó, L. Zolnai, A. J. Boston, D. T. Joss, E. S. Paul, A. T. Semple, C. M. Parry, and I. Ragnarsson, "Terminating bands in ^{98,99,100}Ru nuclei: New information on the neutron $2d_{5/2}$ and $1g_{7/2}$ energy spacing," *Phys. Rev. C*, vol. 62, p. 044317, Sep 2000.

[86] R. B. Cakirli, R. F. Casten, E. A. McCutchan, H. Ai, H. Amro, M. Babilon, C. W. Beausang, A. Heinz, R. O. Hughes, D. A. Meyer, C. Plettner, J. J. Ressler, and N. V. Zamfir, "Breakdown of vibrational structure in ^{98}Ru," *Phys. Rev. C*, vol. 70, p. 044312, Oct 2004.

[87] D. D. Frenne and A. Negret, "Nuclear data sheets for A = 106," *Nuclear Data Sheets*, vol. 109, no. 4, pp. 943 – 1102, 2008.

[88] J. Blachot, "Nuclear data sheets for A = 108," *Nuclear Data Sheets*, vol. 91, no. 2, pp. 135 – 296, 2000.

[89] K.-H. Kim, A. Gelberg, T. Mizusaki, T. Otsuka, and P. von Brentano, "IBM-2 calculations of even-even Pd nuclei," *Nuclear Physics A*, vol. 604, no. 2, pp. 163 – 182, 1996.

[90] A. Giannatiempo, A. Nannini, and P. Sona, "Interacting boson approximation-2 analysis of the Pd and Ru chains. i. mixed symmetry states

of $F_{\max} - 1$ character in even palladium isotopes," *Phys. Rev. C*, vol. 58, pp. 3316–3334, Dec 1998.

[91] P. H. Regan, T. M. Menezes, C. J. Pearson, W. Gelletly, C. S. Purry, P. M. Walker, S. Juutinen, R. Julin, K. Helariutta, A. Savelius, P. Jones, P. Jämsen, M. Muikku, P. A. Butler, G. Jones, and P. Greenlees, "Observation of $(h_{11/2})^2$ neutron alignments in ^{100}Mo, ^{104}Ru, and ^{108}Pd using deep inelastic reactions," *Phys. Rev. C*, vol. 55, pp. 2305–2313, May 1997.

[92] G. Gurdal and F. Kondev, "Nuclear data sheets for A = 110," *Nuclear Data Sheets*, vol. 113, no. 5, pp. 1315 – 1561, 2012.

[93] D. Frenne and E. Jacobs, "Nuclear data sheets for A = 112," *Nuclear Data Sheets*, vol. 79, no. 3, pp. 639 – 758, 1996.

[94] J. Blachot, "Nuclear data sheets for A = 114," *Nuclear Data Sheets*, vol. 113, no. 2, pp. 515 – 714, 2012.

[95] J. Kern, P. Garrett, J. Jolie, and H. Lehmann, "Search for nuclei exhibiting the U(5) dynamical symmetry," *Nuclear Physics A*, vol. 593, no. 1, pp. 21 – 47, 1995.

[96] D. Bandyopadhyay, S. R. Lesher, C. Fransen, N. Boukharouba, P. E. Garrett, K. L. Green, M. T. McEllistrem, and S. W. Yates, "Investigation of phonon excitations in ^{114}Cd with the $(n, n'\gamma)$ reaction," *Phys. Rev. C*, vol. 76, p. 054308, Nov 2007.

[97] P. E. Garrett, J. Bangay, A. Diaz Varela, G. C. Ball, D. S. Cross, G. A. Demand, P. Finlay, A. B. Garnsworthy, K. L. Green, G. Hackman, C. D. Hannant, B. Jigmeddorj, J. Jolie, W. D. Kulp, K. G. Leach, J. N. Orce, A. A. Phillips, A. J. Radich, E. T. Rand, M. A. Schumaker, C. E. Svensson, C. Sumithrarachchi, S. Triambak, N. Warr, J. Wong, J. L. Wood, and S. W. Yates, "Detailed spectroscopy of ^{110}cd: Evidence for weak mixing and the emergence of γ-soft behavior," *Phys. Rev. C*, vol. 86, p. 044304, Oct 2012.

[98] K. Heyde, P. Van Isacker, M. Waroquier, G. Wenes, and M. Sambataro, "Description of the low-lying levels in ^{112,114}Cd," *Phys. Rev. C*, vol. 25, pp. 3160–3177, Jun 1982.

[99] R. Meyer and L. Peker, "Evidence for the coexistence of shapes in even-mass cd nuclei," *Zeitschrift für Physik A Atoms and Nuclei*, vol. 283, no. 4, pp. 379–382, 1977.

[100] M. Kadi, N. Warr, P. E. Garrett, J. Jolie, and S. W. Yates, "Vibrational and intruder structures in ^{116}Cd," *Phys. Rev. C*, vol. 68, p. 031306, Sep 2003.

[101] P. E. Garrett, K. L. Green, H. Lehmann, J. Jolie, C. A. McGrath, M. Yeh, and S. W. Yates, "Properties of ^{112}Cd from the $(n, n'\gamma)$ reaction: Lifetimes and transition rates," *Phys. Rev. C*, vol. 75, p. 054310, May 2007.

[102] K. Kitao, "Nuclear data sheets update for A = 118," *Nuclear Data Sheets*, vol. 75, no. 1, pp. 99 – 198, 1995.

[103] T. Tamura, "Nuclear data sheets for A = 122," *Nuclear Data Sheets*, vol. 108, no. 3, pp. 455 – 632, 2007.

[104] E. S. Paul, D. B. Fossan, J. M. Sears, and I. Thorslund, "Favored noncollective oblate states in light tellurium isotopes," *Phys. Rev. C*, vol. 52, pp. 2984–2988, Dec 1995.

[105] E. S. Paul, D. B. Fossan, G. J. Lane, J. M. Sears, I. Thorslund, and P. Vaska, "High-spin states in ^{121,122}Te: Identification of favored noncollective oblate states," *Phys. Rev. C*, vol. 53, pp. 1562–1570, Apr 1996.

[106] J. R. Vanhoy, R. T. Coleman, K. A. Crandell, S. F. Hicks, B. A. Sklaney, M. M. Walbran, N. V. Warr, J. Jolie, F. Corminboeuf, L. Genilloud, J. Kern, J.-L. Schenker, and P. E. Garrett, "Structure of ^{120}Te from the ^{118}Sn$(\alpha, 2n\gamma)$ reaction and ^{120}I decay," *Phys. Rev. C*, vol. 68, p. 034315, Sep 2003.

[107] S. F. Hicks, G. K. Alexander, C. A. Aubin, M. C. Burns, C. J. Collard, M. M. Walbran, J. R. Vanhoy, E. Jensen, P. E. Garrett, M. Kadi, A. Martin, N. Warr, and S. W. Yates, "Intruder structures observed in ^{122}Te through inelastic neutron scattering," *Phys. Rev. C*, vol. 71, p. 034307, Mar 2005.

[108] S. F. Hicks, J. R. Vanhoy, and S. W. Yates, "Fragmentation of mixed-symmetry excitations in stable even-even tellurium nuclei," *Phys. Rev. C*, vol. 78, p. 054320, Nov 2008.

[109] S. Nag, A. K. Singh, A. N. Wilson, J. Rogers, H. Hübel, A. Bürger, S. Chmel, I. Ragnarsson, G. Sletten, B. Herskind, M. P. Carpenter, R. V. F. Janssens, T. L. Khoo, F. G. Kondev, T. Lauritsen, S. Zhu, A. Korichi, H. Ha, P. Fallon, A. O. Macchiavelli, B. M. Nyakó, J. Timár, and K. Juhász, "Collective and noncollective states in ^{120}Te," *Phys. Rev. C*, vol. 85, p. 014310, Jan 2012.

[110] J. Cizewski, "Energy ratios in medium and heavy mass nuclei. signatures of coexisting configurations," *Physics Letters B*, vol. 219, no. 23, pp. 189 – 193, 1989.

[111] E. Williams, C. Plettner, E. A. McCutchan, H. Levine, N. V. Zamfir, R. B. Cakirli, R. F. Casten, H. Ai, C. W. Beausang, G. Gürdal, A. Heinz, J. Qian, D. A. Meyer, N. Pietralla, and V. Werner, "Revisiting anomalous $B(e2; 4_1^+ \to 2_1^+)/B(e2; 2_1^+ \to 0_1^+)$ values in ^{98}Ru and ^{180}Pt," *Phys. Rev. C*, vol. 74, p. 024302, Aug 2006.

[112] C. Fahlander, A. Bäcklin, L. Hasselgren, A. Kavka, V. Mittal, L. E. Svensson, B. Varnestig, D. Cline, B. Kotliński, H. Grein, E. Grosse, R. Kulessa, C. Michel, W. Spreng, H. J. Wollersheim, and J. Stachel, "Quadrupole collective properties of ^{114}Cd," *Nuclear Physics A*, vol. 485, no. 2, pp. 327 – 359, 1988.

[113] A. Aprahamian, "The nature of low-lying $K^\pi = 0^+$ bands in nuclei," *Physics of Atomic Nuclei*, vol. 67, no. 9, pp. 1750–1755, 2004.

[114] M. A. J. Mariscotti, G. Scharff-Goldhaber, and B. Buck, "Phenomenological analysis of ground-state bands in even-even nuclei," *Phys. Rev.*, vol. 178, pp. 1864–1886, Feb 1969.

[115] H. Leutwyler, "Energy levels of light quarks confined to a box," *Physics Letters B*, vol. 189, pp. 197 – 202, 1987.

[116] J. M. Román and J. Soto, "Effective field theory approach to ferromagnets and antiferromagnets in crystalline solids," *International Journal of Modern Physics B*, vol. 13, no. 07, pp. 755–789, 1999.

[117] C. P. Hofmann, "Spin-wave scattering in the effective lagrangian perspective," *Phys. Rev. B*, vol. 60, pp. 388–405, Jul 1999.

[118] F. Kämpfer, M. Moser, and U.-J. Wiese, "Systematic low-energy effective theory for magnons and charge carriers in an antiferromagnet," *Nuclear Physics B*, vol. 729, no. 3, pp. 317 – 360, 2005.

[119] T. Brauner, "Spontaneous symmetry breaking and Nambu-Goldstone bosons in quantum many-body systems," *Symmetry*, vol. 2, no. 2, pp. 609–657, 2010.

[120] G. Scharff-Goldhaber, C. B. Dover, and A. L. Goodman, "The variable moment of inertia (VMI) model and theories of nuclear collective motion," *Annual Review of Nuclear Science*, vol. 26, no. 1, pp. 239–317, 1976.

[121] J. Eisenberg and W. Greiner, *Excitation mechanisms of the nucleus*. Nuclear Theory, New York: North-Holland Pub. Co., 1970.

[122] L. Rothman, I. Gordon, Y. Babikov, A. Barbe, D. C. Benner, P. Bernath, M. Birk, L. Bizzocchi, V. Boudon, L. Brown, A. Campargue, K. Chance, E. Cohen, L. Coudert, V. Devi, B. Drouin, A. Fayt, J.-M. Flaud, R. Gamache, J. Harrison, J.-M. Hartmann, C. Hill, J. Hodges, D. Jacquemart, A. Jolly, J. Lamouroux, R. L. Roy, G. Li, D. Long, O. Lyulin, C. Mackie, S. Massie, S. Mikhailenko, H. Müller, O. Naumenko, A. Nikitin, J. Orphal, V. Perevalov, A. Perrin, E. Polovtseva, C. Richard, M. Smith, E. Starikova, K. Sung, S. Tashkun, J. Tennyson, G. Toon, V. Tyuterev, and G. Wagner, "The hitran2012 molecular spectroscopic database," *Journal of Quantitative Spectroscopy and Radiative Transfer*, vol. 130, no. 0, pp. 4 – 50, 2013.

[123] E. Browne and J. Tuli, "Nuclear data sheets for A = 236," *Nuclear Data Sheets*, vol. 107, no. 10, pp. 2649 – 2714, 2006.

[124] E. Browne and H. Junde, "Nuclear data sheets for A = 174," *Nuclear Data Sheets*, vol. 87, no. 1, pp. 15 – 176, 1999.

[125] D. D. Warner, "Description of $m1$ transitions in deformed even-even nuclei with the interacting boson approximation," *Phys. Rev. Lett.*, vol. 47, pp. 1819–1822, Dec 1981.

[126] F. K. McGowan, "Interacting boson approximation model analysis of $e2$ transition probabilities for transitions in $^{166-170}$Er," *Phys. Rev. C*, vol. 24, pp. 1803–1805, Oct 1981.

[127] C. M. Baglin, "Nuclear data sheets for A = 166," *Nuclear Data Sheets*, vol. 109, no. 5, pp. 1103 – 1382, 2008.

[128] P. Hubert, N. R. Johnson, and E. Eichler, "Lifetime measurements and multiple Coulomb excitation in ^{162}Dy," *Phys. Rev. C*, vol. 17, pp. 622–627, Feb 1978.

[129] C. Reich, "Nuclear data sheets for A = 162," *Nuclear Data Sheets*, vol. 108, no. 9, pp. 1807 – 2034, 2007.

[130] C. Reich, "Nuclear data sheets for A = 154," *Nuclear Data Sheets*, vol. 110, no. 10, pp. 2257 – 2532, 2009.

[131] D. Tonev, A. Dewald, T. Klug, P. Petkov, J. Jolie, A. Fitzler, O. Möller, S. Heinze, P. von Brentano, and R. F. Casten, "Transition probabilities in ^{154}Gd: Evidence for X(5) critical point symmetry," *Phys. Rev. C*, vol. 69, p. 034334, Mar 2004.

[132] N. V. Zamfir, R. F. Casten, M. A. Caprio, C. W. Beausang, R. Krücken, J. R. Novak, J. R. Cooper, G. Cata-Danil, and C. J. Barton, "$B(e2)$ values and phase coexistence in ^{152}Sm," *Phys. Rev. C*, vol. 60, p. 054312, Oct 1999.

[133] N. Pietralla and O. M. Gorbachenko, "Evolution of the "β excitation" in axially symmetric transitional nuclei," *Phys. Rev. C*, vol. 70, p. 011304, Jul 2004.

APPENDICES

A
PROBABILITY DISTRIBUTION FUNCTIONS FOR RESIDUALS

In this Appendix the details on the calculation of the LO and NLO pdfs for the normalized residual (2.30) are provided. In terms of the prior for the expansion coefficients $\mathscr{C}_i$ given the width parameter c, $\mathrm{pr}(\mathscr{C}_i|c)$, and the prior for this parameter, $\mathrm{pr}(c)$, the pdf for the residual is given by [40]

$$p_M\left(\Delta|\mathscr{C}_n\right) = \frac{\int_0^\infty dc\, p_M(\Delta|c)\left[\prod_n^k \mathrm{pr}(\mathscr{C}_n|c)\right]\mathrm{pr}(c)}{\int_0^\infty dc\left[\prod_n^k \mathrm{pr}(\mathscr{C}_n|c)\right]\mathrm{pr}(c)}, \tag{A.1}$$

where

$$p_M(\Delta|c) = \int_{-\infty}^{\infty}\left[\prod_{m=k+1}^{k+M} d\mathscr{C}_m\,\mathrm{pr}(\mathscr{C}_m|c)\right]\delta\left(\Delta - \Delta_k^{(M)}\right), \tag{A.2}$$

$n \leq k$ are the known coefficients, and

$$\Delta_k^{(M)} = \sum_{m=k+1}^{k+M} \mathscr{C}_m Q^m \tag{A.3}$$

is the residual for an observable. Here, Q is the small expansion parameter.

As discussed in Chapter 2, a log-normal pdf for c [40]

$$\mathrm{pr}(c) = \frac{1}{\sqrt{2\pi}Rc} e^{-\frac{\log^2 c}{2R^2}}, \tag{A.4}$$

where R is the width of this distribution, is consistent with the expectation for the coefficients $\mathscr{C}_i$ to be of order one. In what follows, we calculate the pdf (A.1) given a hard wall prior

$$\mathrm{pr}(\mathscr{C}_i|c) = \frac{1}{2c}\Theta\left(c - |\mathscr{C}_i|\right), \tag{A.5}$$

where $\Theta(x)$ is the Heaviside function, and a Gaussian prior

$$\mathrm{pr}(\mathscr{C}_i|c) = \frac{1}{\sqrt{2\pi}sc} e^{-\frac{\mathscr{C}_i^2}{2s^2c^2}}, \tag{A.6}$$

where s is a scale factor, for the coefficients $\mathscr{C}_i$.

A.1 Leading order probability distribution

As mentioned in Chapter 2, the LO coefficient has a sharp (or delta function) distribution. At such order, no other expansion coefficient is known. From here, the denominator in the pdf (A.1) is one.

A.1.1 Hard wall prior

If only the first term of the residual is taken into account, that is, for $M = 1$, its pdf takes the form

$$\begin{aligned} p_1(\Delta) &= \int_0^\infty dc\, \mathrm{pr}(c) \int_{-\infty}^\infty d\mathscr{C}_{k+1}\, \mathrm{pr}(\mathscr{C}_{k+1}|c)\delta\left(\Delta - \mathscr{C}_{k+1}Q^{k+1}\right) \\ &= \frac{1}{Q^{k+1}} \int_0^\infty dc\, \mathrm{pr}(c)\mathrm{pr}(\Delta/Q^{k+1}|c). \end{aligned} \tag{A.7}$$

Inserting the hard wall prior for the expansion coefficients (A.5) into (A.7) yields the following pdf for the residual

$$\begin{aligned} p_1^{(\mathrm{hw})}(\Delta) &= \frac{1}{\sqrt{8\pi}RQ^{k+1}} \int_0^\infty dc\, \frac{e^{-\frac{\log^2 c}{2R^2}}}{c^2} \Theta\left(c - |\Delta/Q^{k+1}|\right) \\ &= \frac{1}{\sqrt{8\pi}RQ^{k+1}} \int_{\Delta/Q^{k+1}}^\infty dc\, \frac{e^{-\frac{\log^2 c}{2R^2}}}{c^2} \\ &= \frac{1}{\sqrt{8\pi}RQ^{k+1}} \int_{\log(\Delta/Q^{k+1})}^\infty du\, e^{-u} e^{-\frac{u^2}{2R^2}} \\ &= \frac{e^{\frac{R^2}{2}}}{\sqrt{8\pi}RQ^{k+1}} \int_{\log(\Delta/Q^{k+1})}^\infty du\, e^{-\left(\frac{u}{\sqrt{2}R} + \frac{R}{\sqrt{2}}\right)^2} \\ &= \frac{e^{\frac{R^2}{2}}}{\sqrt{4\pi}Q^{k+1}} \int_{\frac{R}{\sqrt{2}}\left[1 + \frac{\log(\Delta/Q^{k+1})}{R^2}\right]}^\infty dx\, e^{-x^2} \\ &= \frac{e^{\frac{R^2}{2}}}{4Q^{k+1}} \left[1 - \Phi\left(\frac{R}{\sqrt{2}}\left[1 + \frac{\log(\Delta/Q^{k+1})}{R^2}\right]\right)\right], \end{aligned} \tag{A.8}$$

where $\Phi(x)$ is the error function. In order to reach the final expression in Equation (A.8), the change of variables $u = \log c$ and $x = (u/R + R)/\sqrt{2}$ were employed.

A.1.2 Gaussian prior

If other terms of the residual are taken into account, its pdf takes the form

$$\begin{aligned} p_M(\Delta) &= \int_0^\infty dc\, \mathrm{pr}(c) \int_{-\infty}^\infty \left[\prod_{m=k+1}^{k+M} d\mathscr{C}_m\, \mathrm{pr}(\mathscr{C}_m|c)\right] \delta\left(\Delta - \sum_{m=k+1}^{k+M} \mathscr{C}_m Q^m\right) \\ &= \frac{1}{2\pi} \int_0^\infty dc\, \mathrm{pr}(c) \int_{-\infty}^\infty \left[\prod_{m=k+1}^{k+M} d\mathscr{C}_m\, \mathrm{pr}(\mathscr{C}_m|c)\right] \int_{-\infty}^\infty dt\, e^{it\left(\Delta - \sum_{m=k+1}^{k+M} \mathscr{C}_m Q^m\right)} \\ &= \frac{1}{2\pi} \int_0^\infty dc\, \mathrm{pr}(c) \int_{-\infty}^\infty dt\, e^{it\Delta} \int_{-\infty}^\infty \left[\prod_{m=k+1}^{k+M} d\mathscr{C}_m\, e^{-it\mathscr{C}_m Q^m} \mathrm{pr}(\mathscr{C}_m|c)\right], \end{aligned} \tag{A.9}$$

where the delta function $\delta(x)$ has been written as a Fourier integral in order to facilitate the following calculations.

Inserting the Gaussian prior for the expansion coefficients (A.6) into (A.9) yields the following pdf for the residual

$$\begin{aligned} p_M^{(\mathrm{G})}(\Delta) &= \frac{1}{2\pi R s^M} \int_0^\infty dc\, \frac{e^{-\frac{\log^2 c}{2R^2}}}{\left(\sqrt{2\pi}c\right)^{M+1}} \int_{-\infty}^\infty dt\, e^{it\Delta} \int_{-\infty}^\infty \left[\prod_{m=k+1}^{k+M} d\mathscr{C}_m\, e^{-it\mathscr{C}_m Q^m} e^{-\frac{\mathscr{C}_m^2}{2s^2c^2}}\right] \\ &= \frac{1}{2\pi R s^M} \int_0^\infty dc\, \frac{e^{-\frac{\log^2 c}{2R^2}}}{\left(\sqrt{2\pi}c\right)^{M+1}} \int_{-\infty}^\infty dt\, e^{it\Delta} e^{-\frac{t^2 s^2 c^2 q^2}{2}} \int_{-\infty}^\infty \left[\prod_{m=k+1}^{k+M} d\mathscr{C}_m\, e^{-\left(\frac{\mathscr{C}_m}{\sqrt{2}sc} + \frac{itscQ^m}{\sqrt{2}}\right)^2}\right] \\ &= \frac{1}{\sqrt{8\pi^3}R} \int_0^\infty dc\, \frac{e^{-\frac{\log^2 c}{2R^2}}}{c} \int_{-\infty}^\infty dt\, e^{it\Delta} e^{-\frac{t^2 s^2 c^2 q^2}{2}} \\ &= \frac{1}{\sqrt{8\pi^3}R} \int_0^\infty dc\, \frac{e^{-\frac{\log^2 c}{2R^2}}}{c} e^{-\frac{\Delta^2}{2s^2c^2q^2}} \int_{-\infty}^\infty dt\, e^{-\left(\frac{tscq}{\sqrt{2}} - \frac{i\Delta}{\sqrt{2}scq}\right)^2} \\ &= \frac{1}{2\pi R s q} \int_0^\infty dc\, \frac{e^{-\frac{\log^2 c}{2R^2}}}{c^2} e^{-\frac{\Delta^2}{2s^2c^2q^2}} \\ &= \frac{1}{2\pi R s q} \int_0^\infty dx\, e^{-\frac{\log^2 x}{2R^2}} e^{-\frac{\Delta^2 x^2}{2s^2q^2}}, \end{aligned} \tag{A.10}$$

where $q^2 \equiv \sum_{m=k+1}^{k+M} Q^{2m}$. In order to reach the final expression in Equation (A.10), the change of variables $x = 1/c$ was employed. This pdf takes can easily take into account as many terms in the expansion for the residual as desired.

A.2 Next-to-leading order probability distribution

At NLO, the numerator and denominator of the pdf for the residual (A.1), denoted by $\mathcal{N}$ and $\mathcal{D}$, respectively, take the form

$$\mathcal{N} = \int_0^\infty dc\, p_M(\Delta|c)\mathrm{pr}(\mathscr{C}_k|c)\mathrm{pr}(c), \tag{A.11}$$

and

$$\mathcal{D} = \int_0^\infty dc\, \mathrm{pr}(\mathscr{C}_k|c)\mathrm{pr}(c), \tag{A.12}$$

where $\mathscr{C}_k$ is the NLO expansion coefficient.

A.2.1 Hard wall prior

If only the first term of the residual is taken into account, and the hard wall prior (A.5) is inserted into the expressions for the numerator (A.11) and the denominator (A.12) of the pdf for the residual one gets

$$\begin{aligned}\mathcal{N} &= \frac{1}{\sqrt{32\pi}RQ^{k+1}}\int_0^\infty dc\, \frac{e^{-\frac{\log^2 c}{2R^2}}}{c^3}\Theta\left(c - |\Delta/Q^{k+1}|\right)\Theta\left(c - |\mathscr{C}_k|\right) \\ &= \frac{e^{\frac{4R^2}{2}}}{8Q^{k+1}}\left[1 - \Phi\left(\frac{R}{\sqrt{2}}\left[2 + \frac{\log\kappa}{R^2}\right]\right)\right],\end{aligned} \tag{A.13}$$

where $\kappa \equiv \max(|\mathscr{C}_k|, \Delta/Q^{k+1})$. For the denominator one finds

$$\begin{aligned}\mathcal{D} &= \frac{1}{\sqrt{8\pi}R}\int_0^\infty dc\, \frac{e^{-\frac{\log^2 c}{2R^2}}}{c^2}\Theta\left(c - |\mathscr{C}_k|\right) \\ &= \frac{e^{\frac{R^2}{2}}}{4}\left[1 - \Phi\left(\frac{R}{\sqrt{2}}\left[1 + \frac{\log|\mathscr{C}_k|}{R^2}\right]\right)\right].\end{aligned} \tag{A.14}$$

The procedure to calculate $\mathcal{N}$ and $\mathcal{D}$ assuming a hard wall prior for the expansion coefficients is analogous to that employed to calculate the pdf (A.8).

Combining these expressions, one finds that

$$p_1^{(\mathrm{hw})}(\Delta|\mathscr{C}_k) = \frac{e^{3R^2}}{2Q^{k+1}}\frac{1 - \Phi\left(\frac{R}{\sqrt{2}}\left[2 + \frac{\log\kappa}{R^2}\right]\right)}{1 - \Phi\left(\frac{R}{\sqrt{2}}\left[1 + \frac{\log|\mathscr{C}_k|}{R^2}\right]\right)}. \tag{A.15}$$

A.2.2 Gaussian prior

If more terms of the residual are taken into account, and the Gaussian prior (A.6) is inserted into the numerator (A.11) and denominator (A.12) of the pdf for the residual one gets

$$\begin{aligned}\mathcal{N} &= \frac{1}{2\pi R s^{M+1}} \int_0^\infty dc\, \frac{e^{-\frac{\log^2 c}{2R^2}} e^{-\frac{\mathscr{C}_k^2}{2s^2c^2}}}{\left(\sqrt{2\pi}c\right)^{M+2}} \int_{-\infty}^{\infty} dt\, e^{it\Delta} \int_{-\infty}^{\infty} \left[\prod_{m=k+1}^{k+M} d\mathscr{C}_m\, e^{-it\mathscr{C}_m Q^m} e^{-\frac{\mathscr{C}_m^2}{2s^2c^2}}\right] \\ &= \frac{1}{\sqrt{8\pi^3} R s^2 q} \int_0^\infty dx\, x e^{-\frac{\log^2 x}{2R^2}} e^{-\frac{\left(\mathscr{C}_k^2 + \Delta^2/q^2\right)x^2}{2s^2}}\end{aligned} \tag{A.16}$$

and

$$\begin{aligned}\mathcal{D} &= \frac{1}{2\pi R s} \int_0^\infty dc\, \frac{e^{-\frac{\log^2 c}{2R^2}} e^{-\frac{\mathscr{C}_k^2}{2s^2c^2}}}{c^2} \\ &= \frac{1}{2\pi R s} \int_0^\infty dx\, e^{-\frac{\log^2 x}{2R^2}} e^{-\frac{\mathscr{C}_k^2 x^2}{2s^2}}.\end{aligned} \tag{A.17}$$

Combining these expressions, one finds that

$$p_M^{(\mathrm{G})}(\Delta|\mathscr{C}_k) = \frac{\int_0^\infty dx\, x e^{-\frac{\log^2 x}{2R^2}} e^{-\frac{\left(\mathscr{C}_k^2 + \Delta^2/q^2\right)x^2}{2s^2}}}{\sqrt{2\pi} s q \int_0^\infty dx\, e^{-\frac{\log^2 x}{2R^2}} e^{-\frac{\mathscr{C}_k^2 x^2}{2s^2}}}. \tag{A.18}$$

B
TOY MODEL: SPHERICAL SURFACE WITH QUADRUPOLE VIBRATIONS

In order to gain insight on how to couple the quadrupole DOF, and consequently the phonon operators, to an electromagnetic field with vector potential $\mathbf{A}$, the following toy model is studied. Assume an infinite number of particles lie on a spherical surface of radius R_0. If the surface undergoes small quadrupole oscillations, the surface density of particles is approximately uniform at all times, and the position and velocity of each particle may be written as

$$\begin{aligned} \mathbf{R}(\theta,\phi) &= R_0\left[1+\sum_\mu \alpha_\mu Y_{2\mu}(\theta,\phi)\right]\mathbf{e}_r \\ \mathbf{v}(\theta,\phi) &= R_0\sum_\mu \dot{\alpha}_\mu Y_{2\mu}(\theta,\phi)\mathbf{e}_r, \end{aligned} \tag{B.1}$$

where the condition $\alpha_\mu = (-1)^\mu \alpha^*_{-\mu}$ needs to be fulfilled by the α coordinates for $\mathbf{R}(\theta,\phi)$ to be real [22]. Notice that the angles θ and ϕ indicate the orientation of a particle with respect to the laboratory reference frame. This orientation is time-independent for small quadrupole oscillations.

For a uniform mass density $m = M/A$, where M and A are the total mass and surface area A of the system respectively, the kinetic energy of the system is

$$\begin{aligned} T &= \frac{1}{2}\int d\Omega m R_0^2 \left(\sum_\mu \dot{\alpha}_\mu Y_{2\mu}(\theta,\phi)\right)^2 \\ &= \frac{1}{2} m R_0^2 \sum_\mu |\dot{\alpha}_\mu|^2. \end{aligned} \tag{B.2}$$

If each particle is trapped in a quadratic potential $dV = \kappa[R(\theta,\phi)-R_0]^2/2$, the potential energy of the system is

$$\begin{aligned} V &= \frac{1}{2}\int d\Omega \kappa R_0^2 \left(\sum_\mu \alpha_\mu Y_{2\mu}(\theta,\phi)\right)^2 \\ &= \frac{1}{2}\kappa R_0^2 \sum_\mu |\alpha_\mu|^2. \end{aligned} \tag{B.3}$$

Thus, the Hamiltonian of the system $H_{\rm TM} = T + V$ is equivalent to the harmonic vibrator submodel of the Bohr collective model, implying such system can be described within the EFT for nuclear vibrations.

Let the surface have a uniform charge density $q = Q/A$, where Q is the total charge of the system. If we couple an electromagnetic field with vector potential $\mathbf{A}$ to the system, the coupling term in the Lagrangian takes the form

$$\begin{aligned} L_{\rm EM} =& \int d\Omega q \mathbf{v}(\theta,\phi)\cdot\mathbf{A}(\theta,\phi) \\ =& qR_0 \int d\Omega \sum_\mu \dot{\alpha}_\mu Y_{2\mu}(\theta,\phi) A_r(\theta,\phi). \end{aligned} \tag{B.4}$$

In order to make progress, let us employ a plane wave vector potential of the form $\mathbf{A} = -iAe^{ikx}\mathbf{e}_z$, which radial component can approximately be written as

$$\begin{aligned} A_r(\theta,\phi) \approx& -i\sqrt{\frac{4\pi}{3}} A\left[1 + ikx(\theta,\phi)\right] Y_{10}(\theta,\phi) \\ \approx& -i\sqrt{\frac{4\pi}{3}} A Y_{10}(\theta,\phi) + \sqrt{\frac{2\pi}{15}} AkR_0 \left[Y_{2-1}(\theta,\phi) - Y_{21}(\theta,\phi)\right], \end{aligned} \tag{B.5}$$

where the value of $\mathbf{A}$ at R_0 has been employed since the electromagnetic field does not change considerably with r within the domain of the small oscillations. In the long wavelength limit $kr \ll 1$, the correction to this expression is of order $\mathcal{O}(k^2r^2)$.

Inserting this expression for the radial component of the vector potential into the coupling term (B.4) leads to

$$\begin{aligned} L_{\rm EM} &= q\sqrt{\frac{2\pi}{15}} AkR_0^2(\dot{\alpha}_{-1} - \dot{\alpha}_1) \\ &= q\dot{\alpha}\cdot\mathcal{A}, \end{aligned} \tag{B.6}$$

where $\mathcal{A}$ is defined as a spherical tensor of rank two defined by

$$\mathcal{A}_{\pm1} = \mp\sqrt{\frac{2\pi}{15}} AkR_0^2, \qquad \mathcal{A}_{\pm2} = 0 = \mathcal{A}_0. \tag{B.7}$$

Thus, the quadrupole DOF can be minimally coupled to an electromagnetic field via the gauging

$$\pi_\mu \to \pi_\mu - q\mathcal{A}_\mu, \tag{B.8}$$

where π_μ with $\mu = \pm2, \pm1, 0$ is the momenta conjugate to α_μ.

C
MATRIX ELEMENTS OF THE LO INTERBAND INTERACTION

C.1 Interactions from the β band to the ground band

The LO interband interaction operator coupling states in the β band to states in the ground band is

$$\hat{H}^{(\mathbf{A})}_{\mathrm{NNLO}} = i\frac{q}{2C_0}\frac{C_\beta}{C_0}\psi_0\left(\nabla_{\Omega\gamma}\cdot\mathbf{A}_\Omega + \mathbf{A}_\Omega\cdot\nabla_{\Omega\gamma}\right). \tag{C.1}$$

In this section we calculate the matrix elements of this interband interaction between initial states in the β band and final states in the ground band. These matrix elements are

$$\begin{aligned}\langle f|\hat{H}^{(\mathbf{A})}_{\mathrm{NNLO}}|i\rangle =& \frac{C_\beta}{C_0}\langle n_{0f}|\psi_0|n_{0i}\rangle\langle n_{2f}|n_{2i}\rangle \\ &\times i\frac{q}{2C_0}\langle I_f M_f K_f|\left(\nabla_{\Omega\gamma}\cdot\mathbf{A}_\Omega + \mathbf{A}_\Omega\cdot\nabla_{\Omega\gamma}\right)|I_i M_i K_i\rangle \\ =& \frac{C_\gamma}{C_0}\langle n_{0f}|\psi_0|n_{0i}\rangle i\frac{q}{2C_0}\langle I_f M_f K_f|\left(\nabla_{\Omega\gamma}\cdot\mathbf{A}_\Omega + \mathbf{A}_\Omega\cdot\nabla_{\Omega\gamma}\right)|I_i M_i K_i\rangle,\end{aligned} \tag{C.2}$$

where the matrix element $\langle n_{2f}|n_{2i}\rangle = 1$ due to the conditions $n_{2f} = n_{2i}$ and $K_f = K_i$.

C.1.1 Vibrational matrix elements

To calculate the matrix elements of ψ_0 operator we write it in terms of the creation and annihilation operators for the harmonic oscillator, defined by

$$\hat{a}^\dagger|n_0\rangle = \sqrt{n_0+1}|n_0+1\rangle, \qquad \hat{a}|n_0\rangle = \sqrt{n}|n_0-1\rangle, \tag{C.3}$$

as

$$\psi_0 = \sqrt{\frac{1}{2\omega_0}}\left(\hat{a}^\dagger + \hat{a}\right). \tag{C.4}$$

The matrix elements take the form

$$\langle n_{0f}|\psi_0|n_{0i}\rangle = \sqrt{\frac{1}{2\omega_0}}. \tag{C.5}$$

C.1.2 Angular matrix elements

When the quadrupole component of the vector potential is employed in the calculation of the angular matrix elements in Equation (C.2), they are equivalent to those of the LO inband quadrupole interaction (3.89). Thus, the matrix elements of the LO interband interaction from a state the β band to a state in the ground band are

$$\langle f|\hat{H}^{(\mathbf{A})}_{\mathrm{NNLO}}|i\rangle = \sqrt{\frac{1}{2\omega_0}}\frac{C_\beta}{C_0}M(E2, i \to f). \tag{C.6}$$

C.2 Interactions from the γ band to the ground band

The LO interaction coupling states in the γ band to states in the ground band is

$$\hat{H}^{(\mathbf{A})}_{\mathrm{NNLO}} = i\frac{q}{2C_0}\frac{C_\gamma}{C_0}\psi_2\left(\nabla^T_{\Omega\gamma}\hat{\Gamma}\mathbf{A}_\Omega + \mathbf{A}_\Omega\hat{\Gamma}\nabla_{\Omega\gamma}\right). \tag{C.7}$$

In this section we calculate the matrix elements of this interband interaction between initial states in the γ band and final states in the ground band. These matrix elements are

$$\begin{aligned}\langle f|\hat{H}^{\mathbf{A}}_{\mathrm{NNLO}}|i\rangle =& \frac{C_\gamma}{C_0}\langle n_{0f}|n_{0i}\rangle\langle n_{2f}|\psi_2|n_{2i}\rangle \\ &\times i\frac{q}{2C_0}\langle I_f M_f K_f|\left(\nabla_{\Omega\gamma}\cdot\mathbf{A}_\Gamma + \mathbf{A}_\Gamma\cdot\nabla_{\Omega\gamma}\right)|I_i M_i K_i\rangle \\ =& \frac{C_\gamma}{C_0}\langle n_{2f}|\psi_2|n_{2i}\rangle i\frac{q}{2C_0}\langle I_f M_f K_f|\left(\nabla_{\Omega\gamma}\cdot\mathbf{A}_\Gamma + \mathbf{A}_\Gamma\cdot\nabla_{\Omega\gamma}\right)|I_i M_i K_i\rangle,\end{aligned} \tag{C.8}$$

where $\mathbf{A}_\Gamma \equiv \hat{\Gamma}\mathbf{A}$, and the matrix element $\langle n_{0f}|n_{0i}\rangle = 1$ due to the condition $n_{0f} = n_{0i}$.

C.2.1 Vibrational matrix elements

The ψ_2-dependent factor of the wave function is equivalent to the radial wave function of a 2-dimensional harmonic oscillator with frequency ω_2. For states in the ground and γ bands these radial wave functions are

$$\begin{aligned}\langle\psi_2|n_2 = 0\,(K/2 = 0)\rangle &= \left(\frac{4\omega_2}{\pi}\right)^{1/4} e^{-\omega_2\psi_2^2/2}, \\ \langle\psi_2|n_2 = 0\,(K/2 = 1)\rangle &= \left(\frac{16\omega_2}{\pi}\right)^{1/4} \psi_2 e^{-\omega_2\psi_2^2/2}.\end{aligned} \tag{C.9}$$

Thus, the matrix elements of ψ_2 in Equation (C.8) are given by

$$\langle n_{2f}|\psi_2|n_{2i}\rangle = \sqrt{\frac{1}{2\omega_2}}. \tag{C.10}$$

C.2.2 Angular matrix elements

In order to calculate the angular matrix elements in Equation (C.8), we recall that the components of the angular momentum in the tangent plane operator $-i\nabla_{\Omega\gamma} = \hat{\mathbf{p}}_{\Omega\gamma}$ act on the Wigner D-function as follows

$$\begin{aligned}
\hat{p}_\theta D^I_{MK} =& -i\sqrt{\frac{I(I+1)}{2}}\left(e^{-i\gamma}C^{IK-1}_{IK1-1}D^I_{MK-1} + e^{i\gamma}C^{IK+1}_{IK11}D^I_{MK+1}\right), \\
\hat{p}_{\phi\gamma} D^I_{MK} =& \sqrt{\frac{I(I+1)}{2}}\left(e^{-i\gamma}C^{IK-1}_{IK1-1}D^I_{MK-1} - e^{i\gamma}C^{IK+1}_{IK11}D^I_{MK+1}\right).
\end{aligned} \tag{C.11}$$

Also we write the quadrupole component of the vector potential in terms of Wigner D-functions as

$$\begin{aligned}
\mathbf{A}^{(2)} =& AkR\sin\theta\cos\phi\cos\theta\mathbf{e}_r - AkR\sin\theta\cos\phi\sin\theta\mathbf{e}_\theta \\
=& \frac{AkR}{\sqrt{2}}\left(D^1_{-10} - D^1_{10}\right)D^1_{00}\mathbf{e}_r + \frac{AkR}{2}\left(D^1_{-10} - D^1_{10}\right)\left(e^{-i\gamma}D^1_{0-1} - e^{\imath\gamma}D^1_{01}\right)\mathbf{e}_\theta \\
=& -\frac{AkR}{4}\Big[e^{-i\gamma}\left(D^1_{-1-1} - D^2_{-1-1} + D^1_{1-1} + D^2_{1-1}\right) \\
&+ e^{i\gamma}\left(D^1_{-11} + D^2_{-11} + D^1_{11} - D^2_{11}\right)\Big]\mathbf{e}_\theta + \frac{AkR}{\sqrt{6}}\left(D^2_{-10} - D^2_{10}\right)\mathbf{e}_r,
\end{aligned} \tag{C.12}$$

where the product of 2 Wigner D-functions was expanded in a Clebsch-Gordan series [50]

$$D^{I_1}_{M_1K_1}D^{I_2}_{M_2K_2} = \sum_I C^{IM}_{I_1M_1I_2M_2}C^{IK}_{I_1K_1I_2K_2}D^I_{MK}, \tag{C.13}$$

with $|I_1 - I_2| \leq I \leq I_1 + I_2$, $M = M_1 + M_2$ and $K = K_1 + K_2$. In the following calculations we employ the quadrupole component of the vector potential.

We start by writing the operator $i\mathbf{A}_\Gamma \cdot \nabla_{\Omega\gamma}$ as

$$-\mathbf{A}_\Gamma \cdot (-i\nabla_{\Omega\gamma}) = -A_{\Gamma\theta}\hat{p}_\theta - A_{\Gamma\phi}\hat{p}_{\phi\gamma}, \tag{C.14}$$

where $A_{\Gamma\theta}$ and $A_{\Gamma\phi}$ are the tangential components of $\mathbf{A}_\Gamma$. The matrix elements of

the first and second terms on right side of Equation (C.14) take the form

$$\begin{aligned}
\langle f|A_{\Gamma\theta}\hat{p}_\theta|i\rangle &= \frac{iAkR}{8}\sqrt{\frac{(2I_i+1)(2I_f+1)}{32\pi^4}}\sqrt{\frac{I_i(I_i+1)}{2}}\int d\Omega d\gamma D^{I_f*}_{M_f0} \\
&\left[e^{-i\gamma}\left(D^1_{-1-1}-D^2_{-1-1}+D^1_{1-1}+D^2_{1-1}\right)+e^{i\gamma}\left(D^1_{-11}+D^2_{-11}+D^1_{11}-D^2_{11}\right)\right]\left(e^{i2\gamma}+e^{-i2\gamma}\right) \\
&\left[e^{-i\gamma}C^{I_i1}_{I_i21-1}D^{I_i}_{M_i1}+e^{i\gamma}C^{I_i3}_{I_i211}D^{I_i}_{M_i3}-(-1)^{I_i}e^{-i\gamma}C^{I_i3}_{I_i211}D^{I_i}_{M_i-3}-(-1)^{I_i}e^{i\gamma}C^{I_i1}_{I_i21-1}D^{I_i}_{M_i-1}\right] \\
&= \frac{iAkR}{8}\sqrt{\frac{(2I_i+1)(2I_f+1)}{32\pi^4}}\sqrt{\frac{I_i(I_i+1)}{2}}C^{I_i1}_{I_i21-1}\int d\Omega d\gamma D^{I_f*}_{M_f0} \\
&\Big\{\left[\left(D^1_{-1-1}-D^2_{-1-1}+D^1_{1-1}+D^2_{1-1}\right)+e^{i2\gamma}\left(D^1_{-11}+D^2_{-11}+D^1_{11}-D^2_{11}\right)\right]D^{I_i}_{M_i1} \\
&-(-1)^{I_i}\left[e^{-i2\gamma}\left(D^1_{-1-1}-D^2_{-1-1}+D^1_{1-1}+D^2_{1-1}\right)+\left(D^1_{-11}+D^2_{-11}+D^1_{11}-D^2_{11}\right)\right]D^{I_i}_{M_i-1}\Big\} \\
&+\frac{iAkR}{8}\sqrt{\frac{(2I_i+1)(2I_f+1)}{32\pi^4}}\sqrt{\frac{I_i(I_i+1)}{2}}C^{I_i3}_{I_i211}\int d\Omega d\gamma D^{I_f*}_{M_f0} \\
&\Big\{\left[e^{i2\gamma}\left(D^1_{-1-1}-D^2_{-1-1}+D^1_{1-1}+D^2_{1-1}\right)+e^{i4\gamma}\left(D^1_{-11}+D^2_{-11}+D^1_{11}-D^2_{11}\right)\right]D^{I_i}_{M_i3} \\
&-(-1)^{I_i}\left[e^{-i4\gamma}\left(D^1_{-1-1}-D^2_{-1-1}+D^1_{1-1}+D^2_{1-1}\right)+e^{-i2\gamma}\left(D^1_{-11}+D^2_{-11}+D^1_{11}-D^2_{11}\right)\right]D^{I_i}_{M_i-3}\Big\}
\end{aligned} \tag{C.15}$$

$$\begin{aligned}
&= \frac{iAkR}{8}\sqrt{\frac{(2I_i+1)(2I_f+1)}{32\pi^4}}\sqrt{\frac{I_i(I_i+1)}{2}}C^{I_i1}_{I_i21-1}\int d\Omega d\gamma D^{I_f*}_{M_f0} \\
&\Big\{\left[\left(D^1_{-1-1}-D^2_{-1-1}+D^1_{1-1}+D^2_{1-1}\right)+e^{i2\phi}\left(D^1_{1-1}+D^2_{1-1}\right)+e^{-i2\phi}\left(D^1_{-1-1}-D^2_{-1-1}\right)\right]D^{I_i}_{M_i1} \\
&-(-1)^{I_i}\left[e^{i2\phi}\left(D^1_{11}-D^2_{11}\right)+e^{-i2\phi}\left(D^1_{-11}+D^2_{-11}\right)+\left(D^1_{-11}+D^2_{-11}+D^1_{11}-D^2_{11}\right)\right]D^{I_i}_{M_i-1}\Big\} \\
&+\frac{iAkR}{8}\sqrt{\frac{(2I_i+1)(2I_f+1)}{32\pi^4}}\sqrt{\frac{I_i(I_i+1)}{2}}C^{I_i3}_{I_i211}\int d\Omega d\gamma D^{I_f*}_{M_f0} \\
&\Big\{\left[e^{i2\gamma}\left(D^1_{-1-1}-D^2_{-1-1}+D^1_{1-1}+D^2_{1-1}\right)+e^{i4\gamma}\left(D^1_{-11}+D^2_{-11}+D^1_{11}-D^2_{11}\right)\right]D^{I_i}_{M_i3} \\
&-(-1)^{I_i}\left[e^{-i4\gamma}\left(D^1_{-1-1}-D^2_{-1-1}+D^1_{1-1}+D^2_{1-1}\right)+e^{-i2\gamma}\left(D^1_{-11}+D^2_{-11}+D^1_{11}-D^2_{11}\right)\right]D^{I_i}_{M_i-3}\Big\}
\end{aligned}$$

and

$$\begin{aligned}
\langle f|A_{\Gamma\phi}\hat{p}_{\phi\gamma}|i\rangle &= \frac{iAkR}{8}\sqrt{\frac{(2I_i+1)(2I_f+1)}{32\pi^4}}\sqrt{\frac{I_i(I_i+1)}{2}}\int d\Omega d\gamma D^{I_f*}_{M_f0} \\
&\left[e^{-i\gamma}\left(D^1_{-1-1}-D^2_{-1-1}+D^1_{1-1}+D^2_{1-1}\right)+e^{i\gamma}\left(D^1_{-11}+D^2_{-11}+D^1_{11}-D^2_{11}\right)\right]\left(e^{i2\gamma}-e^{-i2\gamma}\right) \\
&\left[e^{-i\gamma}C^{I_i1}_{I_i21-1}D^{I_i}_{M_i1}-e^{i\gamma}C^{I_i3}_{I_i211}D^{I_i}_{M_i3}-(-1)^{I_i}e^{-i\gamma}C^{I_i3}_{I_i211}D^{I_i}_{M_i-3}+(-1)^{I_i}e^{i\gamma}C^{I_i1}_{I_i21-1}D^{I_i}_{M_i-1}\right] \\
&= \frac{iAkR}{8}\sqrt{\frac{(2I_i+1)(2I_f+1)}{32\pi^4}}\sqrt{\frac{I_i(I_i+1)}{2}}C^{I_i1}_{I_i21-1}\int d\Omega d\gamma D^{I_f*}_{M_f0} \\
&\Big\{\left[\left(D^1_{-1-1}-D^2_{-1-1}+D^1_{1-1}+D^2_{1-1}\right)+e^{i2\phi}\left(D^1_{1-1}+D^2_{1-1}\right)+e^{-i2\phi}\left(D^1_{-1-1}-D^2_{-1-1}\right)\right]D^{I_i}_{M_i1} \\
&-(-1)^{I_i}\left[e^{i2\phi}\left(D^1_{11}-D^2_{11}\right)+e^{-i2\phi}\left(D^1_{-11}+D^2_{-11}\right)+\left(D^1_{-11}+D^2_{-11}+D^1_{11}-D^2_{11}\right)\right]D^{I_i}_{M_i-1}\Big\} \\
&-\frac{iAkR}{8}\sqrt{\frac{(2I_i+1)(2I_f+1)}{32\pi^4}}\sqrt{\frac{I_i(I_i+1)}{2}}C^{I_i3}_{I_i211}\int d\Omega d\gamma D^{I_f*}_{M_f0} \\
&\Big\{\left[e^{i2\gamma}\left(D^1_{-1-1}-D^2_{-1-1}+D^1_{1-1}+D^2_{1-1}\right)+e^{i4\gamma}\left(D^1_{-11}-D^2_{-11}+D^1_{11}+D^2_{11}\right)\right]D^{I_i}_{M_i3} \\
&-(-1)^{I_i}\left[e^{-i4\gamma}\left(D^1_{-1-1}-D^2_{-1-1}+D^1_{1-1}+D^2_{1-1}\right)+e^{-i2\gamma}\left(D^1_{-11}+D^2_{-11}+D^1_{11}-D^2_{11}\right)\right]D^{I_i}_{M_i-3}\Big\}
\end{aligned} \tag{C.16}$$

where the identity [50]

$$D^I_{MK} = (-1)^{K-M} e^{-i2M\phi - i2K\gamma} D^I_{-M-K} \tag{C.17}$$

has been used to write some terms in a convenient form.

Combining the matrix elements (C.15) and (C.16) yields

$$\begin{aligned} i\langle f|\mathbf{A}_\Gamma \cdot \nabla_{\Omega\gamma}|i\rangle = &-\frac{iAkR}{4}\sqrt{\frac{(2I_i+1)(2I_f+1)}{32\pi^4}}\sqrt{\frac{I_i(I_i+1)}{2}} C^{I_i 1}_{I_i 21-1} \int d\Omega d\gamma D^{I_f *}_{M_f 0} \\ &\Big\{ \left[\left(D^1_{-1-1} - D^2_{-1-1} + D^1_{1-1} + D^2_{1-1}\right) + e^{i2\phi}\left(D^1_{1-1} + D^2_{1-1}\right) + e^{-i2\phi}\left(D^1_{-1-1} - D^2_{-1-1}\right)\right] D^{I_i}_{M_i 1} \\ &- (-1)^{I_i}\left[e^{i2\phi}\left(D^1_{11} - D^2_{11}\right) + e^{-i2\phi}\left(D^1_{-11} + D^2_{-11}\right) + \left(D^1_{-11} + D^2_{-11} + D^1_{11} - D^2_{11}\right)\right] D^{I_i}_{M_i -1} \Big\}. \end{aligned} \tag{C.18}$$

The integrals in the matrix elements (C.18) can be evaluated as follows

$$\begin{aligned} &\int d\Omega d\gamma D^{I_f *}_{M_f 0}\left(D^1_{-1-1} - D^2_{-1-1} + D^1_{1-1} + D^2_{1-1}\right) D^{I_i}_{M_i 1} \\ &\quad = \frac{4\pi^2}{2I_f+1}\left[\left(C^{I_f M_f}_{I_i M_i 1-1} + C^{I_f M_f}_{I_i M_i 11}\right) C^{I_f 0}_{I_i 11-1} - \left(C^{I_f M_f}_{I_i M_i 2-1} - C^{I_f M_f}_{I_i M_i 21}\right) C^{I_f 0}_{I_i 12-1}\right], \end{aligned} \tag{C.19}$$

$$\begin{aligned} &\int d\Omega d\gamma D^{I_f *}_{M_f 0} e^{i2\phi}\left(D^1_{1-1} + D^2_{1-1}\right) D^{I_i}_{M_i 1} \\ &\quad = 4\pi^2 \int d\theta \sin\theta d^{I_f}_{M_f 0}\left(d^1_{-1-1} - d^2_{-1-1}\right) d^{I_i}_{M_i 1} \delta^{M_f}_{M_i -1}\delta^0_{1-1} \\ &\quad = \frac{4\pi^2}{2I_f+1}\left(C^{I_f M_f}_{I_i M_i 1-1} C^{I_f 0}_{I_i 11-1} - C^{I_f M_f}_{I_i M_i 2-1} C^{I_f 0}_{I_i 12-1}\right), \end{aligned} \tag{C.20}$$

$$\begin{aligned} &\int d\Omega d\gamma D^{I_f *}_{M_f 0} e^{-i2\phi}\left(D^1_{-1-1} - D^2_{-1-1}\right) D^{I_i}_{M_i 1} \\ &\quad = 4\pi^2 \int d\theta \sin\theta d^{I_f}_{M_f 0}\left(d^1_{1-1} + d^2_{1-1}\right) d^{I_i}_{M_i 1} \delta^{M_f}_{M_i +1}\delta^0_{1-1} \\ &\quad = \frac{4\pi^2}{2I_f+1}\left(C^{I_f M_f}_{I_i M_i 11} C^{I_f 0}_{I_i 11-1} + C^{I_f M_f}_{I_i M_i 21} C^{I_f 0}_{I_i 12-1}\right), \end{aligned} \tag{C.21}$$

$$\begin{aligned} &\int d\Omega d\gamma D^{I_f *}_{M_f 0} e^{i2\phi}\left(D^1_{11} - D^2_{11}\right) D^{I_i}_{M_i -1} \\ &\quad = 4\pi^2 \int d\theta \sin\theta d^{I_f}_{M_f 0}\left(d^1_{-11} + d^2_{-11}\right) d^{I_i}_{M_i -1} \delta^{M_f}_{M_i -1}\delta^0_{-1+1} \\ &\quad = \frac{4\pi^2}{2I_f+1}\left(C^{I_f M_f}_{I_i M_i -11} C^{I_f 0}_{I_i -111} + C^{I_f M_f}_{I_i M_i 2-1} C^{I_f 0}_{I_i -121}\right), \end{aligned} \tag{C.22}$$

$$\begin{aligned} &\int d\Omega d\gamma D^{I_f *}_{M_f 0} e^{-i2\phi}\left(D^1_{-11} + D^2_{-11}\right) D^{I_i}_{M_i -1} \\ &\quad = 4\pi^2 \int d\theta \sin\theta d^{I_f}_{M_f 0}\left(d^1_{11} - d^2_{11}\right) d^{I_i}_{M_i -1} \delta^{M_f}_{M_i +1}\delta^0_{-1+1} \\ &\quad = \frac{4\pi^2}{2I_f+1}\left(C^{I_f M_f}_{I_i M_i 11} C^{I_f 0}_{I_i -111} - C^{I_f M_f}_{I_i M_i 21} C^{I_f 0}_{I_i -121}\right), \end{aligned} \tag{C.23}$$

$$\begin{aligned}&\int d\Omega d\gamma D^{I_f*}_{M_f0}\left(D^1_{-11}+D^2_{-11}+D^1_{11}-D^2_{11}\right)D^{I_i}_{M_i-1}\\&\quad=\frac{4\pi^2}{2I_f+1}\left[\left(C^{I_fM_f}_{I_iM_i1-1}+C^{I_fM_f}_{I_iM_i11}\right)C^{I_f0}_{I_i-111}+\left(C^{I_fM_f}_{I_iM_i2-1}-C^{I_fM_f}_{I_iM_i21}\right)C^{I_f0}_{I_i-121}\right],\end{aligned}\tag{C.24}$$

where the small Wigner functions $d^I_{MK}\equiv d^I_{MK}(\theta)$ are defined by

$$D^I_{MK}\equiv e^{-iM\phi}d^I_{MK}e^{-iK\gamma},\tag{C.25}$$

and the identities

$$d^1_{11}-d^2_{11}=d^1_{-11}+d^2_{-11},\qquad d^1_{1-1}+d^2_{1-1}=d^1_{-1-1}-d^2_{-1-1}.\tag{C.26}$$

have been employed. Since the spin of the final state I_f is even, the symmetry properties of the Clebsch-Gordan [50] coefficients allow us to rewrite some of these integrals as follows

$$\begin{aligned}&\int d\Omega d\gamma D^{I_f*}_{M_f0}e^{i2\phi}\left(D^1_{11}-D^2_{11}\right)D^{I_i}_{M_i-1}\\&\quad=\frac{4\pi^2}{2I_f+1}(-1)^{I_i}\left(-C^{I_fM_f}_{I_iM_i1-1}C^{I_f0}_{I_i11-1}+C^{I_fM_f}_{I_iM_i2-1}C^{I_f0}_{I_i12-1}\right),\end{aligned}\tag{C.27}$$

$$\begin{aligned}&\int d\Omega d\gamma D^{I_f*}_{M_f0}e^{-i2\phi}\left(D^1_{-11}+D^2_{-11}\right)D^{I_i}_{M_i-1}\\&\quad=\frac{4\pi^2}{2I_f+1}(-1)^{I_i}\left(-C^{I_fM_f}_{I_iM_i11}C^{I_f0}_{I_i11-1}-C^{I_fM_f}_{I_iM_i21}C^{I_f0}_{I_i12-1}\right),\end{aligned}\tag{C.28}$$

$$\begin{aligned}&\int d\Omega d\gamma D^{I_f*}_{M_f0}\left(D^1_{-11}+D^2_{-11}+D^1_{11}-D^2_{11}\right)D^{I_i}_{M_i-1}\\&\quad=\frac{4\pi^2}{2I_f+1}(-1)^{I_i}\left[-\left(C^{I_fM_f}_{I_iM_i1-1}+C^{I_fM_f}_{I_iM_i11}\right)C^{I_f0}_{I_i11-1}+\left(C^{I_fM_f}_{I_iM_i2-1}-C^{I_fM_f}_{I_iM_i21}\right)C^{I_f0}_{I_i12-1}\right].\end{aligned}\tag{C.29}$$

Thus, the matrix elements (C.18) are

$$\begin{aligned}i\langle f|\mathbf{A}_\Gamma\cdot\nabla_{\Omega\gamma}|i\rangle=&-\frac{iAkR}{2}\sqrt{\frac{2I_i+1}{2I_f+1}}\sqrt{I_i(I_i+1)}C^{I_i1}_{I_i21-1}\\&\left[\left(C^{I_fM_f}_{I_iM_i1-1}+C^{I_fM_f}_{I_iM_i11}\right)C^{I_f0}_{I_i11-1}-\left(C^{I_fM_f}_{I_iM_i2-1}-C^{I_fM_f}_{I_iM_i21}\right)C^{I_f0}_{I_i12-1}\right]\\=&-\frac{iAkR}{2}\sqrt{\frac{2I_i+1}{2I_f+1}}\sqrt{\frac{(I_i-1)(I_i+2)}{2}}\\&\left[\left(C^{I_fM_f}_{I_iM_i1-1}+C^{I_fM_f}_{I_iM_i11}\right)C^{I_f0}_{I_i11-1}-\left(C^{I_fM_f}_{I_iM_i2-1}-C^{I_fM_f}_{I_iM_i21}\right)C^{I_f0}_{I_i12-1}\right].\end{aligned}\tag{C.30}$$

Under Hermitian conjugation, the angular momentum in the tangent plane

operator transforms as

$$\begin{aligned}(-i\nabla_{\Omega\gamma})^{\dagger} &= \left(\frac{i}{2}\left[\hat{\mathbf{I}}^2, \mathbf{e}_r\right] - i\mathbf{e}_r\right)^{\dagger} \\ &= \frac{i}{2}\left[\hat{\mathbf{I}}^2, \mathbf{e}_r\right] + i\mathbf{e}_r \\ &= -i\nabla_{\Omega\gamma} + i2\mathbf{e}_r.\end{aligned} \tag{C.31}$$

Consequently, we can write the matrix elements of $i\nabla_{\Omega\gamma}\cdot\mathbf{A}_{\Gamma}$ as

$$\begin{aligned}-\langle f|\left(-i\nabla_{\Omega\gamma}\right)\cdot\mathbf{A}_{\Gamma}|i\rangle &= -\left(\langle i|\mathbf{A}_{\Gamma}\cdot\left(-i\nabla_{\Omega\gamma}\right)^{\dagger}|f\rangle\right)^{*} \\ &= -\left(\langle i|A_{\Gamma\theta}\hat{p}_{\theta}|f\rangle\right)^{*} - \left(\langle i|A_{\Gamma\phi}\hat{p}_{\phi\gamma}|f\rangle\right)^{*} - \left(\langle i|i2\mathbf{A}_{\Gamma}\cdot\mathbf{e}_r|f\rangle\right)^{*}.\end{aligned} \tag{C.32}$$

Notice that the last term vanishes since $\mathbf{A}_{\Gamma}$ do not posses a radial component. The matrix elements on the right side of Equation (C.32) are

$$\begin{aligned}&\langle i|A_{\Gamma\theta}\hat{p}_{\theta}|f\rangle = \frac{iAkR}{8}\sqrt{\frac{(2I_i+1)(2I_f+1)}{32\pi^4}}\sqrt{\frac{I_f(I_f+1)}{2}}\int d\Omega d\gamma\left(D^{I_i*}_{M_i2} + (-1)^{I_i}D^{I_i*}_{M_i-2}\right) \\ &\left[e^{-i\gamma}\left(D^1_{-1-1} - D^2_{-1-1} + D^1_{1-1} + D^2_{1-1}\right) + e^{i\gamma}\left(D^1_{-11} + D^2_{-11} + D^1_{11} - D^2_{11}\right)\right]\left(e^{i2\gamma} + e^{-i2\gamma}\right) \\ &\left(e^{i\gamma}C^{I_f1}_{I_f011}D^{I_f}_{M_f1} - e^{-i\gamma}C^{I_f1}_{I_f011}D^{I_f}_{M_f-1}\right)\end{aligned}$$

$$\begin{aligned}&= \frac{iAkR}{8}\sqrt{\frac{(2I_i+1)(2I_f+1)}{32\pi^4}}\sqrt{\frac{I_f(I_f+1)}{2}}C^{I_f1}_{I_f011}\int d\Omega d\gamma D^{I_i*}_{M_i2} \\ &\Big\{\left[e^{-i2\gamma}\left(D^1_{-1-1} - D^2_{-1-1} + D^1_{1-1} + D^2_{1-1}\right) + \left(D^1_{-11} + D^2_{-11} + D^1_{11} - D^2_{11}\right)\right]D^{I_f}_{M_f1} \\ &- \left[e^{-i4\gamma}\left(D^1_{-1-1} - D^2_{-1-1} + D^1_{1-1} + D^2_{1-1}\right) + e^{-i2\gamma}\left(D^1_{-11} + D^2_{-11} + D^1_{11} - D^2_{11}\right)\right]D^{I_f}_{M_f-1}\Big\} \\ &+ \frac{iAkR}{8}\sqrt{\frac{(2I_i+1)(2I_f+1)}{32\pi^4}}\sqrt{\frac{I_f(I_f+1)}{2}}C^{I_f1}_{I_f011}\int d\Omega d\gamma(-1)^{I_i}D^{I_i*}_{M_i-2} \\ &\Big\{\left[e^{i2\gamma}\left(D^1_{-1-1} - D^2_{-1-1} + D^1_{1-1} + D^2_{1-1}\right) + e^{i4\gamma}\left(D^1_{-11} + D^2_{-11} + D^1_{11} - D^2_{11}\right)\right]D^{I_f}_{M_f1} \\ &- \left[\left(D^1_{-1-1} - D^2_{-1-1} + D^1_{1-1} + D^2_{1-1}\right) + e^{i2\gamma}\left(D^1_{-11} + D^2_{-11} + D^1_{11} - D^2_{11}\right)\right]D^{I_f}_{M_f-1}\Big\}\end{aligned} \tag{C.33}$$

$$\begin{aligned}&= \frac{iAkR}{8}\sqrt{\frac{(2I_i+1)(2I_f+1)}{32\pi^4}}\sqrt{\frac{I_f(I_f+1)}{2}}C^{I_f1}_{I_f011}\int d\Omega d\gamma D^{I_i*}_{M_i2} \\ &\Big\{\left[e^{i2\phi}\left(D^1_{11} - D^2_{11}\right) + e^{-i2\phi}\left(D^1_{-11} + D^2_{-11}\right) + \left(D^1_{-11} + D^2_{-11} + D^1_{11} - D^2_{11}\right)\right]D^{I_f}_{M_f1} \\ &- \left[e^{-i4\gamma}\left(D^1_{-1-1} - D^2_{-1-1} + D^1_{1-1} + D^2_{1-1}\right) + e^{-i2\gamma}\left(D^1_{-11} + D^2_{-11} + D^1_{11} - D^2_{11}\right)\right]D^{I_f}_{M_f-1}\Big\} \\ &+ \frac{iAkR}{8}\sqrt{\frac{(2I_i+1)(2I_f+1)}{32\pi^4}}\sqrt{\frac{I_f(I_f+1)}{2}}C^{I_f1}_{I_f011}\int d\Omega d\gamma(-1)^{I_i}D^{I_i*}_{M_i-2} \\ &\Big\{\left[e^{i2\gamma}\left(D^1_{-1-1} - D^2_{-1-1} + D^1_{1-1} + D^2_{1-1}\right) + e^{i4\gamma}\left(D^1_{-11} + D^2_{-11} + D^1_{11} - D^2_{11}\right)\right]D^{I_f}_{M_f1} \\ &- \left[\left(D^1_{-1-1} - D^2_{-1-1} + D^1_{1-1} + D^2_{1-1}\right) + e^{i2\phi}\left(D^1_{1-1} + D^2_{1-1}\right) + e^{-i2\phi}\left(D^1_{-1-1} - D^2_{-1-1}\right)\right]D^{I_f}_{M_f-1}\Big\}\end{aligned}$$

and

$$\begin{aligned}
\langle i|A_{\Gamma\phi}\hat{p}_{\phi\gamma}|f\rangle = &-\frac{iAkR}{8}\sqrt{\frac{(2I_i+1)(2I_f+1)}{32\pi^4}}\sqrt{\frac{I_f(I_f+1)}{2}}\int d\Omega d\gamma \left(D^{I_i*}_{M_i 2}+(-1)^{I_i}D^{I_i*}_{M_i -2}\right)\\
&\left[e^{-i\gamma}\left(D^1_{-1-1}-D^2_{-1-1}+D^1_{1-1}+D^2_{1-1}\right)+e^{i\gamma}\left(D^1_{-11}+D^2_{-11}+D^1_{11}-D^2_{11}\right)\right]\left(e^{i2\gamma}-e^{-i2\gamma}\right)\\
&\left(e^{-i\gamma}C^{I_f 1}_{I_f 011}D^{I_f}_{M_f -1}+e^{i\gamma}C^{I_f 1}_{I_f 011}D^{I_f}_{M_f 1}\right)
\end{aligned}$$

$$\begin{aligned}
&= \frac{iAkR}{8}\sqrt{\frac{(2I_i+1)(2I_f+1)}{32\pi^4}}\sqrt{\frac{I_f(I_f+1)}{2}}C^{I_f 1}_{I_f 011}\int d\Omega d\gamma D^{I_i*}_{M_i 2}\\
&\left\{\left[e^{i2\phi}\left(D^1_{11}-D^2_{11}\right)+e^{-i2\phi}\left(D^1_{-11}+D^2_{-11}\right)+\left(D^1_{-11}+D^2_{-11}+D^1_{11}-D^2_{11}\right)\right]D^{I_f}_{M_f 1}\right.\\
&\left.+\left[e^{-i4\gamma}\left(D^1_{-1-1}-D^2_{-1-1}+D^1_{1-1}+D^2_{1-1}\right)+e^{-i2\gamma}\left(D^1_{-11}+D^2_{-11}+D^1_{11}-D^2_{11}\right)\right]D^{I_f}_{M_f -1}\right\}\\
&- \frac{iAkR}{8}\sqrt{\frac{(2I_i+1)(2I_f+1)}{32\pi^4}}\sqrt{\frac{I_f(I_f+1)}{2}}C^{I_f 1}_{I_f 011}\int d\Omega d\gamma (-1)^{I_i}D^{I_i*}_{M_i -2}\\
&\left\{\left[e^{i2\gamma}\left(D^1_{-1-1}-D^2_{-1-1}+D^1_{1-1}+D^2_{1-1}\right)+e^{i4\gamma}\left(D^1_{-11}+D^2_{-11}+D^1_{11}-D^2_{11}\right)\right]D^{I_f}_{M_f 1}\right.\\
&\left.+\left[\left(D^1_{-1-1}-D^2_{-1-1}+D^1_{1-1}+D^2_{1-1}\right)+e^{i2\phi}\left(D^1_{1-1}+D^2_{1-1}\right)+e^{-i2\phi}\left(D^1_{-1-1}-D^2_{-1-1}\right)\right]D^{I_f}_{M_f -1}\right\}.
\end{aligned} \tag{C.34}$$

Adding the matrix elements (C.33) and (C.34) leads to

$$\begin{aligned}
-\langle i|\mathbf{A}_\Gamma\cdot\left(-i\nabla_{\Omega\gamma}\right)^\dagger|f\rangle = &-\frac{iAkR}{4}\sqrt{\frac{(2I_i+1)(2I_f+1)}{32\pi^4}}\sqrt{\frac{I_f(I_f+1)}{2}}C^{I_f 1}_{I_f 011}\int d\Omega d\gamma D^{I_i*}_{M_i 2}\\
&\left[e^{i2\phi}\left(D^1_{11}-D^2_{11}\right)+e^{-i2\phi}\left(D^1_{-11}+D^2_{-11}\right)+\left(D^1_{-11}+D^2_{-11}+D^1_{11}-D^2_{11}\right)\right]D^{I_f}_{M_f 1}\\
&+\frac{iAkR}{4}\sqrt{\frac{(2I_i+1)(2I_f+1)}{32\pi^4}}\sqrt{\frac{I_f(I_f+1)}{2}}C^{I_f 1}_{I_f 011}\int d\Omega d\gamma (-1)^{I_i}D^{I_i*}_{M_i -2}\\
&\left[\left(D^1_{-1-1}-D^2_{-1-1}+D^1_{1-1}+D^2_{1-1}\right)+e^{i2\phi}\left(D^1_{1-1}+D^2_{1-1}\right)+e^{-i2\phi}\left(D^1_{-1-1}-D^2_{-1-1}\right)\right]D^{I_f}_{M_f -1}.
\end{aligned} \tag{C.35}$$

The integrals in Equation (C.35) can be evaluated as follows

$$\begin{aligned}
&\int d\Omega d\gamma D^{I_i*}_{M_i 2}e^{i2\phi}\left(D^1_{11}-D^2_{11}\right)D^{I_f}_{M_f 1}\\
&\quad=\frac{4\pi^2}{2I_i+1}\left(C^{I_i M_i}_{I_f M_f 1-1}C^{I_i 2}_{I_f 111}+C^{I_i M_i}_{I_f M_f 2-1}C^{I_i 2}_{I_f 121}\right),
\end{aligned} \tag{C.36}$$

$$\begin{aligned}
&\int d\Omega d\gamma D^{I_i*}_{M_i 2}e^{-i2\phi}\left(D^1_{-11}+D^2_{-11}\right)D^{I_f}_{M_f 1}\\
&\quad=\frac{4\pi^2}{2I_i+1}\left(C^{I_i M_i}_{I_f M_f 11}C^{I_i 2}_{I_f 111}-C^{I_i M_i}_{I_f M_f 21}C^{I_i 2}_{I_f 121}\right),
\end{aligned} \tag{C.37}$$

$$\begin{aligned}
&\int d\Omega d\gamma D^{I_i*}_{M_i 2}\left(D^1_{-11}+D^2_{-11}+D^1_{11}-D^2_{11}\right)D^{I_f}_{M_f 1}\\
&\quad=\frac{4\pi^2}{2I_i+1}\left[\left(C^{I_i M_i}_{I_f M_f 1-1}+C^{I_i M_i}_{I_f M_f 11}\right)C^{I_i 2}_{I_f 111}+\left(C^{I_i M_i}_{I_f M_f 2-1}-C^{I_i M_i}_{I_f M_f 21}\right)C^{I_i 2}_{I_f 121}\right],
\end{aligned} \tag{C.38}$$

$$\begin{aligned}
&\int d\Omega d\gamma D^{I_i*}_{M_i-2}\left(D^1_{-1-1}-D^2_{-1-1}+D^1_{1-1}+D^2_{1-1}\right)D^{I_f}_{M_f-1}\\
&\quad=\frac{4\pi^2}{2I_i+1}\left[\left(C^{I_iM_i}_{I_fM_f1-1}+C^{I_iM_i}_{I_fM_f11}\right)C^{I_i-2}_{I_f-11-1}-\left(C^{I_iM_i}_{I_fM_f2-1}-C^{I_iM_i}_{I_fM_f21}\right)C^{I_i-2}_{I_f-12-1}\right]\\
&\quad=\frac{4\pi^2}{2I_i+1}(1)^{I_i}\left[-\left(C^{I_iM_i}_{I_fM_f1-1}+C^{I_iM_i}_{I_fM_f11}\right)C^{I_i2}_{I_f111}-\left(C^{I_iM_i}_{I_fM_f2-1}-C^{I_iM_i}_{I_fM_f21}\right)C^{I_i2}_{I_f121}\right],
\end{aligned}\tag{C.39}$$

$$\begin{aligned}
&\int d\Omega d\gamma D^{I_i*}_{M_i-2}e^{i2\phi}\left(D^1_{1-1}+D^2_{1-1}\right)D^{I_f}_{M_f-1}\\
&\quad=\frac{4\pi^2}{2I_i+1}\left(C^{I_iM_i}_{I_fM_f1-1}C^{I_i-2}_{I_f-11-1}-C^{I_iM_i}_{I_fM_f2-1}C^{I_i-2}_{I_f-12-1}\right)\\
&\quad=\frac{4\pi^2}{2I_i+1}(1)^{I_i}\left(-C^{I_iM_i}_{I_fM_f1-1}C^{I_i2}_{I_f111}-C^{I_iM_i}_{I_fM_f2-1}C^{I_i2}_{I_f121}\right),
\end{aligned}\tag{C.40}$$

$$\begin{aligned}
&\int d\Omega d\gamma D^{I_i*}_{M_i-2}e^{-i2\phi}\left(D^1_{-1-1}-D^2_{-1-1}\right)D^{I_f}_{M_f-1}\\
&\quad=\frac{4\pi^2}{2I_i+1}\left(C^{I_iM_i}_{I_fM_f11}C^{I_i-2}_{I_f-11-1}+C^{I_iM_i}_{I_fM_f21}C^{I_i-2}_{I_f-12-1}\right)\\
&\quad=\frac{4\pi^2}{2I_i+1}(1)^{I_i}\left(-C^{I_iM_i}_{I_fM_f11}C^{I_i2}_{I_f111}+C^{I_iM_i}_{I_fM_f21}C^{I_i2}_{I_f121}\right),
\end{aligned}\tag{C.41}$$

where the fact that I_f is even and the symmetry properties of the Clebsch-Gordan coefficients have been employed. Inserting these integrals into (C.35) leads to

$$\begin{aligned}
-\langle i|\mathbf{A}_\Gamma\cdot(-i\nabla_{\Omega\gamma})^\dagger|f\rangle=&-\frac{iAkR}{2}\sqrt{\frac{2I_f+1}{2I_i+1}}\sqrt{I_f(I_f+1)}C^{I_f1}_{I_f011}\\
&\left[\left(C^{I_iM_i}_{I_fM_f1-1}+C^{I_iM_i}_{I_fM_f11}\right)C^{I_i2}_{I_f111}+\left(C^{I_iM_i}_{I_fM_f2-1}-C^{I_iM_i}_{I_fM_f21}\right)C^{I_i2}_{I_f121}\right]\\
=&\frac{iAkR}{2}\sqrt{\frac{2I_i+1}{2I_f+1}}\sqrt{\frac{I_f(I_f+1)}{2}}\\
&\left[\left(C^{I_fM_f}_{I_iM_i1-1}+C^{I_fM_f}_{I_iM_i11}\right)C^{I_f1}_{I_i21-1}-\left(C^{I_fM_f}_{I_iM_i2-1}-C^{I_fM_f}_{I_iM_i21}\right)C^{I_f1}_{I_i22-1}\right],
\end{aligned}\tag{C.42}$$

which implies

$$\begin{aligned}
i\langle i|\nabla_{\Omega\gamma}\cdot\mathbf{A}_\Gamma|f\rangle=&-\frac{iAkR}{2}\sqrt{\frac{2I_i+1}{2I_f+1}}\sqrt{\frac{I_f(I_f+1)}{2}}\\
&\left[\left(C^{I_fM_f}_{I_iM_i1-1}+C^{I_fM_f}_{I_iM_i11}\right)C^{I_f1}_{I_i21-1}-\left(C^{I_fM_f}_{I_iM_i2-1}-C^{I_fM_f}_{I_iM_i21}\right)C^{I_f1}_{I_i22-1}\right].
\end{aligned}\tag{C.43}$$

According to the recursion relations for the Clebsch-Gordan coefficients [50] it

is possible to write

$$\begin{aligned}\sqrt{\frac{(I_i-1)(I_i+2)}{2}}C^{I_f0}_{I_i11-1} &= \sqrt{\frac{I_f(I_f+1)}{2}}C^{I_f1}_{I_i21-1},\\ \sqrt{\frac{(I_i-1)(I_i+2)}{2}}C^{I_f0}_{I_i12-1} &= \sqrt{\frac{I_f(I_f+1)}{2}}C^{I_f1}_{I_i22-1} - \sqrt{2}C^{I_f0}_{I_i22-2}.\end{aligned} \tag{C.44}$$

Combining the matrix elements (C.30) and (C.43), and employing the recursion relations (C.44) allow us to write the angular matrix elements of the LO interband interaction as

$$\begin{aligned}i\langle f|\left(\nabla_{\Omega\gamma}\cdot\mathbf{A}_\Gamma + \mathbf{A}_\Gamma\cdot\nabla_{\Omega\gamma}\right)|i\rangle &= -iAkR\sqrt{\frac{2I_i+1}{2I_f+1}}\sqrt{\frac{I_f(I_f+1)}{2}}C^{I_f1}_{I_i21-1}\left(C^{I_fM_f}_{I_iM_i1-1}+C^{I_fM_f}_{I_iM_i11}\right)\\ &+ iAkR\sqrt{\frac{2I_i+1}{2(2I_f+1)}}\left(\sqrt{I_f(I_f+1)}C^{I_f1}_{I_i22-1}-C^{I_f0}_{I_i22-2}\right)\left(C^{I_fM_f}_{I_iM_i2-1}-C^{I_fM_f}_{I_iM_i21}\right).\end{aligned} \tag{C.45}$$

The first term on the right side of Equation (C.45) is a contribution of order $\mathcal{O}(kR)$ to the electric dipole angular matrix elements. We neglect this contribution, and keep only the electric quadrupole component.

In order to write these matrix elements in a more convenient form, we employ the explicit form of the Clebsch-Gordan coefficients in different cases to write

$$\begin{aligned}\sqrt{I_f(I_f+1)}C^{I_f1}_{I_i22-1} &= -2(I_i-2)C^{I_f0}_{I_i22-2} \qquad I_f = I_i-2,\\ \sqrt{I_f(I_f+1)}C^{I_f1}_{I_i22-1} &= -(I_i-3)C^{I_f0}_{I_i22-2} \qquad I_f = I_i-1,\\ \sqrt{I_f(I_f+1)}C^{I_f1}_{I_i22-1} &= 3C^{I_f0}_{I_i22-2} \qquad I_f = I_i,\\ \sqrt{I_f(I_f+1)}C^{I_f1}_{I_i22-1} &= (I_i+4)C^{I_f0}_{I_i22-2} \qquad I_f = I_i+1,\\ \sqrt{I_f(I_f+1)}C^{I_f1}_{I_i22-1} &= 2(I_i+3)C^{I_f0}_{I_i22-2} \qquad I_f = I_i+2,\end{aligned} \tag{C.46}$$

and recall that

$$\begin{aligned}I_f(I_f+1)-\left[I_i(I_i+1)-K_i^2\right] &= -4I_1+6 \qquad I_f = I_i-2,\\ I_f(I_f+1)-\left[I_i(I_i+1)-K_i^2\right] &= -2I_1+4 \qquad I_f = I_i-1,\\ I_f(I_f+1)-\left[I_i(I_i+1)-K_i^2\right] &= 4 \qquad I_f = I_i,\\ I_f(I_f+1)-\left[I_i(I_i+1)-K_i^2\right] &= 2I_1+6 \qquad I_f = I_i+1,\\ I_f(I_f+1)-\left[I_i(I_i+1)-K_i^2\right] &= 4I_1+10 \qquad I_f = I_i+2.\end{aligned} \tag{C.47}$$

Identities (C.46) and (C.47) imply that we can write the quadrupole component

of the angular matrix elements (C.45) as

$$i\langle f|\left(\nabla_{\Omega\gamma}\cdot\mathbf{A}_{\Gamma}+\mathbf{A}_{\Gamma}\cdot\nabla_{\Omega\gamma}\right)|i\rangle = iAkRC_0 w\sqrt{\frac{2I_i+1}{2(2I_f+1)}}C^{I_f 0}_{I_i 2 2-2}\left(C^{I_f M_f}_{I_i M_i 2-1}-C^{I_f M_f}_{I_i M_i 21}\right), \tag{C.48}$$

where $w=\left[I_f(I_f+1)-(I_i(I_i+1)-K_i^2)\right]/2C_0$.

Finally, the matrix elements of the LO interband quadrupole interaction between initial states in the γ band a final states in the ground band are

$$\langle f|\hat{H}^{(\mathbf{A})}_{\mathrm{NNLO}}|i\rangle = i\sqrt{\frac{1}{2\omega_2}}\frac{C_\gamma}{C_0}\frac{qAkR}{2}w\sqrt{\frac{3(2I_i+1)}{6(2I_f+1)}}C^{I_f 0}_{I_i 2 2-2}\left(C^{I_f M_f}_{I_i M_i 2-1}-C^{I_f M_f}_{I_i M_i 21}\right). \tag{C.49}$$

VITA

Eduardo Antonio Coello Pérez was born in Mexico City, Mexico to the parents of Maite Pérez Pérez and Marco Antonio Coello Coutiño. He is the third of four sons. His brothers are Alejandro Coello Pérez, Daniel Coello Pérez and Raúl Coello Pérez.

As an undergraduate, he studied the Physics career at the Universidad Nacional Autónoma de México, where he was first introduced to the field of experimental Nuclear Physics. He obtained a Bachelors of Physics degree in 2011 under the advisory of Dr. Efraín Rafael Chávez Lomeli. He started his graduate studies at The University of Tennessee, Knoxville, in the Doctor of Philosophy program in Physics in 2011 under the advisory of Dr. Dan Shapira. One year later he started working as a research assistant for Dr. Thomas Papenbrock, who introduced him to the field of theoretical Nuclear Physics.

During his time in graduate school, Eduardo Antonio Coello Pérez attended the TALENT course on Nuclear forces and their impact on structure, reactions and astrophysics, held at the Institute for Nuclear Theory, at the University of Washington in 2013 under the supervision of Dr. Dick Furnstahl and Dr. Achim Schwenk, and the TALENT course on Theory for exploring nuclear structure experiments, held at the Grand Accélérateur National d'Ions Lourds, at Caen, France, in 2014 under the supervision of Dr. Richard F. Casten, Dr. Marek Poszajczak and Dr. Piet Van Isacker. His final project in the later course was recognized as one of the best. In 2015, he was awarded the Extraordinary Professional Promise Award at The University of Tennessee Citation Awards.

Eduardo Antonio Coello Pérez obtained his Doctor of Philosophy Degree in Nuclear Physics in December 2015.